突觸前神經活性對齒狀迴抑制性神經訊息傳導之研究

Rapid Dynamic Changes of Dendritic Inhibition in the Dentate Gyrus by Presynaptic Activity Patterns

研究生：劉于超 (Yu-Chao Liu)

指導教授：連正章 博士 (Cheng-Chang Lien, M.D., Ph.D.)

國立陽明大學

神經科學研究所

博士論文

Institute of Neuroscience

National Yang-Ming University

Doctoral Dissertation

中華民國 一百零三年 二月

February, 2014

ABSTRACT

The dentate gyrus (DG) serves as a primary gate to control information transfer from the cortex to the hippocampus. Activation of incoming cortical inputs results in rapid synaptic excitation followed by slow γ-aminobutyric acid-mediated (GABAergic) synaptic inhibition onto DG granule cells (GCs). GABAergic inhibitory interneurons (INs) in the DG comprise fast-spiking (FS) and non-fast-spiking (non-FS) cells. Anatomical analyses of DG INs reveal that FS cells are soma-targeting INs, whereas non-FS cells are dendrite-targeting INs. These two IN classes are differentially recruited by excitatory inputs and in turn provide exquisite spatiotemporal control over GC activity. Yet, little is known how FS and non-FS cells transform their presynaptic dynamics into varying postsynaptic response amplitudes. Using paired recordings in rat hippocampal slices, I show that inhibition in the DG is dominated by somatic GABAergic inputs during periods of sparse presynaptic activity, whereas dendritic GABAergic inputs are rapidly shifted to powerful and sustained inhibition during periods of intense presynaptic activity. The variant dynamics of dendritic inhibition is dependent on presynaptic IN subtypes and their activity patterns and is attributed to Ca^{2+}-dependent increases in the probability of release and the size of the readily releasable pool. Furthermore, the degree of dynamic GABA release can be reduced by blocking voltage-gated K^+ channels, which increases the efficacy of dendrite-targeting IN output synapses during sparse firing. Such rapid dynamic modulation of dendritic inhibition may act as a frequency-dependent filter to prevent over-excitation of GC dendrites and thus set the excitatory-inhibitory synaptic balance in the DG circuits.

中文摘要

齒狀迴是負責處理訊息由大腦皮質傳送至海馬迴的第一站。當皮質訊息送至齒狀迴時，其中的顆粒細胞會接受到快速的興奮性刺激，而皮質訊息會同時激活分泌伽瑪胺基丁酸的中間聯絡神經元，引起對顆粒細胞抑制性的前饋反應，也就是在顆粒細胞接受到興奮性刺激後，會伴隨著較慢的抑制性訊息。而齒狀迴中分泌伽瑪胺基丁酸的中間聯絡神經元可簡略分為兩種，高頻動作電位與非高頻動作電位細胞。神經解剖學證據顯示，高頻動作電位細胞是細胞本體抑制型中間聯絡神經元，非高頻動作電位細胞則是樹突抑制型中間聯絡神經元。這兩類中間聯絡神經元受到興奮性刺激後，會在不同的時間點被激活，進而從時間和空間上，精巧地調控顆粒細胞的活性。然而，這些中間聯絡神經元如何將不同頻率/強度的訊息，傳遞至下游的顆粒細胞，仍不清楚。因此，我在大鼠的海馬迴切片中，透過同時記錄突觸前後的神經元(配對記錄)發現：在稀疏的突觸前刺激下，齒狀迴的抑制訊息主要來自於本體抑制型中間聯絡神經元；但是，當密集且強烈的突觸前刺激發生時，樹突抑制訊息將快速地增強。而決定樹突抑制訊息強度的關鍵在於，突觸前的細胞種類以及其活性高低，高活性狀態將造成鈣離子相關的囊泡釋放機率以及，立即可釋放的囊泡數目上升。此外，透過阻斷電位控制的鉀離子通道，將增加稀疏刺激下樹突抑制訊息的強度，因此減少樹突抑制訊息受活性調控而增強的程度。透過神經活性，快速地調控樹突抑制訊息，將可作為一種特定的濾波系統，避免顆粒細胞在高強度刺激下過度興奮，因此，進而達成齒狀迴中興奮與抑制訊息的整體平衡。

TABLE OF CONTENTS

ABBREVIATIONS

AP: action potential

BC: basket cell

C/A: commissural-associational

CB_1R: cannabinoid receptor type 1

CCK: cholecystokinin

DG: dentate gyrus

DI: dendrite-targeting IN

DSI: depolarization-induced suppression of inhibition

FS: fast spiking

GABA: γ-aminobutyric acid

GC: granule cell

GCL: granule cell layer

HICAP: hilar IN with C/A pathway-associated

HIPP: hilar IN with PP-associated

IN: interneuron

ISI: inter-spike interval

ML: molecular layer

PI: perisomatic-targeting IN

PP: perforant pathway

PV: parvalbumin

RMP: resting membrane potential

RRP: readily releasable pool

uIPSC: unitary inhibitory postsynaptic current

INTRODUCTION

The Hippocampus

The hippocampus is the cortical component in the human brain and other vertebrates. This term, "hippocampus", arises from its structural appearance which is similar to the seahorse (Greek: *"hippos"* meaning horse and *"kampos"* meaning sea monster). Another name, "Ammon's horn" (Ammon, the ancient Egyptian god), is also sometimes used to describe this bilateral ram's horn- or banana-shaped structure. In terms of anatomy, the hippocampus is located underneath the neocortex primarily in the medial temporal lobe and belongs to the limbic system (Latin: *"limbus"* meaning border), structures line the edge of the cortex including the hippocampus, cingulate cortex, olfactory cortex, and amygdala. The hippocampal formation consists of the hippocampus, subiculum and entorhinal cortex. In general, the hippocampus processes the information coming from entorhinal cortex and sends the output to other brain areas *via* subiculum.

Two major hippocampal functions have been investigated for decades, memory and spatial map. In 1957, Scoville and Milner reported a famous case that a patient, named H.M., receives surgical removals of two-thirds of the hippocampal formation and amygdala to relief the epileptic seizures, and gets severe anterograde and partial retrograde amnesia (Scoville and Milner, 1957). After the surgery, H.M. could not transform declarative short-term memory into long-term memory. However, his working memory and procedural memory remained intact. This unexpected case gave rise to countless studies investigating where and how the memory is stored in the brain, and focusing on the hippocampus. And now, there is a general agreement that the hippocampus plays an important role in memory formation.

The second major hippocampal function is spatial discrimination. The spatial theory was originated from O’Keefe and Dostrovsky. They discovered that neurons in the rat hippocampus show spiking activity especially related to the physical location of rat body in the environment (O’Keefe and Dostrovsky, 1971). The neuron they found is called “place cell” which is thought to represent the spatial information in the brain (O’Keefe and Nadel, 1978; Epsztein et al., 2011). In addition to place cell, there is another cell also representing spatial information in the entorhinal cortex, named “grid cell”. The spiking patterns of these cells are grid-like shape related to the spatial locations (Fyhn et al., 2004; Hafting et al., 2005). Besides, a part of hippocampus, dentate gyrus (DG), has been found which is critical for pattern separation and pattern completion. (McHugh et al., 2007; Nakashiba et al., 2012). Based on these remarkable findings, as with the memory formation, the hippocampus also functions as a spatial map in the brain.

Neuronal and Synaptic Organization of the Rat Hippocampus

The hippocampus is a well-laminated structure comprising two parts, DG and hippocampus proper (Cornu Amonnis, CA1-CA3). The DG serves as a primary gate which receives the inputs mainly from the layer II of entorhinal cortex (perforant path, PP). And the principal cells in the DG, granule cells (GCs), send its axons (mossy fibers) toward to the CA3 area. The highly specialized axonal output of mossy fibers provides strong synaptic excitation to CA3 principal (pyramidal) cells (Geiger and Jonas, 2000; Rollenhagen et al., 2007). The CA3 area is the next step in the progression of connections, and CA3 pyramidal cells give rise to their projections called Schaffer collaterals that innervate the apical dendrites of CA1 principal (pyramidal) cells (Schaffer, 1892; Szirmai et al., 2012). Axons of CA1 pyramidal cells then extend into subiculum which is an important component of the outputs of the hippocampal formation which send to other brain regions including the entorhinal cortex (Naber and Witter, 1998; Ishizuka, 2001). Thus, the entorhinal-hippocampal circuit forms a loop processing and amplifying the cortical information.

Beyond the basic wiring components, the hippocampus has more exquisite neuronal connections. In the DG, in addition to perforant path innervating the outer two-thirds of the molecular layer, there is another excitatory pathway called commissural-associational (C/A) projections which appear to originate on the axonal collaterals of mossy cells in the hilus both ipsilateral and contralateral sides. This C/A pathway specifically targets to the inner third of the molecular layer where the proximal dendrites of GCs are located (Laurberg and Sørensen, 1981). Although the mossy fibers are elongated into CA3 stratum lucidum, its fasciculate axonal collaterals in the hilus also terminate on the thorny excrescences that are the special features of the proximal dendrites of mossy cells, and local γ-aminobutyric acid-releasing (GABAergic) interneurons (INs) in the DG, hilus and CA3 area (Geiger et al., 1997; Bischofberger et al., 2006a; Szabadics and Soltesz, 2009). In terms of the target selectivity of mossy fibers, it’s worthy to mention that the major postsynaptic targets of mossy fiber seem to be the INs (Acsády et al., 1998;

Szabadics and Soltesz, 2009). Because the mossy cells are glutamatergic neurons and densely innervated by the mossy fibers, they provide the substrate for a potential reverberatory circuitry within the entorhinal-hippocampal loop.

In the CA3 area, the pyramidal cells receive the excitatory inputs not only from the mossy fibers. CA3 pyramidal cells also give rise to commissural projections which terminate throughout stratum radiatum and oriens, to the CA3, CA2 and CA1 regions of both the ipsilateral and contralateral hippocampus. A single CA3 neuron may use ~11,000 presynaptic boutons to recurrently excite other CA3 pyramidal cells (Wittner et al., 2007; Mitra et al., 2011). Thus, CA3-CA3 circuit becomes another recurrent loop. Apart from mossy fibers and CA3 recurrent collaterals, perforant path from the layer II of entorhinal cortex provides additional excitatory drives to the CA3 field. Regarding the CA3 outputs, Schaffer collaterals from the CA3 dominate the excitatory outputs to the stratum radiatum of CA1 region, whereas INs in the CA1, in addition to pyramidal cells, are also innervated by this pathway. And synaptic activation of the INs results in the feed-forward inhibitions which can expand the dynamic range of the CA1 pyramidal cells, while receiving different strengths of afferent inputs (Pouille et al., 2009). The feed-forward inhibitions, especially somatic-inhibition, delicately control the neuronal synchrony and temporal fidelity of CA1 pyramidal cells (Cobb et al., 1995; Poullie and Scanziani, 2001). On the other hand, dendritic feed-forward inhibition is the primary regulator of input-output transformations in the CA1 pyramidal cells (Lovett-Barron et al., 2012).

The CA1 pyramidal cells receive two major excitatory input, one is Schaffer collateral pathway (stratum radiatum and oriens) carrying internal representations stored in the CA3; the other is temporoammonic pathway (stratum lacunosum-moleculare) carrying sensory information from the layer III of entorhinal cortex (Cutsuridis et al., 2010). The CA1 pyramidal cells give rise to connections both to the subiculum and deep layers (III, IV and V) of the entorhinal cortex serving as an output station to transfer the processed signals back to the cortex. In addition, CA1 INs can be directly activated by CA1 pyramidal cells, therefore forming the feed-back inhibitory loops. And the inhibitory transmissions can shift, in the activity-dependent manner, along the somato-dendritic axis (Pouille and Scanziani, 2004).

Diversity of Interneurons

Owning to the recently precise estimations, we know that the number of total neurons in the human and rat brain is ~8.6×10^{10} and ~2×10^{8}, respectively (Azevedo et al., 2009; Herculano-Houzel et al., 2006). Around ten percent of the neuron populations consist of INs in the hippocampus (Freund and Buzsáki, 1996) and ~25% in the neocortex (Ren et al., 1992; Markram et al., 2004). Even though INs account for the small part of neuronal populations in the brain, they are highly diverse as various distinct subtypes of INs.

There are at least 21 subtypes of IN in the hippocampal CA1 area (Klausberger and Somogyi 2008) and 11 subtypes in the neocortex (Markram et al., 2004), distinguished by three major features (Ascoli et al., 2008; DeFelipe et al., 2013). First, morphological features including somatic location, dendritic arborizations and axonal projections can be the bases to name the INs. For instance, one classical dendritic-targeting IN in the CA1 is called oriens lacunosum-moleculare (O-LM) cell due to the somatic location in the stratum oriens and wide distribution of the axonal plexus over the stratum lacunosum-moleculare (Maccaferri et al., 2000). Second, another nomenclature of INs depends on the molecular expressions, such as calcium-binding proteins, neuropeptides and receptors. In the CA1 area, one typical type of somatic-targeting INs is named basket cell (BC) because the basket-like axonal plexus massively covering the stratum pyramidale, the somatic location of CA1 pyramidal cells. Nevertheless, the CA1 BCs can be further discriminated according to the selective expression of parvalbumin (PV) and cholecystokinin (CCK), which correlate well with absence or presence of cannabinoid receptors type 1 (CB$_1$Rs), respectively (Katona et al., 1999; Tsou et al., 1999; Glickfeld and Scanziani, 2006). Last, physiological features such as firing patterns, resting membrane potential and input resistance, are also considered as critical criteria for classifying the INs.

One major challenge of research in neuroscience is to decipher the functional roles of distinct INs in the brain (Mott and Dingledine, 2003). Notwithstanding the limited knowledge of functional roles of distinct INs, several studies shed the insights of IN dichotomy. As mentioned before, perisomatic-targeting INs, like axo-axonic cells (AACs) and BCs, precisely control the firing timing of the principal cells and neuronal synchrony in the hippocampus including CA1, CA3 and DG (Poullie and Scanziani, 2001; Viney et al., 2013; Bartos et al., 2007), whereas dendrite-targeting INs, such as neurogliaform cells and O-LM cells, regulate dendritic electrical and biochemical signaling and synaptic plasticity therefore gating the information flow (Miles et al., 1996; Chittajallu et al., 2013; Leão et al., 2012; Chiu et al., 2013).

Synaptic Transmission

Synaptic transmission involves a highly complex series of events. An action potentials (AP), drove by voltage-gated sodium and potassium channels (Hodgkin and Huxley, 1952), invades a presynaptic terminal and results in the opening of voltage-gate calcium channels, which leads to a rise in intracellular Ca^{2+} concentration. Next, Ca^{2+} binds to a presynaptic Ca^{2+} sensor, which subsequently triggers the exocytosis of neurotransmitter-containing synaptic vesicles. Finally, the released transmitters diffuse across the synaptic cleft and bind to postsynaptic receptors. Therefore, a voltage change in the presynaptic neuron (AP) is converted into two chemical signals (Ca^{2+} and transmitter) and further transformed into an electrical response in the postsynaptic cell (Llinás et al., 1982; Borst and Sakmann, 1996). Intriguingly, such a sequence of biophysical and biochemical events can take place in a range (synaptic delay or latency) from sub-millisecond to few milliseconds (Geiger et al., 1997; Kraushaar and Jonas, 2000; Bartos et al., 2001; Glickfeld and Scanziani, 2006). Such synaptic latency may be influenced by the coupling distance between calcium channel and sensor (Eggermann et al., 2012).

Actually, communications between each neurons are highly specialized. Some synapses talk in a “whisper”; others “shout”. The “louder” the synapse, the more synaptic vesicles are needed to maintain effective transmission, ranging from a few hundred (whisperers) to nearly a million (shouters; Rizzoli and Betz, 2005). These vesicles reside in different "pools" in the presynaptic terminals. And it has been postulated that three distinct vesicle pools, varying from relative size, location, kinetics and mobility, maintain the dynamics of synaptic transmission (Zucker and Regehr, 2002; Rizzoli and Betz, 2005). First one, the readily releasable pool (RRP), the vesicles reside in RRP (~1-2% of total vesicles) are generally thought to be docked to the presynaptic active zone and primed for release. So, the RRP can be rapidly depleted by few shocks of high frequency electrical stimulation (Elmqvist and Quastel, 1965; Schneggenburger et al., 1999). Second one, the recycling pool, this pool of vesicles (~5-20%) is thought to maintain the release on moderate (physiological) stimulation by continuously recycling and refilling (Harata et al., 2001; Lange et al., 2003). Last one, the reserve pool (~80-90%), it serves as a depot of vesicles. And the mobilization and release of reserve pool can be only triggered during intense stimulation which causes the depletion of recycle pool (Richards et al., 2000). Although, it's possible that these vesicles are seldom or never recruited during physiological activity. In summary, the three pools model provides the substantial perspective of synaptic transmission and some explanations for the synaptic dynamics.

In spite of the presynaptic location of the sophisticated release machinery, the key factors that determine the action of neurotransmitter are primarily expressed postsynaptically. Take the GABAergic transmission as an example. The polarity of GABAergic response is mainly governed by the relation of resting membrane potential (RMP) and equilibrium potential of GABA_A receptor (E_{GABA}). According to Nernst equation, neurons have far more open K^+-selective channels than Na^+- or Ca2^+-selective channels, hence the RMP is relative negative and close to the equilibrium potential of potassium channels (E_K). And the E_K can be determined by the temperature and the intra- and extra-cellular K^+ concentration (Hille, 2001). Likewise, the E_{GABA} can be determined by the intra- and extra-cellular Cl^- concentration. However, the intracellular Cl^- concentration can be regulated by the differential expression of Cl^- transporters during development and seizures (Ben-Ari, 2002; Ben-Ari et al., 2012). Therefore, it's important and necessary to estimate the GABAergic action for investigating the GABAergic circuitry.

Synaptic Plasticity

As described above, synaptic transmission is very dynamic. And it's full of plasticity, which has been thought that it's the substantial component to explain why human has the ability to learn and store the memories (Kandel, 2009). Given the various functions ascribed to synaptic plasticity, it is not surprising that multiple forms and mechanisms of synaptic plasticity have been described. Synaptic transmission can be either enhanced or depressed by activity, and these changes span temporal domains ranging from milliseconds to hours, days, and presumably even longer (Citri and Malenka, 2008).

Numerous forms of short-term synaptic plasticity, lasting on the order of milliseconds to several minutes, have been observed including paired-pulse facilitation/depression (Zucker and

Regehr, 2002). They are thought to play important roles in short-term adaptations to sensory inputs, transient changes in behavioral states, and short-lasting forms of memory (Abbott and Regehr 2004). It is well established that the facilitation of Ca^{2+} influx can elevate the synaptic release probability, therefore contributing to the short-term facilitation (Augustine, 2001). On the other hand, the short-term depression can be caused by the depletion of readily releasable pool (synaptic fatigue) or the inhibitory modulations of presynaptic receptors (Tsodyks and Markram, 1997; Miller, 1998; Oláh et al., 2009).

In terms of long-term synaptic plasticity, it has been observed for four decades. In 1973, Terje Lømo and Tim Bliss first demonstrated that repetitive stimulation of excitatory input (perforant path, at 100 Hz for 3-4 seconds) to the DG results in a potentiation of synaptic strength which could last for hours or even days (Bliss and Lømo, 1973). This long-lasting potentiation, termed long-term potentiation (LTP), has been the object for intensive investigations. Because it’s wildly believed that LTP provides an important key to understand the molecular and cellular mechanisms of memory formation. Indeed, many studies reveal that LTP and the downstream signaling are required for the memory formation *in vivo* (Morris et al., 1986; Bach et al., 1995; Abel et al., 1997; Kelleher et al., 2004). In contrast to LTP, the long-term depression (LTD) can be induced by prolonged repetitive low frequency stimulation (~900 stimuli at 1 Hz; Dudek and Bear, 1992; Mulkey and Malenka, 1992). Importantly, most synapses which express LTP also exhibit one or more forms of LTD. Therefore, a key concept is that the synaptic strength of excitatory synapses is bidirectionally modifiable by different patterns of activity, and which is balanced by the excitation and inhibition. Interestingly, Basu and the colleagues reported that CCK-expressing INs are the key modulators of CA1 pyramidal cell plasticity, thus sculpting the information processing (Basu et al., 2013).

Neural Oscillation and Behavioral Relevance

Neural oscillation were first observed by Hans Berger, a neurologist who invented the electroencephalography (EEG), in 1924 (Berger, 1929). The oscillatory signals, arise from the rhythmic or repetitive neural activity, are thought to be a hallmark of neuronal network function in various brain regions (Buzsáki and Draguhn, 2004). And the oscillatory bands cover frequencies from slow oscillations in the delta (0.5–3 Hz) and theta (3–8 Hz) ranges to fast oscillations in the gamma (30–90 Hz) and ultrafast (90–200 Hz) ranges. Intriguingly, the scalp EEG during conscious, waking behavior demonstrates low amplitude, “desynchronized” patterns, whereas states associated with loss of consciousness, such like sleep and anesthesia, exhibit the prominent oscillations (Steriade, 2001; Poulet and Petersen, 2008). In addition, theta oscillations in the hippocampus are thought to be critical for the memory and navigation (Buzsáki, 2005; Buzsáki and Moser, 2013). Moreover, gamma-band rhythmogenesis is inextricably tied to fast-spiking (FS), PV^+ somatic-targeting INs (Bartos et al., 2007; Buzsáki and Wang, 2012), and dysregulated gamma activities can be found in the schizophrenia-like and Alzheimer’s disease mouse models (Del Pino et al., 2013; Verret et al., 2012).

In respect of slow oscillation (<1 Hz), which occur during natural sleep and certain forms of anesthesia, is characterized by rhythmic cycles of synaptic bombardment mediated depolarization and action potentials (Up states), followed by diminution of synaptic inputs, leading to membrane hyperpolarization and cessation of firing (Down states; Haider et al., 2006). The fast changes of synaptic bombardment can control the spike probability of the recipient neurons, and may mediate rapid (milliseconds to seconds) network dynamics (Haider and McCormick, 2009).

The Aims of This Study

Sparse firing of DG GCs is thought to be important for rapid pattern separation and spatial information encoding (Leutgeb et al., 2007; McHugh et al., 2007; Moser et al., 2008). The relatively uniform GCs are supported by a rich diversity of GABAergic INs that provide general inhibition and also temporally regulate GC activity. In the DG, PV-expressing BCs, a class of soma-targeting INs, generate reliable and powerful phasic inhibition (Kraushaar and Jonas, 2000), whereas CCK-expressing INs release GABA in a highly asynchronous manner, thus generating long-lasting dendritic inhibition (Hefft and Jonas, 2005). In contrast, synaptic inhibition provided by other types of GABAergic INs has less been investigated. Furthermore, hippocampal neurons *in vivo* receive the dynamic inputs and the INs fire in bursts, with variable number and frequency of spikes (Pernía-Andrade and Jonas, 2013; Bragin et al., 1995). It is not known how the distinct GABAergic INs respond to and translate the various activities.

MATERIALS AND METHODS

Preparation of Hippocampal Slice

Male Sprague-Dawley rats (postnatal day 16-25) were sacrificed by decapitation without anesthesia, in accordance with national and institutional guidelines. All procedures were approved by the Institutional Animal Care and Use Committee of National Yang-Ming University. The brains were rapidly removed and transferred into oxygenated (95% O_2 and 5% CO_2) ice-cold sucrose saline solution containing (in mM): 87 NaCl, 25 $NaHCO_3$, 1.25 NaH_2PO_4, 2.5 KCl, 10 glucose, 75 sucrose, 0.5 $CaCl_2$ and 7 $MgCl_2$. 300 μm thick transverse slices were sectioned as previous described (Bischofberger et al., 2006b), in oxygenated ice-cold sucrose saline using a vibratome (DTK-1000, Dosaka) and further incubated in oxygenated sucrose saline in a holding chamber (Sakmann and Stuart, 1995) at 34 ˚C for 40 min. Slices were kept in the same chamber at room temperature (23 ± 2 ˚C) until used. During experiments, slices were placed in a recording chamber and superfused with oxygenated artificial cerebral spinal fluid (ACSF) containing (in mM): 125 NaCl, 25 $NaHCO_3$, 1.25 NaH_2PO_4, 2.5 KCl, 25 glucose, 2 $CaCl_2$ and 1 $MgCl_2$. The recording temperature was 23 ± 2 ˚C in the majority of experiments and 35 ± 2 ˚C in a subset (Fig. 14).

Electrophysiology

Recording electrodes (3-7 MΩ) were pulled from borosilicate glass (outer diameter, 1.5 mm; thickness 0.32 mm; Harvard apparatus). Putative INs were first identified at the border between the granule cell layer (GCL) and the hilus by their relatively large somata (diameter > 10 μm) under infrared and differential interference contrast (IR-DIC) microscope (Olympus BX51WI) coupled with an IR-sensitive CCD camera (Hamamatsu, C7500-50) and then confirmed by their electrophysiological characteristics.

Cell-attached recordings (pipette resistance 3-5 MΩ) were made to detect spike responses of single INs (Lien et al., 2006). And extracellular recordings (tip diameter ~10 μm; filled with ACSF; current clamp) were made to detect the population spike (PS) of GCs. The spikes were orthodromically evoked by glass electrodes (tip diameter ~10 μm; filled with ACSF) or bipolar tungsten electrodes (MicroProbes) placed in different DG molecular layers. Trains of ten pulses (100 μs) at 50 Hz at near-threshold intensities were delivered every 5 s using a stimulus isolator (Isoflex, A.M.P.I.). With near-threshold intensities, each train triggered at least one spike in more than 50% of trials and the probability of spike generation triggered by any stimulus didn't exceed 0.8 (Pouille and Scanziani, 2004). Antidromic spikes, distinguished by non-jittering, were excluded.

The method to measure RMP from cell-attached K^+ currents was previously described (Verheugen et al., 1999). After tight-seal was established in the GCs, depolarizing voltage ramps (from command potential = 100 to -200 mV, 20-40 ms) were applied to activate voltage-gated K^+ channels and to establish the K^+ current reversal potential. Between stimulations, the patch was held at -60 mV (command potential = 60 mV) hyperpolarized with respect to RMP to remove possible voltage-dependent "steady-state" inactivation from the voltage-gated K$^+$ channel at the physiological RMP. For analysis of currents evoked by ramp stimulation, a correction was made for a leak component by linear extrapolation of the closed level below the threshold for activation of the voltage-gated current. Passive Cl$^-$ conductance was negligible during this experiment (Verheugen et al., 1999).

For gramicidin perforated-patch recording (voltage clamp), the gramicidin-containing solution was sonicated for 90 s every time before loading. And cell-attached recordings (pipette resistance 4-7 MΩ) were made in the DG GCs. The integrity of the perforated patch was monitored by series resistance (R$_s$) and epifluorescence illumination. The R$_s$ was checked by a small voltage step (-10 mV for 50 ms), every 15 s. Spontaneous breakthrough was identified by an abrupt reduction in R$_s$, accompanied by a sudden fluorescence labeling of the cell body. After stable R$_s$ (50-100 MΩ) was established, GABAergic responses were elicited (15 s interval) by local puffs (~5 psi; 10 ms) of GABA (100 µM) using PicoSpritzer III (Parker Instrumentation) in the presence of kynurenic acid (2 mM). The puffing pipette (tip diameter ~2 µm) was placed in the GCL adjacent (~20 µm) to the recorded soma. Data points in the resulting current-voltage (I-V) relations were fitted with a second order polynomial function to determine the E_{GABA}.

Paired recordings from synaptically coupled presynaptic INs and postsynaptic GCs in the DG were made as described previously (Kraushaar and Jonas, 2000). Presynaptic INs were held near -70 mV in current clamp. One or multiple short (1-ms duration) current pulses were delivered to evoke single or clustered APs. Postsynaptic cells were held at -80 mV in voltage clamp. To induce depolarization-induced suppression of inhibition (DSI), GCs were depolarized to 0 mV for 5 s. Whole-cell patch-clamp recordings were made using a Multiclamp 700B amplifier (Molecular Devices). Pipette capacitances of both electrodes were carefully compensated (by >95%) and R_s was fully compensated using the automatic bridge balance (readouts after compensation were 9-28 MΩ) in current clamp and it was only compensated (~80%) in voltage clamp for perforated-patch. Signals were filtered at 4 kHz using the 4-pole low-pass Bessel filter. The signals of PS were additionally filtered at 200 Hz using the 8-pole high-pass Bessel filter. A Digidata 1440A (Molecular Devices) connected to a personal computer was used for stimulus generation and data acquisition. The PicoSpritzer was triggered by an external TTL pulse generated by Digidata 1440A. The sampling frequency was 10 kHz. Pulse sequences were generated by pClamp 10.2 (Molecular Devices). No correction for liquid junction potentials was made.

Solutions and Drugs

The pipette solution for cell-attached recordings contained (in mM): 141.5 K-gluconate, 13.5 KCl, 0.1 EGTA, 2 $MgCl_2$, 4 Na_2ATP and 10 HEPES. For whole-cell patch-clamp recordings, the intracellular solution for presynaptic cells contained (in mM): 135 K-gluconate, 20 KCl, 2 $MgCl_2$, 4 Na_2ATP, 10 HEPES and 0.4% biocytin. For perforated-patch, the tip-filling intracellular solution contained (in mM): 10 HEPES, 150 KCl and the back-filling solution contained (in mM): 10 HEPES, 150 KCl, Sulforhodamine 101 (20 uM) and gramicidin A (20 µg/ml). For postsynaptic

GC recordings, the intracellular solutions contained (in mM): 15 K-gluconate, 140 KCl, 0.1 EGTA, 2 $MgCl_2$, 4 Na_2ATP, 10 HEPES and 0.4% biocytin; or 135 K-gluconate, 20 KCl, 0.1 EGTA, 2 $MgCl_2$ 4 Na_2ATP, 10 HEPES and 0.4% biocytin; the reason of using different solutions was duo to the need of better signal to noise ratio which could be achieved by increasing the intracellular concentration of Cl^-; for postsynaptic IN recordings, the intracellular solutions contained (in mM): 135 K-gluconate, 20 KCl, 2 $MgCl_2$, 4 Na_2ATP, 10 HEPES and 0.4% biocytin; pH adjusted to 7.3 with KOH. Sulforhodamine 101 and EGTA-AM were purchased from Invitrogen; all other chemicals were purchased from Sigma if not specified.

Post-hoc Immunocytochemistry

After recording, slices were fixed with 4% paraformaldehyde in phosphate-buffered solution (PBS; 0.01 M, pH 7.3). After wash with PBS, slices were incubated with 0.3% Triton-X-100 in PBS (PBST) for 30 min, and subsequently with 10% goat serum in PBS for 2 h. Slices were further incubated with a primary monoclonal antibody against PV (mouse, Swant, 1:5,000; #235) in PBS containing 5% goat serum and 0.3% Triton X-100 for 48 h at 4 ˚C. After wash, the secondary antibody (goat anti-mouse-Alexa 488, 1:500, Molecular Probes) was applied together with Alexa 594-conjugated avidin-D (Molecular Probes) in PBS containing 2% NGS and 0.3% Triton X-100 for 2 h at 4 ˚C. After wash, slides were coverslipped with mounting medium Vectashield® (Vector Laboratories).

Image Acquisition, 3-D Reconstruction and Axonal Density Analysis

For 3-D reconstruction of biocytin-labeled cells, high-resolution two-photon images of INs were acquired. Labeled INs were examined by a two-photon microscope using a pulsed titanium: sapphire laser (Chameleon-Ultra II tuned to 800 nm; Coherent, Portland, OR) attached to a Leica DM6000 CFS (Leica, Wetzlar, Germany) that was equipped with a 63×/0.9 numerical aperture (NA) water immersion objective (objective type HCX APO L). The morphology of the cells was reconstructed from a stack of 51-179 images per cell (voxel size, 271-758 nm in the x-y plane; 1 μm along the z-axis). Image stacks belonging to one cell were imported into the Neuromantic 1.6.3 software (Myatt et al., 2012) for 3-D reconstruction. The axons and dendrites were primarily distinguished from the thickness (axons were relative thinner) and the patterns (axons usually displayed as varicosities or boutons). To quantify the axonal density along the radial axis, we counted the number of intersections made by the axons with lines running parallel to the border between the GCL and the molecular layer and interspaced by 10 μm (Pouille and Scanziani, 2004).

Data Analysis and Statistics

Data were analyzed using Clampfit 10.2 (Molecular Devices) and Prism 5.0 (GraphPad). The synaptic latency was measured from the peak amplitude of the AP to the 10% rise time of the unitary inhibitory postsynaptic current (uIPSC) (Glickfeld and Scanziani, 2006); the decay time constant of the uIPSC was fitted with a single exponential; the coefficient of variation (CV) of the inter-spike intervals (ISIs) was calculated from 1-s spike train elicited in response to current pulse

(+0.6 nA) injection (Lien and Jonas, 2003). The input resistance (R_{in}) was measured by the ratio of the steady-state (average of the last 100 ms) voltage response versus the injected 1-s hyperpolarizing (100 pA) current pulse. The membrane time constant (τ_m) was calculated using a single-exponential fit to the late portion of the voltage change produced by hyperpolarizing (100 pA) current pulse injection in the current clamp mode at the RMP. To estimate the change of the readily releasable pool (RRP) size, AP trains (60 stimuli; 25 Hz) were delivered at 5 s after single and burst stimulations. The RRP size was quantified with a charge integral of the synaptic current (Moulder and Mennerick, 2005; Stevens and Williams, 2007). Linear regression fits to cumulative IPSC area plots after 1 s were back-extrapolated to estimate the cumulative area (RRP charge) at time 0. Data were presented as mean ± standard error of mean (SEM) and n indicates the number of cells or pairs studied. Error bars indicate SEM and were plotted only when they exceeded the respective symbol size. Statistical significance was tested by the Wilcoxon rank-sum or Wilcoxon signed-rank test at the significance level (*P*) as indicated, using Prism 5.0.

RESULTS

Functional and Anatomical Dichotomies between non-FS and FS INs in the DG

To investigate the role of INs in the DG circuitry, I initiated the experiments by establishing whole-cell recordings from GABAergic inhibitory INs located between the GCL and the hilus, then correlating their intrinsic properties with morphologies. According to their firing properties in response to step current injection, GABAergic inhibitory INs were classified as non-fast-spiking (non-FS; Fig. 1A, blue) and fast-spiking (FS) INs (Fig. 1A, red). Non-FS INs exhibited relatively slow and accommodating firing patterns during depolarizing current steps (Fig. 1A, left). The mean firing frequency did not increase monotonically with the injected current intensity (from 0.1 to 1 nA), but rather showed a maximal value (25 ± 4 Hz, n=14) at an intermediate current intensity (0.6 nA; Fig. 1B, blue traces). In contrast, FS INs generated fast, non-accommodating firing patterns (mean firing frequency, 61 ± 4 Hz at 0.6 nA, n=16; Fig. 1A, right) with deep, fast afterhyperpolarization and the mean firing frequency increased monotonically with the current intensity from 0.1 to 1 nA (Fig. 1B, red traces). Non-FS and FS INs also differed significantly in their CV of ISI (non-FS INs, 0.65 ± 0.14, n=15; FS INs, 0.11 ± 0.02, n=15; $P < 0.0005$, Wilcoxon rank-sum test), τ_m (non-FS INs, 40.6 ± 2.7 ms, n=14; FS INs, 21.5 ± 1.5 ms, n=16; $P < 0.0005$, Wilcoxon rank-sum test) and R_{in} (non-FS INs, 447 ± 42 MΩ, n=15; FS INs, 144 ± 8 MΩ, n=15; $P < 0.0005$, Wilcoxon rank-sum test) (Fig. 1C). To further correlate neuronal morphologies with the intrinsic properties of FS and non-FS INs, I filled biocytin into the cells in a subset of recordings and recovered their morphologies after experiments. Anatomical analysis revealed that non-FS and FS INs had distinctive axonal distribution patterns (Fig. 1D_1 and D_2). With the GCL as reference (Fig. 1E), reconstructed non-FS INs had the majority of axonal density distributions outside the GCL (in the ML), whereas FS INs had the highest axonal density distribution within the GCL.

Next, I compared the functional properties of non-FS IN and FS IN output synapses in paired recordings (Fig. 1F). Synaptic connections were identified by evoking uIPSCs in GCs with five brief depolarizing current pulses (1 ms at 25Hz; 5-s interval) applied in presynaptic INs. And the GABAergic responses were verified and abolished by bath application of $GABA_A$ receptor antagonist, gabazine (1 uM), in a subset of experiments (Control, 11.8 ± 2.3 pA; Gabazine, 1.1 ± 0.8 pA; n=4; Fig. 2A,B). Several differences were detected between non-FS IN-to-GC and FS IN-to-GC synapses. First, presynaptic AP half-width of non-FS INs was significantly longer than that of FS INs (non-FS INs, 1.69 ± 0.09 ms, n=10; FS INs, 1.00 ± 0.07 ms, n=8; $P < 0.0005$, Wilcoxon rank-sum test; Fig. 1G). Second, 20-80% rise time (non-FS INs, 1.11 ± 0.08 ms, n=12; FS INs, 0.46 ± 0.03 ms, n=10; $P < 0.0005$, Wilcoxon rank-sum test; Fig. 1G) and decay time constant (non-FS INs, 25.4 ± 2.1 ms, n=12; FS INs, 13.6 ± 0.8 ms, n=9; $P < 0.0005$, Wilcoxon rank-sum test; Fig. 1G) of uIPSCs recorded from pairs of non-FS IN-to-GC synapses were significantly slower than those of FS IN-to-GC synapses. Finally, the synaptic latency was significantly longer for non-FS IN-to-GC synapses than for FS IN-to-GC synapses (non-FS INs, 3.67 ± 0.16 ms, n=11;

FS INs, 1.95 ± 0.14 ms, n=10; $P < 0.0005$, Wilcoxon rank-sum test; Fig. 1F). These results were similar to previous observations (Hefft and Jonas, 2005) and were consistent with a more distal location of non-FS IN terminals on the dendrites of GCs (Fig. 1D$_1$).

Classification of IN Subtypes

Non-FS and FS INs can be further classified into several IN subtypes based on their axonal projection patterns (Han et al., 1993; Hefft and Jonas, 2005). Non-FS INs with their somata at the border between the GCL and the hilus comprise at least three distinct subtypes: the CB$_1$R$^+$INs, also known as CCK$^+$INs, the hilar IN with C/A pathway-associated (HICAP) cells and the hilar IN with PP-associated axon terminals (HIPP) cells. Unlike CB$_1$R$^+$INs in the CA1 area (Glickfeld and Scanziani, 2006), CB$_1$R$^+$INs had their axonal distribution in the IML rather than the GCL (Hefft and Jonas, 2005). Thus, CB$_1$R$^+$INs (6 cells; Fig. 3A$_1$) in this study were identified by asynchronous release (Fig. 3A$_2$), cannabinoid sensitivity (40.6 ± 0.3% of control, n=5 pairs; Fig. 3A$_3$), and their axonal distribution in the IML (Glickfeld and Scanziani, 2006). Cannabinoid sensitivity was tested through the DSI protocol (GCs were depolarized to 0 mV for 5 s). Similar to CB$_1$R$^+$INs, HICAP cells also had the highest density of axons within the IML, (Fig. 3B$_1$). However, in contrast to CB$_1$R$^+$INs, HICAP cells (14 cells) did not display DSI responses (103.4 ± 11.9% of control, n=10 pairs; Fig. 3B$_2$). Unlike CB$_1$R$^+$INs and HICAP cells, HIPP cells (9 cells) had their axonal projection extended to the PP terminal field, whereas its dendrites were restricted to the hilus (Fig. 3C). In addition, four HIPP-like cells, which projected their axons to the OML, but had the dendritic arbor in the ML and the hilus, were observed (Fig. 3D).

In contrast to non-FS INs, FS INs had remarkable axonal projection almost restricted within the GCL (Fig. 3E) and likely comprise two subtypes: AACs and PV$^+$BCs. AACs have prominent radial axon collaterals with vertical rows of axonal terminals, thus also termed chandelier cells, whereas PV$^+$BCs have tangential axonal collaterals with scattered boutons in the GCL (Howard et al., 2005; Hu et al., 2010). In this study, all recovered FS INs were identified as PV$^+$BCs primarily based on their axonal projection pattern and AACs were not present (Fig. 3E and Fig. 4). Summary of morphologically identified INs was shown in Figure 3F.

Differential Recruitment of FS and non-FS INs by Excitatory Afferents

The DG has a distinct laminated structure and receives incoming excitatory inputs from the entorhinal cortex and the hilar regions (Förster et al., 2006; Bartos et al., 2011). The PP from the entorhinal cortex layer II forms a bundle and innervates the distal part of GC dendrites within the outer two thirds of the molecular layer (OML), whereas the C/A afferents, which originate from the mossy cells in the contra- and ipsi-lateral hilar regions, innervate proximal GC dendrites within the inner molecular layer (IML) (Fig. 5A). In addition to GCs, both excitatory afferents target local inhibitory INs, which critically control the GC output. To understand how INs exert their inhibition onto postsynaptic GCs in the normal DG circuitry, it is important to understand not only IN outputs, but also the nature of their inputs. To investigate how excitatory afferents recruit INs, I performed cell-attached recordings from individual INs located in or near the GCL. Putative INs were activated by stimulating the PP with glass or bipolar tungsten electrodes placed in the OML (Fig. 5A; see MATERIALS AND METHODS). Spikes, detected as extracellular AP currents, were recorded from the soma of presumed INs in response to trains of ten electrical stimuli delivered at 50 Hz to the PP. Two populations of INs differed in their responses to the sustained PP afferent stimulation: the first group of INs, termed 'late-onset' cells, had the low firing probability in response to the initial five stimuli and rapidly increased their firing probability over the course of train stimuli (Fig. 5B,D); the second group of INs, termed 'early-onset' cells, preferred to respond to the initial four stimuli and responded less reliably to the latter stimuli (Fig. 5C,D). After cell-attached recordings, whole-cell recordings of the same cells showed that late-onset cells displayed adapting, irregular spiking at lower frequency (36 ± 2 Hz, n=6; Fig. 5B inset), whereas early-onset cells generated non-adapting, high-frequency spike train (63 ± 5 Hz, n=10; Fig. 5C inset) in response to square pulse current (0.6 nA) injection.

To probe the responses of GCs during PP stimulation, population spike (PS) was recorded by extracellular recording electrode placed in the GCL. Interestingly, PS, which might reflect the activity of GCs, exhibited an intermediate pattern between the early-onset and late-onset INs (Fig. 6A,B). The spike probability of PS was gradually increased and reached the highest peak (~20%) during the second and third stimuli, and fell accompanied by climbing spike probability of late-onset INs (Fig. 6 A,B).

In addition to the PP, INs receive C/A afferents, which terminate in the IML (Fig. 5A). Similar to PP activation, sustained stimulation of the C/A afferents sequentially recruited early-onset and late-onset INs. In the early-onset cells, the probability of spiking was highest at the onset of the series and rapidly fell during the sustained afferent stimulation (Fig. 5E,G). In the late-onset cells, the probability of spike generation was low at the onset of the series and slightly increased over the course of train stimuli (Fig. 5F,G). Whole-cell recordings of these two types of neurons also revealed that late-onset cells displayed adapting, non-FS patterns (32 ± 3 Hz, n=8; Fig. 5E inset), whereas early-onset cells exhibited non-adapting, FS patterns (65 ± 5 Hz, n=7; Fig. 5F inset).

Rapid Dynamic Changes of GABA Release in non-FS IN-to-GC Synapses

In neurons *in vivo*, the membrane potential exhibits substantial rapid variations, during all behavioral states, owing to fluctuations in synaptic bombardment (reviewed by Haider and McCormick, 2009). Cortical inhibitory INs *in vivo* fire bursts of APs at gamma frequency range (20 - 50 Hz) during the Up-state or gamma and spindle oscillations (Haider et al., 2006; Massi et al., 2012). It is unclear how the spike timing of INs is translated into their output synapses in different states. To address this question, I made paired recordings between FS or non-FS INs and GCs. Postsynaptic uIPSCs recorded in GCs were evoked by applying brief current pulses to the presynaptic INs. A single AP or a 25-Hz burst of five APs was repetitively applied every 5 s. (Fig. 7A). Synaptic transmission at 5-s interval during periods of either single AP or burst AP complex mode was found to be stable for 8 min in the absence of GABA receptor type B antagonists (Fig. 8A,B). As illustrated in Figure 7B (left traces), non-FS IN-to-GC synapses exhibited small uIPSCs

(11.7 ± 3.0 pA, n=18 pairs) with a larger number of failures (0.54 ± 0.04, n=36 pairs) during single AP stimulations. Interestingly, when non-FS cells fired at bursting complexes, the efficacy (28.0 ± 7.5 pA, n=18 pairs; $P < 0.0005$, Wilcoxon signed-rank test) and reliability (failure rate of IPSC$_1$, 0.24 ± 0.03, n=36 pairs; $P < 0.0005$, Wilcoxon signed-rank test) of neurotransmission robustly increased (Fig. 7B, right traces). When the peak amplitude of the first uIPSC (uIPSC$_1$) was plotted against time, the magnitude was small during single firing modes, whereas the magnitude rapidly increased during burst firing modes (Fig. 7C). On average, the uIPSC$_1$ magnitude increased to 412 ± 67% (n=36; $P < 0.0005$, Wilcoxon signed-rank test; Fig. 7D). Similar results were also found when the mean charge transfer (the charge integral of the synaptic current) per AP was plotted against time during mode transitions (single, 0.18 ± 0.06 pC; burst, 0.55 ± 0.17 pC, n=18; $P < 0.0005$, Wilcoxon signed-rank test; Fig. 7E).

In contrast, FS cells generated relatively reliable and high efficacy of GABA release during single firing modes (Fig. 7F,G). While FS cells fired at burst modes, they maintained stable transmission during burst of 5 APs (Fig. 7F). Unlike the non-FS IN synapses, the uIPSC$_1$ magnitude (single, 12.8 ± 1.5 pA; burst, 12.0 ± 1.8 pA, n=8; P = 0.82, Wilcoxon signed-rank test; Fig. 7H), the failure rate of IPSC$_1$ (single, 0.21 ± 0.06; burst, 0.22 ± 0.06, n=13; $P = 0.67$, Wilcoxon signed-rank test) and the mean charge transfer (single, 0.17 ± 0.02 pC; burst, 0.16 ± 0.01 pC, n=8; $P = 0.31$, Wilcoxon signed-rank test) per AP were unchanged after transition to burst firing modes (Fig. 7I).

Heterogeneity of Dendrite-targeting IN Output Synapses

As illustrated in Figure 3, dendrite-targeting INs are heterogeneous and the properties of most GABAergic synapses between dendrite-targeting INs and GCs are unknown (Hefft and Jonas, 2005). With rigorous anatomical reconstruction, I have identified three subtypes (CB_1R^+, HICAP and HIPP) of dendrite-targeting INs. In agreement with the distance of their axonal termination to the GC soma (see Fig. 3), both uIPSC rise time and decay τ were fast at the CB_1R^+IN-GC synapse, modest at the HICAP-GC synapse, and slow at the HIPP-GC synapse (Table 1). The present study provides, to my knowledge, the first description of their synaptic strength and properties. The main points are as follows. First, the peak amplitude of uIPSC and the charge transfer per AP at the HICAP-GC synapse (1.7 ± 0.5 pA; 0.03 ± 0.01 pC, n=7) are much smaller than those at the CB_1R^+IN-GC synapse (13.5 ± 5.6 pA; 0.2 ± 0.1 pC, n=4) and the HIPP-GC synapse (10.4 ± 8.0 pA; 0.15 ± 0.09 pC, n=3) during basal transmission. Second, the degree (~10-fold) of dynamic change of both CB_1R^+IN and HICAP cell output synapses is greater than that (~1.5 to 3-fold) of the HIPP output synapse during mode-transitions. Third, the mean charge transfer per AP of the CB_1R^+IN-GC synapse (2.41 ± 1.39 pC, n=4) is substantially larger than those of the HICAP-GC (0.31 ± 0.08 pC, n=7), HIPP-GC (0.48 ± 0.32 pC, n=3), and PV^+BC-GC (0.29 ± 0.07 pC, n=4) synapses during the burst mode, indicating that CB_1R^+IN-mediated asynchronous release provides the main inhibitory control onto GCs.

Dynamic GABA Release is Sensitive to Presynaptic Activity Patterns and Ca^{2+} Buffers

The synaptic strength at non-FS IN-to-GC synapses was rapidly switched from low to high release during mode transitions, whereas the dynamics of FS IN-to-GC synapses was relatively independent of presynaptic activity. For non-FS INs, the marked increase in GABA release suggests that the probability of release rapidly increased during AP bursts, which persisted until the first AP of the next burst at five seconds later. To further examine the presynaptic activity dependence at non-FS IN-to-GC synapses, I prolonged the inter-burst interval from five to ten seconds (Fig. 9A). As illustrated in Figure 9B, the uIPSC_1 magnitude and the mean charge transfer of per AP were greatly reduced. Overall, the uIPSC_1 magnitude and the mean charge transfer per AP decreased to 60 ± 8% (from 30.0 ± 11.3 pA to 18.9 ± 7.7 pA, n=9; $P < 0.05$, Wilcoxon signed-rank test; Fig. 9C) and 71 ± 7% (from 0.66 ± 0.28 pC to 0.41 ± 0.17 pC, n=9; $P < 0.05$, Wilcoxon signed-rank test; Fig. 9D), respectively. In contrast, both the failure rate of uIPSC_1 (from 0.28 ± 0.07 to 0.49 ± 0.10, n=9; $P < 0.05$, Wilcoxon signed-rank test; Fig. 9E) and the multiple-pulse ratio ($\text{uIPSC}_5/\text{uIPSC}_1$ from 0.54 ± 0.09 to 0.94 ± 0.16, n=9; $P < 0.05$, Wilcoxon signed-rank test) were significantly increased (Fig. 9F). These results confirm that the use-dependent effects were generated at a presynaptic locus.

Residual elevation of presynaptic $[Ca^{2+}]_i$ as well as loose coupling between Ca^{2+} sources and synaptic vesicles may contribute to activity-dependent facilitation of GABA release during burst activities (Zucker and Regehr, 2002; Bucurenciu et al., 2008; Jonas and Vyleta, 2012). To test this hypothesis, I applied the acetoxymethylester form of EGTA (EGAT-AM, 10 μM), a slowly acting, membrane-permeable Ca^{2+} chelator to interfere with the coupling between endogenous Ca^{2+} and synaptic vesicles (Bucurenciu et al., 2008; Jonas and Vyleta, 2012). The EGTA-AM loaded into the cell can be de-esterified by endogenous esterases and the de-esterified EGTA can accumulate to millimolar levels as opposed to the micromolar concentration of the EGTA-AM in the bath (Zucker and Regehr, 2002). A representative recording showed that after 5-min bath application of EGTA-AM, the uIPSC_1 magnitude during burst firing markedly decreased (from 247.0 ± 31.1 pA to 54.7 ± 11.6 pA; Fig. 10A$_1$,A$_2$). On average, the uIPSC_1 magnitude decreased to $43 \pm 7\%$ (from 426.0 ± 209.5 pA to 158.1 ± 69.8 pA, n=6; $P < 0.05$, Wilcoxon signed-rank test; Fig. 10B) in the presence of EGTA-AM. A similar effect on uIPSC was found during the period of single spiking (control, 23.8 ± 9.9 pA; EGTA-AM, 5.3 ± 1.8 pA; n=5; Fig. 11A). Consistent with the chelator effects on the presynaptic release machinery, the failure rate of the uIPSC_1 during bursting spiking increased from 0.18 ± 0.08 to 0.57 ± 0.07 (n=6; $P < 0.05$, Wilcoxon signed-rank test; Fig. 10C) and the multiple-pulse ratio ($\text{uIPSC}_5/\text{uIPSC}_1$) increased from 0.39 ± 0.10 to 0.76 ± 0.19. (n=6; $P < 0.05$, Wilcoxon signed-rank test; Fig. 10D), whereas the CV^{-2} of uIPSC_1 amplitude was reduced (from 6.25 ± 4.12 to 2.01 ± 0.99; $P < 0.05$, Wilcoxon signed-rank test; 6 pairs, respectively).

Previous studies showed that GABA release at FS IN-GC synapses is insensitive to the slow Ca^{2+} chelator EGTA, suggesting that Ca^{2+} source and Ca^{2+} sensor are tightly coupled at this synapse (Hefft and Jonas, 2005; Bucurenciu et al., 2008). In agreement with those of Hefft and Jonas (2005) and Bucurenciu et al. (2008), bath application of EGTA-AM had little effect on FS IN synapses during single spiking (control, 398.2 ± 147.2 pA; EGTA-AM, 375.8 ± 126.7 pA; n=3; Fig. 11B). Similarly, the $uIPSC_1$ was not changed in the presence of EGTA-AM during burst spiking (control, 642.7 ± 27.2 pA; EGTA-AM, 587.6 ± 24.0 pA; Fig. 10E_1, E_2). On average, the $uIPSC_1$ magnitude before and after EGTA-AM application was unchanged (control, 369.5 ± 140.0 pA; EGTA-AM, 359.3 ± 114.3 pA; n=3; Fig. 10F). Consistently, there were no changes of failure rate (control, 0.015 ± 0.008; EGTA-AM, 0.009 ± 0.006; n=3; Fig. 10G) and the multiple-pulse ratio (control, 0.57 ± 0.04; EGTA-AM, 0.50 ± 0.06; n=3; Fig. 10H). As non-FS IN output synapses are markedly more sensitive to Ca^{2+} chelators than FS IN output synapses, our results suggest residual presynaptic $[Ca^{2+}]_i$ and/or loose coupling between Ca^{2+} sources and synaptic vesicles in non-FS IN terminals.

The RRP Size Increased during Periods of Burst Firing

In addition to increasing the probability of release, a recent study (Thanawala and Regehr, 2013) shows that presynaptic Ca^{2+} accumulation may increase neurotransmitter release in part by increasing the size of the RRP. To test the contribution of this mechanism, I depleted the RRPs in non-FS IN-GC pairs at 5 s after periods of single and burst AP firing using AP trains (Fig. 12A) and then compared the change of the RRP charge using cumulative methods (Moulder and Mennerick, 2005; Rizzoli and Betz, 2005; Stevens and Williams, 2007; Thanawala and Regehr, 2013).

As illustrated in Figure 12B, the uIPSCs during periods of single AP firing were small. After obtaining stable release during periods of single AP firing, AP trains of 60 stimuli at 25 Hz were delivered. The synaptic responses to the first 5 APs were small and then transiently increased during the train, but soon depressed and reached an apparent steady state. Notably, synaptic currents displayed synchronous and asynchronous release. After the recovery from train-induced depletion, INs were then stimulated in the burst mode. In agreement with non-FS IN output synapses, the uIPSC rapidly increased after transition to burst firing and then reached a steady state. To deplete the RRP, the same AP trains were delivered to INs. As illustrated in Figure 12C, synaptic responses were initially large, but rapidly depressed and reached an apparent steady state over the course of 60 stimuli, indicating the rapid depletion of the RRP. Furthermore, synaptic responses showed similar build-up of asynchronous release during AP trains (Fig. 12C). To account for asynchronous release during AP trains, I made cumulative area plots from the 25 Hz trains (Moulder and Mennerick, 2005; Stevens and Williams, 2007). The data set consisted of charge integrals of total synaptic charge transfer and a line of best fit was calculated by linear regression (Fig. 12D). The average RRP charge estimated from the cumulative area at time 0 was 7.9 ± 3.3 pC (n=7) during single firing and markedly increased to 26.4 ± 7.4 pC (n=7), a more than 3-fold increase during the burst stimulation ($P < 0.05$, Wilcoxon signed-rank test; Fig. 12E).

Attenuation of Rapid Dynamic Change of GABA Release by 4-AP

Unlike the release-independent short-term plasticity found at FS IN-to-GC synapses (Kraushaar and Jonas, 2000), rapid dynamic changes of non-FS IN-to-GC synapses are presynaptic activity- and release-dependent. I next asked whether increasing presynaptic spike duration, and therefore driving more Ca^{2+} into terminals, could further increase the probability of release and in turn decrease the extent of the dynamic switch. I inhibited voltage-gated K^+ channels with 30 μM 4-aminopyridine (4-AP). Bath-application of 4-AP slightly increased the somatic AP half-duration (control, 1.60 ± 0.07 ms; 4-AP, 1.91 ± 0.14 ms, n=6; $P = 0.06$, Wilcoxon signed-rank test) and preferentially increased the uIPSC$_1$ magnitude during single AP modes (Fig. 13A$_1$,A$_2$). On average, the degree of the dynamic switch of the uIPSC$_1$ magnitude was reduced in the presence of 4-AP. (control, 8.58 ± 1.08 folds; 4-AP, 2.87 ± 0.86 folds; n=6; $P < 0.05$, Wilcoxon signed-rank test; Fig. 13C). Notably, although the multiple-pulse ratio (uIPSC$_5$/uIPSC$_1$) decreased (control, 0.58 ± 0.15; 4-AP, 0.19 ± 0.04; 6 pairs, respectively; $P < 0.05$, Wilcoxon signed-rank test; Fig. 13D) in the presence of 4-AP, the uIPSC$_1$ magnitude during burst AP modes was unchanged (see DISCUSSION).

I also tested for 4-AP effect on FS IN-to-GC synapses. In contrast to non-FS IN-to-GC synapses, bath-application of 4-AP at low concentrations had little effect on the uIPSC$_1$ magnitude during both single and burst AP modes (Fig. 13B$_1$,B$_2$). On average, the degrees of the dynamic switch of the uIPSC$_1$ magnitude in control and in the presence of 4-AP were 1.04 ± 0.05 and

1.12 ± 0.05 folds (4 pairs, Fig. 13C), respectively. Consistently, the multiple-pulse ratio (uIPSC_5/uIPSC_1) was unchanged (control, 0.44 ± 0.06; 4-AP, 0.39 ± 0.04; 4 pairs, respectively; Fig. 13D). As non-FS IN output synapses are markedly more sensitive to 4-AP at low concentrations than FS IN output synapses, our results suggest differential expression of K^+ channels between FS and non-FS IN terminals.

Rapid Dynamic Changes of Dendritic Inhibition is Preserved at Near-physiological Temperature

Cortical inhibitory INs *in vivo* discharge bursts of APs at gamma frequency range during the Up-state (Massi et al., 2012). Although the natural firing pattern of INs in the DG remains to be determined, I tested whether dendrite-targeting INs fired in *in vivo* recorded discharge patterns exhibited rapid dynamic release during bursting complexes. To mimic the physiological activity, INs were stimulated for 20 s at near-physiological temperature using an IN spike train (shown with hash marks in Fig. $14A_1$,B_1) recorded from anesthetized rats as the stimulation protocol. The stimulation protocol comprised variable stimuli at 30-90 Hz frequency (cell code LK10c from Massi et al., 2012). At 35 ± 2 ˚C, rapid dynamic release from dendrite-targeting IN output synapses during mode transitions was preserved. As illustrated in Figure $14A_1$, the efficacy of neurotransmission was low during low-frequency AP stimulation, but was greatly enhanced during clustered AP stimulation. Figure $14A_2$ illustrates that single APs did not reliably generate postsynaptic responses in contrast to AP bursts. On average, the uIPSC_1 magnitude and charge transfer per AP increased to 523 ± 122% (n=6 pairs; $P < 0.05$, Wilcoxon signed-rank test; Fig. 14C) and 568 ± 153% (n=6 pairs; $P < 0.05$, Wilcoxon signed-rank test; Fig. 14D), respectively. In contrast, soma-targeting INs maintained stable and reliable release during single to burst AP transitions (Fig. 14B_1,B_2). On average, the uIPSC$_1$ and charge transfer per AP were unchanged (uIPSC$_1$, 86 ± 4%; charge transfer per AP, 96 ± 5%; n=4 pairs; Fig. 14C,D). Under the same conditions tested, the substantial difference between dendrite- and soma-targeting IN output synapses was preserved at 35 ± 2 ˚C (Fig. 14C,D). Thus, rapid dynamic changes of GABA release from dendrite-targeting IN terminals occurs at physiological temperature and with behaviorally relevant stimulation patterns. As dendrite-targeting INs provide a rapid fluctuating output, they could efficiently change the gain of input-output relations of GCs *in vivo* (Hefft and Jonas, 2005).

Determine the GABAergic Action in the DG of Juvenile Rat

In development, there can be a transition of action of GABA from excitatory to inhibitory or shunting (Ben-Ari, 2002). To examine the action of GABA in the developing DG, I measured the RMP and E_{GABA} of GCs by noninvasive approaches (See MATERIALS AND METHODS; Verheugen et al., 1999; Ebihara et al., 1995). Cell-attached recordings were made in the DG GCs and CA1 pyramidal neurons (PNs). A command voltage ramp (+100 to -200 mV) elicited the passive (linear) and active K^+ currents (Fig. 15A). RMP was estimated by the command voltage corresponding to the reverse time of active K^+ currents (Fig. 15A). Consistent with previous observations, GCs displayed relatively hyperpolarized RMP as compared with other types of neurons (GCs, -90.0 ± 2.3 mV, n=7; CA1 PNs, -70.7 ± 2.7 mV, n=6; $P < 0.005$, Wilcoxon rank-sum test; Fig. 15A,B; Staley and Mody, 1992; Schmidt-Hieber et al., 2007). On the other hand, estimation of E_{GABA} were done by perforated-patch recordings in the GCs. After tight-seal and stable R_s was established without spontaneous breakthrough, GCs were voltage clamped at -100 to -50 mV. The GABAergic responses were elicited by local puffs of GABA (100 μM; Fig. 15C). The E_{GABA} of GCs was relatively depolarized (-77.7 ± 0.3 mV, n=3; Fig. 15C,D) but still below the AP threshold (Schmidt-Hieber et al., 2004; Krueppel et al., 2011). Together, these results suggested the shunting effect of GABA in the DG.

Functional Connectivity and Specificity of the Synaptic Dynamic Switch

To further determine whether the rapid dynamic switch of GABA release is dependent on postsynaptic cell type, I recorded from non-FS IN-to-non-FS IN, non-FS IN-to-FS IN, FS IN-to-FS IN, and FS IN-to-non-FS IN pairs (Fig. 16A_1,B_1). Regardless of the cell type of postsynaptic targets, the rapid dynamic switch of GABA release was exclusively detected at pairs with non-FS cells as presynaptic neurons, suggesting presynaptic cell type-specificity (Fig. 16A_2,B_2). The uIPSC$_1$(Single/Burst) ratios at non-FS IN-to-GC and non-FS IN-to-non-FS IN synapses were 0.24 ± 0.03 (n=36) and 0 (n=2), respectively (Fig. 16A_3). By contrast, the uIPSC$_1$(Single/Burst) ratios at FS IN output synapses (FS IN-to-GC, 1.10 ± 0.09, n=13; FS IN-to-non-FS IN, 1.05 ± 0.11, n=5; FS IN-to-FS IN, 1.05, n=2) were close to 1 (Fig. 16B_3). Further analyses of synaptic dynamics revealed that FS IN output synapses exhibited short-term depression when tested at 25 Hz

($\mathrm{uIPSC}_5/\mathrm{uIPSC}_1$: 0.51 ± 0.04 at FS IN-to-GC pairs, n=12; 0.54 ± 0.10 at FS IN-to-non FS IN pairs, n=5; 0.50 at FS IN-to-FS IN pairs, n=2). In contrast, non-FS IN output synapses appeared to display a functional divergence: the non-FS IN-to-GC synapses showed short-term depression ($\mathrm{uIPSC}_5/\mathrm{uIPSC}_1$: 0.63 ± 0.06, n=29), whereas non-FS IN-to-non FS IN synapses exhibited little short-term plasticity ($\mathrm{uIPSC}_5/\mathrm{uIPSC}_1$: 1.10, n=2) under the same stimulation condition. Notably, no functional connectivity was detected at non-FS IN-to-FS IN pairs in the present study (11 pairs, Fig. 16A_4).

My study also revealed cell-type specificity of the functional connectivity (Fig. 16A_4,B_4). Non-FS INs preferentially formed functional connections with GCs (38.6%; 151 of 391 pairs), but rarely formed connections with non-FS INs (3.1%; 2 of 64 pairs) and FS INs (0%; 0 of 11 pairs). In contrast, FS INs frequently and almost equally formed connections with GCs (57.7%; 30 of 52 pairs), non-FS INs (45.4%; 5 of 11 pairs), and FS INs (50%; 2 of 4 pairs).

DISCUSSION

Summary

GABAergic INs play a critical role in controlling neuronal activity through their axonal projection to distinct domains of target neurons. In addition to projection patterns, several distinct molecular and functional attributes underscore the differences between soma- and dendrite-targeting INs. Here, I report a novel synaptic dichotomy between the two IN (soma- versus dendrite-targeting) classes in the DG. Notably, despite considerable heterogeneity in dendrite-targeting IN properties and projection patterns, they all exhibit a rapid switch in GABA release between periods of sparse spiking activity and periods of enhanced activity at both 23 and 35 ˚C in contrast to soma-targeting INs (Table 1).

To summarize two major findings of this study, differential recruitment of INs and activity-dependent dendritic inhibition, I propose the diagram of activity-tuned dentate circuitry (Fig. 17). During the resting state, sparse cortical activity can only activate the FS, perisomatic-targeting IN (PI) and transmit the somatic GABA, whereas the non-FS, dendrite-targeting IN (DI) is silenced (Fig. 17A). In the moderate activity state, elevated inputs can both recruit the DI and PI. Nevertheless, single AP is not sufficient to generate robust dendritic inhibition (Fig. 17B). Once the massive and sustained inputs arriving, it can give rise to bursting spike in the DI and subsequently exert the magnificent dendritic inhibition (Fig. 17C).

IN Dichotomy in Distinct Microcircuits

Similar to my present study, a number of functional and anatomical dichotomies have been shown to exist between two BC classes, PV$^+$BCs and CCK$^+$BCs, in the hippocampus proper (see review by Armstrong and Soltesz, 2012). However, these two circuits, CA areas and DG, differ in some respects. First, INs in the DG exert shunting inhibition and depolarize GCs at rest, whereas INs in the CA1 and CA3 areas generate hyperpolarizing inhibition onto pyramidal cells (Glickfeld et al., 2009; Bazelot et al., 2010; Chiang et al., 2012). Second, unlike the remarkable axonal distribution of CB1R$^+$ INs within the IML, CCK$^+$ (also termed CB1R-containing) BCs in the CA1 area primarily synapse onto the somata of their principal cell targets with a slight shifted distribution toward the proximal dendrites (Glickfeld and Scanziani, 2006). Third, PV$^+$BC input, but not CCK$^+$BC input, in the CA1 area is selectively modulated by the hyperpolarization-activated chloride channel, ClC-2 (Földy et al., 2010). Such synapse-specific expression of ClC-2 is not present in the DG. Overall, these differences point to circuit-specific network function of INs.

Classification of Dendrite-targeting INs

As compared with soma-targeting INs, dendrite-targeting INs are more complex and heterogeneous. In this study, I focus exclusively on dendrite-targeting INs with their somata at the border between the GCL and the hilus. According to previous studies (Han et al., 1993; Freund and Buzsáki, 1996), there are three major subtypes (i.e. CB1$^+$INs, HICAP and HIPP cells). However, I observed a small population of INs, not compatible with these classifications. In this study, INs with their axon projection to the OML were classified as HIPP cells. Among them, the majority (9/13 cells) of HIPP cells did display their dendrites strictly in the hilus, in agreement with that of Han et al. (1993). In other words, I observed four atypical HIPP-like cells, which project their axons to the OML, but have the dendritic arbor in the ML. Furthermore, I found that 7/13 of HIPP cells exhibit axon collaterals in the IML in addition to the OML. The possible explanation is that our slices were cut from the hippocampus at some septo-temporal level where the IML may be very narrow or the angle of sectioning relative to layer boundaries may influence the appearance of the axon. It is also likely that those atypical HIPP cells represent a novel subtype of INs. The features of Petilla nomenclature (Ascoli et al., 2008) may provide a stepping stone towards a future classification of these atypical INs.

In this study, all of the INs are recorded in the hilus and GCL. Still, some other types of INs in the DG have not been approached. Such as two different types of DI, neurogliaform cell (NGC) and molecular layer perforant path-associated (MOPP) cell are located in the ML (Armstrong et al., 2011; Li et al., 2013). Both they are thought to play a role in dentate feed-forward inhibition. In addition, one type of specialized PI, AAC, synapses onto the axon initial segment (AIS) of GCs and may control the AP generation (Buhl et al., 1994). Whether these cells follow the activity-dependent regulation of dendritic inhibition needs further investigations.

Differential Recruitment of Soma- and Dendrite-targeting INs by PP and C/A Inputs

Differential recruitment of GABAergic INs is dependent on IN subtypes. Differences in the input synapse properties, dendritic architecture, and membrane properties, as well as the rich repertoire of plasticity mechanisms contribute to this diversity (Geiger et al., 1997 Pouille and Scanziani, 2004). In the DG, FS INs receive direct excitation from the PP pathway followed by di-synaptic recurrent excitation *via* the PP-GC mossy fiber pathway. Slow distal PP-mediated EPSP supports summation, whereas rapid MF mediated-EPSP defines a narrow time window for AP generation. The delay between the PP and the MF inputs of ~10 ms corresponds well to the latency along the di-synaptic excitatory path PP-GC-BC (Sambandan et al., 2010). Synaptic dynamics of GC-to-BC synapses displays pronounced multiple-pulse depression. When presynaptic GCs fired at 50 Hz, the successive third EPSP recorded in BCs rapidly diminished to ~20% of the first EPSP (Geiger et al., 1997). This is in agreement with the high probability of spike occurrence of FS cells during the initial three 50-Hz stimulations (Fig. 5D). Therefore, summation of PP-mediated EPSP and recurrent MF-mediated EPSP contribute to the early recruitment of FS INs. Paired recordings of FS IN-to-GC and GC-to-FS IN connections indicate that these INs can perform feed-forward and feedback somatic inhibition (Geiger et al., 1997; Kraushaar and Jonas, 2000).

It remains to determine whether non-FS INs receive the recurrent (feedback) MF input from GCs. Non-FS INs, which are dendrite-targeting INs, may only receive the PP and C/A inputs and perform feed-forward dendritic inhibition. Thus, a long τ_m and a lack of rapid MF-mediated EPSP may favor integration of synaptic inputs over a longer time scale and therefore these IN types are preferentially activated during later period by repetitive stimuli.

Taken together, early activation of FS INs and delayed recruitment of non-FS INs may result in orchestrating the firing time window of GCs (Fig. 6). Therefore, setting the spike timing of GCs may help the theta-band rhythmogenosis and contribute to sparse temporal coding of information in the dentate gyrus (Montgomery et al., 2009; Pernía-Andrade and Jonas, 2013).

Possible Mechanisms by which Presynaptic Activity Regulates the Short-term Presynaptic Facilitation

Cortical INs display a specific mode of firing composed of sparse and clustered APs (Goldberg et al., 2008). In my experimental conditions, while firing of dendrite-targeting INs is switched from the single to the burst spiking mode, the probability of release is rapidly enhanced, suggesting that AP bursts induced a long-lasting increase in $[Ca^{2+}]_i$ in the terminals and the residual $[Ca^{2+}]_i$ enables the enhancement of subsequent GABA release. Accumulation of residual $[Ca^{2+}]_i$ may be attributed to the loose coupling between Ca^{2+} sources and release sensors (Eggermann et al., 2012) and/or saturation of endogenous Ca^{2+} buffers (Fioravante and Regehr, 2011).

This hypothesis can be tested by introducing the slowly acting, but high affinity Ca^{2+} buffer EGTA into presynaptic terminals (Eggermann et al., 2012). Indeed, the effect of EGTA-AM strongly depress GABA release in dendrite-targeting INs. This is in great contrast to the lack of effect of the EGTA-AM on soma-targeting IN output synapses, where Ca^{2+} channels and Ca^{2+} sensors are tightly coupled (Hefft and Jonas, 2005; Bucurenciu et al., 2008). Here, a potential caveat should be noted. I cannot exclude a contribution of other variables that can affect neurotransmission by EGTA-AM; for instance, the treatment could affect the release of another substance that is selectively modulating synaptic transmission at non-FS IN output synapses, but not FS IN output synapses.

Changes of AP shape can regulate release probability. By prolonging AP duration in the terminals, the probability of release may increase *via* the enhancement of presynaptic Ca^{2+} influx. In agreement with this view, inhibition of voltage-gated K^+ channels with 4-AP increases AP duration and greatly enhances single AP-evoked uIPSCs. A significant decrease in multiple-pulse ratio (Fig. 13D) confirmed that 4-AP enhances presynaptic release, thus reducing the extent of dynamic change during mode transitions. A lack of 4-AP effect on the enhancement of $uIPSC_1$ amplitude during the burst mode suggests that other activity-dependent gating mechanisms may be involved in regulating neurotransmission (Brody and Yue, 2000; also see Discussion in Kraushaar and Jonas, 2000). The non-FS IN output synapses are markedly more sensitive to 4-AP at low concentrations than FS IN output synapses. According to previous observations, the cortical PV^+INs have relatively lower expression of voltage-gated K^+ channel, shaker-related subfamily, member 3 (Kv1.3), which can be blocked by 4-AP at low concentrations (Coetzee et al., 1999), than other types of INs (Duque et al., 2013). Together, these results suggest differential expression of Kv1.3 between FS and non-FS IN terminals in the DG.

As indicated by an increase in multiple-pulse ratio (Figs. 9 and 10), the reduction of burst-induced IPSC amplitude by the prolonged inter-burst interval or EGTA-AM appears to be a result of a decrease in the probability of the release. However, a recent study (Thanawala and Regehr, 2013) shows that alterations in presynaptic calcium influx can also change the effective RRP size. Indeed, I found that the RRP is markedly increased during periods of bursting firing. And it may be also caused by the loose coupling of calcium channel and vesicles (Thanawala and Regehr, 2013). Thus, the calcium dependence of rapid enhancement of GABA release is likely determined by the combined calcium dependencies of the release probability and the effective size of the RRP.

Finally, in addition to those discussed above, I still cannot exclude other mechanisms here, such as use-dependent increases in presynaptic Ca^{2+} currents (Ishikawa et al., 2005) or activation of presynaptic receptors (Ruiz et al., 2010).

Synapse Selectivity in the DG

The connectivity of non-FS IN onto different types of target cells in the DG suggests target-cell selectivity. The probability of finding a synaptic connection between non-FS INs and GCs is considerably higher than those in non-FS IN-to-non-FS IN and non-FS IN-to-FS IN pairs (Fig. 16A4). In contrast, the connectivity of FS IN onto target cells is relatively independent of target cell type (Fig. 16B4). Interestingly, nonrandom local circuits have been reported previously in the DG (Larimer and Strowbridge, 2008). Mossy cells in the hilus show profound synapse selectivity: 87.5% of their intralamellar excitatory connections are exclusively onto hilar INs (mossy cell-to-IN connectivity is 6%; 7/114 cells) and 12.5% of their intralamerllar excitatory connections (mossy cell-to-mossy cell connectivity is 0.5%; 1/206 cells) are onto mossy cell. Similarly, hilar INs also show high synapse selectivity and primarily synapse onto mossy cells (81% of inhibitory connections; hilar IN-to-mossy cell connectivity is 15%) with relatively few connections (19% of inhibitory connections; hilar IN-to-hilar IN connectivity is 6%) onto other hilar INs.

Pathophysiological Aspects of Dynamic Switches of GABA Release

Severely neuronal loss can be caused by overexcitation of certain cell populations in epilepsy. Particularly, the hilar interneurons are found to be the most vulnerable target (Sloviter, 1987). And it has been proposed that Ca^{2+} buffering capacity may be an important factor contributing to neuronal vulnerability facing excessive activity (Sloviter, 1989; Freund et al., 1991; Liao and Lien, 2009). My present study implies that the dendrite-targeting INs in DG may have weak Ca^{2+} handling properties which can account for selective vulnerability to seizure activity. Indeed, intracellular loading calcium chelator can protect hilar cells from prolonged stimulation-mediated damage (Scharfman and Schwartzkroin, 1989).

Histological studies reveal that most degenerated neurons are mossy cell and hilar INs, whereas both PV-expressing and CCK-expressing (also known as CB_1R^+ cell; Katona et al., 1999) INs are relative resistant to epilepsy (Sloviter, 1987; Sloviter, 1989; Buckmaster and Jongen-Rêlo, 1999). In this study, I find that dendrite-targeting INs exert powerful inhibition during burst-mode and it is primarily contributed by CB_1R^+BC, HICAP cells and modest part from HIPP cells. Hence, excessive excitatory activity may enhance dendritic inhibition, which is a compensatory feed-back mechanism, in the early stage of epilepsy. However, progressive loss of hilar INs which dampens dendritic inhibition by weakening the compensatory mechanism during the progress of epilepsy. Although CB_1R^+BC is not susceptible to epilepsy, excessive inputs can drive endocannabinoid-mediated retrograde signaling and cause presynaptic suppression of inhibition (Glickfeld and Scanziani, 2006). Diminished dendritic inhibition would therefore affect network functions.

Given that the dynamics of cortical activity is exquisitely controlled by the excitatory-inhibitory balance (Shu et al., 2003; Hasenstaub et al., 2005; Haider et al., 2006), loss of dendritic inhibition can explain the increased firing rate and lengthened duration of Up-states, which are thought to be associated with epileptogenicity, in epileptic animals (Gerkin et al., 2010; Bragin et al., 2012). Nevertheless, the pathological role of alterations of Up-Down state remains to be investigated in the further study.

Physiological Significance of Dynamic Switches of Dendritic Inhibition in Network Function

Sparse dentate activity is thought to be important for pattern separation and spatial information encoding (Leutgeb et al., 2007; McHugh et al., 2007; Moser et al., 2008). Multiple cellular mechanisms are coordinated for sparse activation of GCs. First, GC dendrites act as strong voltage attenuators. Synaptic input from the entorhinal cortex strongly attenuates along GC dendrites (Schmidt-Hieber et al., 2007; Krueppel et al., 2011). Second, GC dendritic properties are linear integrators. GC dendrites summate synaptic inputs linearly and are not designed for highly efficient synchrony detection (Krueppel et al., 2011). Third, GC dendrites lack dendritic spikes that would allow them to be more efficiently to bring EPSPs to AP threshold (Krueppel et al., 2011). Finally, GCs have relatively hyperpolarized RMP as compared with other types of neurons and relatively depolarized but shunting E_{GABA} as compared with the RMP (Fig. 15; Schmidt-Hieber et al., 2007; Chiang et al., 2012). Beyond the cellular level, what is the circuit mechanism that contributes to the quiescent nature of GCs? Here, I show that GCs are controlled by the powerful dendritic inhibition during periods of intense activity. This novel finding not only provides an important bridge between the fields of synaptic short-term plasticity and hippocampal network states and but also lends a considerable support for a critical role of dendritic inhibitory circuits in gating the information transfer from the cortex to the hippocampus. GABAergic INs exert shunting inhibition onto GCs in the adult brain (Chiang et al., 2012). Our modeling and experimental studies have demonstrated that the impact of a GABAergic input depends upon its spatiotemporal relationship to other depolarizing inputs (Chiang et al., 2012). Given that the E_{GABA} is more depolarized to the resting membrane potential of GCs, but remains hyperpolarized to the AP threshold, it can be expected that burst spiking of dendrite-targeting INs during the Up-state may promote dendritic excitability, but also exert powerful shunting inhibition to limit the degree of dendritic depolarization.

Together, a rapid switch on/off of dendritic inhibition during state-transitions can prevent over-excitation of GCs and effectively control the total amount of signal transfer from the entorhinal cortex to the hippocampus under normal conditions.

REFERENCES

Abbott LF, Regehr WG (2004) Synaptic computation. Nature 431:796-803.

Abel T, Nguyen PV, Barad M, Deuel TA, Kandel ER, Bourtchouladze R (1997) Genetic demonstration of a role for PKA in the late phase of LTP and in hippocampus-based long-term memory. Cell 88:615-626.

Armstrong C, Szabadics J, Tamás G, Soltesz I (2011) Neurogliaform cells in the molecular layer of the dentate gyrus as feed-forward γ-aminobutyric acidergic modulators of entorhinal-hippocampal interplay. J Comp Neurol 519:1476-1491.

Armstrong C, Soltesz I (2012) Basket cell dichotomy in microcircuit function. J Physiol 590:683-694.

Acsády L, Kamondi A, Sík A, Freund T, Buzsáki G (1998) GABAergic cells are the major postsynaptic targets of mossy fibers in the rat hippocampus. J Neurosci 18:3386-3403.

Ascoli GA, Alonso-Nanclares L, Anderson SA, Barrionuevo G, Benavides-Piccione R, Burkhalter A, Buzsáki G, Cauli B, Defelipe J, Fairén A, Feldmeyer D, Fishell G, Fregnac Y, Freund TF, Gardner D, Gardner EP, Goldberg JH, Helmstaedter M, Hestrin S, Karube F, et al. (2008) Petilla terminology: nomenclature of features of GABAergic interneurons of the cerebral cortex. Nat Rev Neurosci 9:557-568.

Augustine GJ (2001) How does calcium trigger neurotransmitter release? Curr Opin Neurobiol 11:320-326.

Azevedo FA, Carvalho LR, Grinberg LT, Farfel JM, Ferretti RE, Leite RE, Jacob Filho W, Lent R, Herculano-Houzel S (2009) Equal numbers of neuronal and nonneuronal cells make the human brain an isometrically scaled-up primate brain. J Comp Neurol 513:532-541.

Bach ME, Hawkins RD, Osman M, Kandel ER, Mayford M (1995) Impairment of spatial but not contextual memory in CaMKII mutant mice with a selective loss of hippocampal LTP in the range of the theta frequency. Cell 81:905-915.

Bartos M, Vida I, Frotscher M, Geiger JR, Jonas P (2001) Rapid signaling at inhibitory synapses in a dentate gyrus interneuron network. J Neurosci 21:2687-2698.

Bartos M, Vida I, Jonas P (2007) Synaptic mechanisms of synchronized gamma oscillations in inhibitory interneuron networks. Nat Rev Neurosci 8:45-56.

Bartos M, Alle H, Vida I (2011) Role of microcircuit structure and input integration in hippocampal interneuron recruitment and plasticity. Neuropharmacology 60:730-739.

Basu J, Srinivas KV, Cheung SK, Taniguchi H, Huang ZJ, Siegelbaum SA (2013) A cortico-hippocampal learning rule shapes inhibitory microcircuit activity to enhance hippocampal information flow. Neuron 79:1208-1221.

Bazelot M, Dinocourt C, Cohen I, Miles R (2010) Unitary inhibitory field potentials in the CA3 region of rat hippocampus. J Physiol 588:2077-2090.

Ben-Ari Y (2002) Excitatory actions of gaba during development: the nature of the nurture. Nat Rev Neurosci 3:728-739.

Ben-Ari Y, Khalilov I, Kahle KT, Cherubini E (2012) The GABA excitatory/inhibitory shift in brain maturation and neurological disorders. Neuroscientist 18:467-486.

Berger H (1929) Uber das elektrenkephalogramm des menschen. Arch. Psychiatr Nervenkr 87:527-570.

Bischofberger J, Engel D, Frotscher M, Jonas P (2006a) Timing and efficacy of transmitter release at mossy fiber synapses in the hippocampal network. Pflugers Arch 453:361-372.

Bischofberger J, Engel D, Li L, Geiger JR, Jonas P (2006b) Patch-clamp recording from mossy fiber terminals in hippocampal slices. Nat Protoc 1:2075-2081.

Bliss TV, Lomo T (1973) Long-lasting potentiation of synaptic transmission in the dentate area of the anaesthetized rabbit following stimulation of the perforant path. J Physiol 232:331-356.

Borst JG, Sakmann B (1996) Calcium influx and transmitter release in a fast CNS synapse. Nature 383:431-434.

Bragin A, Jandó G, Nádasdy Z, Hetke J, Wise K, Buzsáki G (1995) Gamma (40-100 Hz) oscillation in the hippocampus of the behaving rat. J Neurosci 15:47-60.

Bragin A, Benassi SK, Engel J Jr (2012) Patterns of the UP-Down state in normal and epileptic mice. Neuroscience 225:76-87.

Brody DL, Yue DT (2000) Release-independent short-term synaptic depression in cultured hippocampal neurons. J Neurosci 20:2480-2494.

Buckmaster PS, Jongen-Rêlo AL (1999) Highly specific neuron loss preserves lateral inhibitory circuits in the dentate gyrus of kainate-induced epileptic rats. J Neurosci 19:9519-9529.

Bucurenciu I, Kulik A, Schwaller B, Frotscher M, Jonas P (2008) Nanodomain coupling between Ca^{2+} channels and Ca^{2+} sensors promotes fast and efficient transmitter release at a cortical GABAergic synapse. Neuron 57:536-545.

Buhl EH, Han ZS, Lörinczi Z, Stezhka VV, Karnup SV, Somogyi P (1994) Physiological properties of anatomically identified axo-axonic cells in the rat hippocampus. J Neurophysiol 71:1289-1307.

Buzsáki G, Draguhn A (2004) Neuronal oscillations in cortical networks. Science 304:1926-1929.

Buzsáki G (2005) Theta rhythm of navigation: link between path integration and landmark navigation, episodic and semantic memory. Hippocampus 15:827-840.

Buzsáki G, Wang XJ (2012) Mechanisms of gamma oscillations. Annu Rev Neurosci 35:203-225.

Buzsáki G, Moser EI (2013) Memory, navigation and theta rhythm in the hippocampal-entorhinal system. Nat Neurosci 16:130-138.

Chiang PH, Wu PY, Kuo TW, Liu YC, Chan CF, Chien TC, Cheng JK, Huang YY, Chiu CD, Lien CC (2012) GABA is depolarizing in hippocampal dentate granule cells of the adolescent and adult rats. J Neurosci 32:62-67.

Chittajallu R, Pelkey KA, McBain CJ (2013) Neurogliaform cells dynamically regulate somatosensory integration via synapse-specific modulation. Nat Neurosci 16:13-15.

Chiu CQ, Lur G, Morse TM, Carnevale NT, Ellis-Davies GC, Higley MJ (2013) Compartmentalization of GABAergic inhibition by dendritic spines. Science 340:759-762.

Citri A, Malenka RC (2008) Synaptic plasticity: multiple forms, functions, and mechanisms. Neuropsychopharmacology 33:18-41.

Cobb SR, Buhl EH, Halasy K, Paulsen O, Somogyi P (1995) Synchronization of neuronal activity in hippocampus by individual GABAergic interneurons. Nature 378: 75-78.

Coetzee WA, Amarillo Y, Chiu J, Chow A, Lau D, McCormack T, Moreno H, Nadal MS, Ozaita A, Pountney D, Saganich M, Vega-Saenz de Miera E, Rudy B (1999) Molecular diversity of K^+ channels. Ann N Y Acad Sci 868:233-285.

Cutsuridis V, Cobb S, Graham BP (2010) Encoding and retrieval in a model of the hippocampal CA1 microcircuit. Hippocampus 20:423-446.

DeFelipe J, López-Cruz PL, Benavides-Piccione R, Bielza C, Larrañaga P, Anderson S, Burkhalter A, Cauli B, Fairén A, Feldmeyer D, Fishell G, Fitzpatrick D, Freund TF, González-Burgos G, Hestrin S, Hill S, Hof PR, Huang J, Jones EG, Kawaguchi Y, et al. (2013) New insights into the classification and nomenclature of cortical GABAergic interneurons. Nat Rev Neurosci 14:202-216.

Del Pino I, García-Frigola C, Dehorter N, Brotons-Mas JR, Alvarez-Salvado E, Martínez de Lagrán M, Ciceri G, Gabaldón MV, Moratal D, Dierssen M, Canals S, Marín O, Rico B (2013) Erbb4 deletion from fast-spiking interneurons causes schizophrenia-like phenotypes. Neuron 79:1152-1168.

Dudek SM, Bear MF (1992) Homosynaptic long-term depression in area CA1 of hippocampus and effects of N-methyl-D-aspartate receptor blockade. Proc Natl Acad Sci U S A 89:4363-4367.

Duque A, Gazula VR, Kaczmarek LK (2013) Expression of Kv1.3 potassium channels regulates density of cortical interneurons. Dev Neurobiol 73:841-855.

Ebihara S, Shirato K, Harata N, Akaike N (1995) Gramicidin-perforated patch recording: GABA response in mammalian neurones with intact intracellular chloride. J Physiol 484:77-86.

Eggermann E, Bucurenciu I, Goswami SP, Jonas P (2012) Nanodomain coupling between Ca^{2+} channels and sensors of exocytosis at fast mammalian synapses. Nat Rev Neurosci 13:7-21.

Elmqvist D, Quastel DM (1965) A quantitative study of end-plate potentials in isolated human muscle. J Physiol 178:505-529.

Epsztein J, Brecht M, Lee AK (2011) Intracellular determinants of hippocampal CA1 place and silent cell activity in a novel environment. Neuron 70:109-120.

Fioravante D, Regehr WG (2011) Short-term forms of presynaptic plasticity. Curr Opin Neurobiol 21:269-274.

Földy C, Lee SH, Morgan RJ, Soltesz I (2010) Regulation of fast-spiking basket cell synapses by the chloride channel ClC-2. Nat Neurosci 13:1047-1049.

Förster E, Zhao S, Frotscher M (2006) Laminating the hippocampus. Nat Rev Neurosci 7:259-267.

Freund TF, Ylinen A, Miettinen R, Pitkänen A, Lahtinen H, Baimbridge KG, Riekkinen PJ (1992) Brain Res Bull 28:27-38.

Freund TF , Buzsáki G (1996) Interneurons of the hippocampus. Hippocampus 6:347-470.

Fyhn M, Molden S, Witter MP, Moser EI, Moser MB (2004) Spatial representation in the entorhinal cortex. Science 305:1258-1264.

Geiger JR, Lübke J, Roth A, Frotscher M, Jonas P (1997) Submillisecond AMPA receptor-mediated signaling at a principal neuron-interneuron synapse. Neuron 18:1009-1023.

Geiger JR, Jonas P (2000) Dynamic control of presynaptic Ca^{2+} inflow by fast-inactivating K^+ channels in hippocampal mossy fiber boutons. Neuron 28:927-939.

Gerkin RC, Clem RL, Shruti S, Kass RE, Barth AL (2010) Cortical up state activity is enhanced after seizures: a quantitative analysis. J Clin Neurophysiol 27:425-432

Glickfeld LL, Scanziani M (2006) Distinct timing in the activity of cannabinoid-sensitive and cannabinoid-insensitive basket cells. Nat Neurosci 9:807-815.

Glickfeld LL, Roberts JD, Somogyi P, Scanziani M (2009) Interneurons hyperpolarize pyramidal cells along their entire somatodendritic axis. Nat Neurosci 12:21-23.

Goldberg EM, Clark BD, Zagha E, Nahmani M, Erisir A, Rudy B (2008) K^+ channels at the axon initial segment dampen near-threshold excitability of neocortical fast-spiking GABAergic interneurons. Neuron 58:387-400.

Hafting T, Fyhn M, Molden S, Moser MB, Moser EI (2005) Microstructure of a spatial map in the entorhinal cortex. Nature 436:801-806.

Haider B, Duque A, Hasenstaub AR, McCormick DA (2006) Neocortical network activity in vivo is generated through a dynamic balance of excitation and inhibition. J Neurosci 26:4535-4545.

Haider B, McCormick DA (2009) Rapid neocortical dynamics: cellular and network mechanism. Neuron 62:171-189.

Han ZS, Buhl EH, Lörinczi Z, Somogyi P (1993) A high degree of spatial selectivity in the axonal and dendritic domains of physiologically identified local-circuit neurons in the dentate gyrus of the rat hippocampus. Eur J Neurosci 5:395-410.

Harata N, Ryan TA, Smith SJ, Buchanan J, Tsien RW (2001) Visualizing recycling synaptic vesicles in hippocampal neurons by FM 1-43 photoconversion. Proc Natl Acad Sci U S A 98:12748-12753.

Hasenstaub A, Shu Y, Haider B, Kraushaar U, Duque A, McCormick DA (2005) Inhibitory postsynaptic potentials carry synchronized frequency information in active cortical networks. Neuron 47:423-435.

Hefft S, Jonas P (2005) Asynchronous GABA releases generates long-lasting inhibition at a hippocampal interneuron-principal neuron synapse. Nat Neurosci 8:1319-1328.

Herculano-Houzel S, Mota B, Lent R (2006) Cellular scaling rules for rodent brains. Proc Natl Acad Sci U S A 103:12138-12143.

Herculano-Houzel S (2009) The human brain in numbers: a linearly scaled-up primate brain. Front Hum Neurosci 3:31.

Hille B (2001) Ion Channels of Excitable Membranes 3rd edition. Sinauer Associates, Inc. Press.

Hodgkin AL, Huxley AF (1952) A quantitative description of membrane current and its application to conduction and excitation in nerve. J Physiol 117:500-544.

Howard A, Tamas G, Soltesz I (2005) Lighting the chandelier: new vistas for axo-axonic cells.

Trends Neurosci 28:310-316.

Hu H, Martina M, Jonas P (2010) Dendritic mechanisms underlying rapid synaptic activation of fast-spiking hippocampal interneurons. Science 327:52-58.

Ishikawa T, Kaneko M, Shin HS, Takahashi T (2005) Presynaptic N-type and P/Q-type Ca^{2+} channels mediating synaptic transmission at the calyx of Held of mice. J Physiol 568:199-209.

Ishizuka N (2001) Laminar organization of the pyramidal cell layer of the subiculum in the rat. J Comp Neurol 435:89-110.

Jonas P, Vyleta NO (2012) Loose coupling between Ca^{2+} channels and release sensors generated “conditional detonator” properties of hippocampal mossy fiber terminals. Program No. 334.19. 2012 Neuroscience Meeting Planner. Washington, DC: Society for Neuroscience, 2012. Online.

Kandel ER (2009) The biology of memory: a forty-year perspective. J Neurosci 29:12748-12756.

Katona I, Sperlágh B, Sík A, Käfalvi A, Vizi ES, Mackie K, Freund TF (1999) Presynaptically located CB1 cannabinoid receptors regulate GABA release from axon terminals of specific hippocampal interneurons. J Neurosci 19:4544-4558.

Kelleher RJ 3rd, Govindarajan A, Jung HY, Kang H, Tonegawa S (2004) Translational control by MAPK signaling in long-term synaptic plasticity and memory. Cell 116:467-479.

Klausberger T, Somogyi P (2008) Neuronal diversity and temporal dynamics: the unity of hippocampal circuit operations. Science 321: 53-57.

Kraushaar U, Jonas P (2000) Efficacy and stability of quantal GABA release at a hippocampal interneuron-principal neuron synapse. J Neurosci 20:5594-5607.

Krueppel R, Remy S, Beck H (2011) Dendritic integration in hippocampal dentate granule cells. Neuron 71:512-528.

Lange RP, Roos AD, Borst JG (2003) Two modes of vesicle recycling in the rat calyx of Held. J Neurosci 23:10164-10173.

Larimer P, Strowbridge BW (2008) Nonrandom local circuits in the dentate gyrus. J Neurosci 28:12212-12223.

Laurberg S, Sørensen KE (1981) Associational and commissural collaterals of neurons in the hippocampal formation (hilus fasciae dentatae and subfield CA3). Brain Res 212:287-300.

Leão RN, Mikulovic S, Leão KE, Munguba H, Gezelius H, Enjin A, Patra K, Eriksson A, Loew LM, Tort AB, Kullander K (2012) OLM interneurons differentially modulate CA3 and entorhinal inputs to hippocampal CA1 neurons. Nat Neurosci 15:1524-1530.

Leutgeb JK, Leutgeb S, Moser MB, Moser EI (2007) Pattern separation in the dentate gyrus and CA3 of the hippocampus. Science 315:961-966.

Li Y, Stam FJ, Aimone JB, Goulding M, Callaway EM, Gage FH (2013) Molecular layer perforant path-associated cells contribute to feed-forward inhibition in the adult dentate gyrus. Proc Natl Acad Sci U S A 110:9106-9111.

Liao CW, Lien CC (2009) Estimating intracellular Ca^{2+} concentrations and buffering in a dendritic inhibitory hippocampal interneuron. Neuroscience 164:1701-1711.

Lien CC, Mu Y, Vargas-Caballero M, Poo MM (2006) Visual stimuli-induced LTD of GABAergic synapses mediated by presynaptic NMDA receptors. Nat Neurosci 9:372-380.

Lien CC, Jonas P (2003) Kv3 potassium conductance is necessary and kinetically optimized for high-frequency action potential generation in hippocampal interneurons. J Neurosci 23:2058-2068.

Llinás R, Sugimori M, Simon SM (1982) Transmission by presynaptic spike-like depolarization in the squid giant synapse. Proc Natl Acad Sci U S A 79:2415-2419.

Lovett-Barron M, Turi GF, Kaifosh P, Lee PH, Bolze F, Sun XH, Nicoud JF, Zemelman BV, Sternson SM, Losonczy A (2012) Regulation of neuronal input transformations by tunable dendritic inhibition. Nat Neurosci 15:423-430.

Maccaferri G, Roberts JD, Szucs P, Cottingham CA, Somogyi P (2000) Cell surface domain specific postsynaptic currents evoked by identified GABAergic neurones in rat hippocampus in vitro. J Physiol 524:91-116.

Markram H, Toledo-Rodriguez M, Wang Y, Gupta A, Silberberg G, Wu C (2004) Interneurons of the neocortical inhibitory system. Nat Rev Neurosci 5:793-807.

Massi L, Lagler M, Hartwich K, Borhegyi Z, Somogyi P, Klausberger T (2012) Temporal dynamics of parvalbumin-expressing axo-axonic and basket cells in the rat medial prefrontal cortex in vivo. J Neurosci 32:16496-16502.

McHugh TJ, Jones MW, Quinn JJ, Balthasar N, Coppari R, Elmquist JK, Lowell BB, Fanselow MS, Wilson MA, Tonegawa S (2007) Dentate gyrus NMDA receptors mediate rapid pattern separation in the hippocampal network. Science 317:94-99.

Miles R, Tóth K, Gulyás AI, Hájos N, Freund TF (1996) Differences between somatic and dendritic inhibition in the hippocampus. Neuron 16: 815-823.

Miller RJ (1998) Presynaptic receptors. Annu Rev Pharmacol Toxicol 38:201-227.

Mitra A, Mitra SS, Tsien RW (2011) Heterogeneous reallocation of presynaptic efficacy in recurrent excitatory circuits adapting to inactivity. Nat Neurosci 15:250-257.

Montgomery SM, Betancur MI, Buzsáki G (2009) Behavior-dependent coordination of multiple theta dipoles in the hippocampus. J Neurosci 29:1381-1394.

Morris RG, Anderson E, Lynch GS, Baudry M (1986) Selective impairment of learning and blockade of long-term potentiation by an N-methyl-D-aspartate receptor antagonist, AP5. Nature 319:774-776.

Moser EI, Kropff E, Moser MB (2008) Place cells, grid cells, and the brain’s spatial representation system. Annu Rev Neurosci 31:69-89.

Mott DD, Dingledine R (2003) Interneuron Diversity series: Interneuron research--challenges and strategies. Trends Neurosci 26:484-488.

Moulder KL, Mennerick S (2005) Reluctant vesicles contribute to the total readily releasable pool in glutamatergic hippocampal neurons. J Neurosci 25:3842-3850.

Mulkey RM, Malenka RC (1992) Mechanisms underlying induction of homosynaptic long-term depression in area CA1 of the hippocampus. Neuron 9:967-975.

Myatt DR, Hadlington T, Ascoli GA, Nasuto SJ (2012) Neuromantic - from semi-manual to semi-automatic reconstruction of neuron morphology. Front Neuroinform 6:4.

Naber PA, Witter MP (1998) Subicular efferents are organized mostly as parallel projections: a double-labeling, retrograde-tracing study in the rat. J Comp Neurol 393:284-297.

Nakashiba T, Cushman JD, Pelkey KA, Renaudineau S, Buhl DL, McHugh TJ, Rodriguez Barrera V, Chittajallu R, Iwamoto KS, McBain CJ, Fanselow MS, Tonegawa S (2012) Young dentate granule cells mediate pattern separation, whereas old granule cells facilitate pattern completion. Cell 149:188-201.

O'Keefe J, Dostrovsky J (1971) The hippocampus as a spatial map. Preliminary evidence from unit activity in the freely-moving rat. Brain Res 34:171-175.

O'Keefe, J; Nadel L (1978). The Hippocampus as a Cognitive Map. Oxford University Press.

Oláh S, Füle M, Komlósi G, Varga C, Báldi R, Barzó P, Tamás G (2009) Regulation of cortical microcircuits by unitary GABA-mediated volume transmission. Nature 461:1278-1281.

Pernía-Andrade AJ, Jonas P (2014) Theta-Gamma-Modulated Synaptic Currents in Hippocampal Granule Cells In Vivo Define a Mechanism for Network Oscillations. Neuron 81:140-152.

Pouille F, Scanziani M (2001) Enforcement of temporal fidelity in pyramidal cells by somatic feed-forward inhibition. Science 293:1159-1163.

Pouille F, Scanziani M (2004) Routing of spike series by dynamic circuits in the hippocampus. Nature 429:717-723.

Pouille F, Marin-Burgin A, Adesnik H, Atallah BV, Scanziani M (2009) Input normalization by global feedforward inhibition expands cortical dynamic range. Nat Neurosci 12:1577-1585.

Poulet JF, Petersen CC (2008) Internal brain state regulates membrane potential synchrony in barrel cortex of behaving mice. Nature 454:881-885.

Ren JQ, Aika Y, Heizmann CW, Kosaka T (1992) Quantitative analysis of neurons and glial cells in the rat somatosensory cortex, with special reference to GABAergic neurons and parvalbumin-containing neurons. Exp Brain Res 92:1-14.

Richards DA, Guatimosim C, Betz WJ (2000) Two endocytic recycling routes selectively fill two vesicle pools in frog motor nerve terminals. Neuron 27:551-559.

Rizzoli SO, Betz WJ (2005) Synaptic vesicle pools Nat Rev Neurosci 6:57-69.

Rollenhagen A, Sätzler K, Rodríguez EP, Jonas P, Frotscher M, Lübke JH (2007) Structural determinants of transmission at large hippocampal mossy fiber synapses. J Neurosci 27:10434-10444.

Ruiz A, Campanac E, Scott RS, Rusakov DA, Kullmann DM (2010) Presynaptic $GABA_A$ receptors enhance transmission and LTP induction at hippocampal mossy fiber synapses. Nat Neurosci 13: 431-438.

Sakmann B, Stuart G (1995) Patch-pipette recordings from the soma, dendrites and axon of neurons in brain slices. In Single Channel Recording, Sakmann B and Neher E, New York Plenum Press, 199-211.

Schaffer K (1892) Beitrag zur Histologie der Ammonshorn formation. Arch mikroskop Anatomie 39:611–632.

Scharfman HE, Schwartzkroin PA (1989) Protection of dentate hilar cells from prolonged stimulation by intracellular calcium chelation. Science 246:257-260.

Schmidt-Hieber C, Jonas P, Bischofberger J (2007) Subthreshold dendritic signal processing and coincidence detection in dentate gyrus granule cells. J Neurosci 27:8430-8441.

Schneggenburger R, Meyer AC, Neher E (1999) Released fraction and total size of a pool of immediately available transmitter quanta at a calyx synapse. Neuron 23:399-409.

Scoville WB, Milner B (1957) Loss of recent memory after bilateral hippocampal lesions. J Neurol Neurosurg Psychiatry 20:11-21.

Shu Y, Hasenstaub A, McCormick DA (2003) Turning on and off recurrent balanced cortical activity. Nature 423:288-293.

Sloviter RS (1987) Decreased hippocampal inhibition and a selective loss of interneurons in experimental epilepsy. Science 235:73-76.

Sloviter RS (1989) Calcium-binding protein (calbindin-D28k) and parvalbumin immunocytochemistry: localization in the rat hippocampus with specific reference to the selective vulnerability of hippocampal neurons to seizure activity. J Comp Neurol 280:183-196.

Staley KJ, Mody I (1992) Shunting of excitatory input to dentate gyrus granule cells by a depolarizing GABAA receptor-mediated postsynaptic conductance. J Neurophysil 68:197-212.

Steriade M (2001) Impact of network activities on neuronal properties in corticothalamic systems. J Neurophysiol 86:1-39.

Stevens CF, Williams JH (2007) Discharge of the readily releasable pool with action potentials at hippocampal synapses. J Neurophysiol 98:3221-3229.

Szabadics J, Soltesz I (2009) Functional specificity of mossy fiber innervation of GABAergic cells in the hippocampus. J Neurosci 29:4239-4251.

Szirmai I, Buzsáki G, Kamondi A (2012) 120 years of hippocampal Schaffer collaterals. Hippocampus 22:1508-1516.

Thanawala MS, Regehr WG (2013) Presynaptic calcium influx controls neurotransmitter release in part by regulating the effective size of the readily releasable pool. J Neurosci 33:4625-4633.

Tsodyks MV, Markram H (1997) The neural code between neocortical pyramidal neurons depends on neurotransmitter release probability. Proc Natl Acad Sci U S A 94:719-723.

Tsou K, Mackie K, Sañudo-Peña MC, Walker JM (1999) Cannabinoid CB1 receptors are localized primarily on cholecystokinin-containing GABAergic interneurons in the rat hippocampal formation. Neuroscience 93:969-975.

Verheugen JA, Fricker D, Miles R (1999) Noninvasive measurements of the membrane potential and GABAergic action in hippocampal interneurons. J Neurosci 19:2546-2555.

Verret L, Mann EO, Hang GB, Barth AM, Cobos I, Ho K, Devidze N, Masliah E, Kreitzer AC, Mody I, Mucke L, Palop JJ (2012) Inhibitory interneuron deficit links altered network activity and cognitive dysfunction in Alzheimer model. Cell 149:708-721.

Viney TJ, Lasztoczi B, Katona L, Crump MG, Tukker JJ, Klausberger T, Somogyi P (2013) Network state-dependent inhibition of identified hippocampal CA3 axo-axonic cells in vivo. Nat

Neurosci 16:1802-1811.

Wittner L, Henze DA, Záborszky L, Buzsáki G (2007) Three-dimensional reconstruction of the axon arbor of a CA3 pyramidal cell recorded and filled in vivo. Brain Struct Funct 212:75-83.

Zucker RS, Regehr WS (2002) Short-term synaptic plasticity. Annu Rev Physiol 64:355-405.

FIGURES AND TABLE

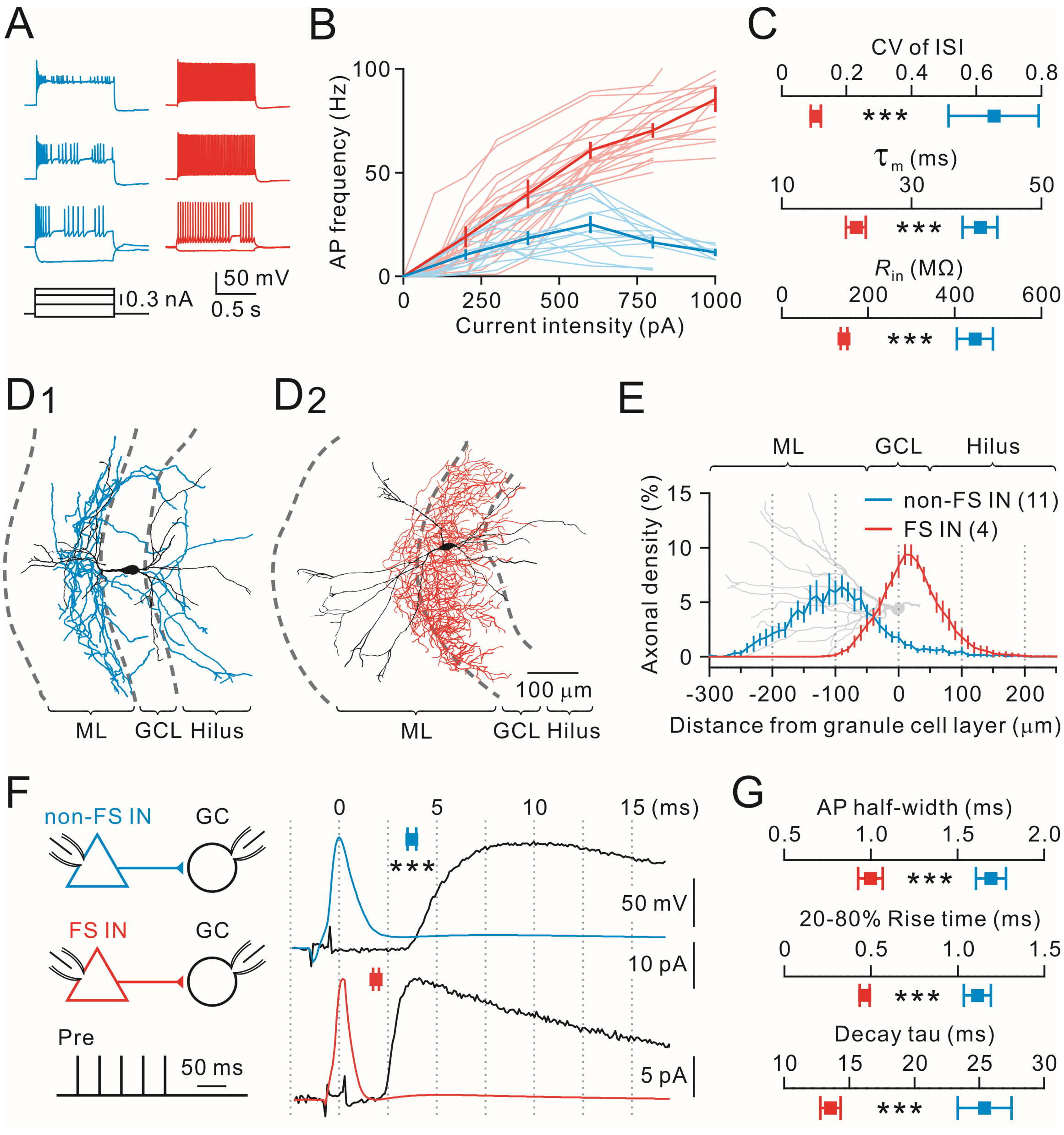

Fig. 1 Intrinsic, morphological, and synaptic properties of non-FS and FS cells

(A) Exemplar voltage responses evoked by a series of current pulses in a non-FS (blue) and a FS (red) cells. Current during the pulse was -0.1, +0.3, +0.6 and +0.8 nA. Membrane potential before the pulse was -70 mV.

(B) The relationship between the mean AP frequency and injected current for a subset of representative non-FS (n=14) and FS (n=16) cells. Individual cells were in lighter color and the average values were darker.

(C) Summary of CV of ISI, τ_m and R_{in} of non-FS (blue, n=15) and FS (red, n=15) cells. ***$P < 0.0005$.

(D) Exemplar reconstruction of a non-FS IN (D_1), which had the main axonal distribution (blue) outside the GCL and a FS IN (D_2), which had the major axonal distribution (red) within the GCL. Somata and dendrites are indicated in black. ML, molecular layer.

(E) Axonal density distribution for non-FS (n=11) and FS (n=4) INs plotted against distance from the GCL. A reconstructed GC (gray) is aligned and scaled to the plot for reference.

(F) Left, schematic of paired recordings from a non-FS IN (blue)-to-GC (black) pair and a FS IN (red)-to-GC pair. Bursts of five APs were evoked in the non-FS IN and the FS IN by injection of brief current pulses (1 ms, 25 Hz) every 5 s. Presynaptic INs were current clamped at -70 mV, while postsynaptic GCs were voltage clamped at -80 mV. Right, the first AP from non-FS (blue) and FS (red) INs and their corresponding average uIPSCs (average of 70 and 73 sweeps, respectively, currents were inverted for clarity) in the target GCs (black) on an expanded time scale (vertical lines are separated by 2.5 ms). Squares, average uIPSC latencies for non-FS (n=11) and FS cells (n=10). ***$P < 0.0005$.

(G) Summary of AP half-width (blue, n=8; red, n=10), 20-80% rise time (blue, n=10; red, n=12) and decay time constant (blue, n=9; red, n=12). ***$P < 0.0005$.

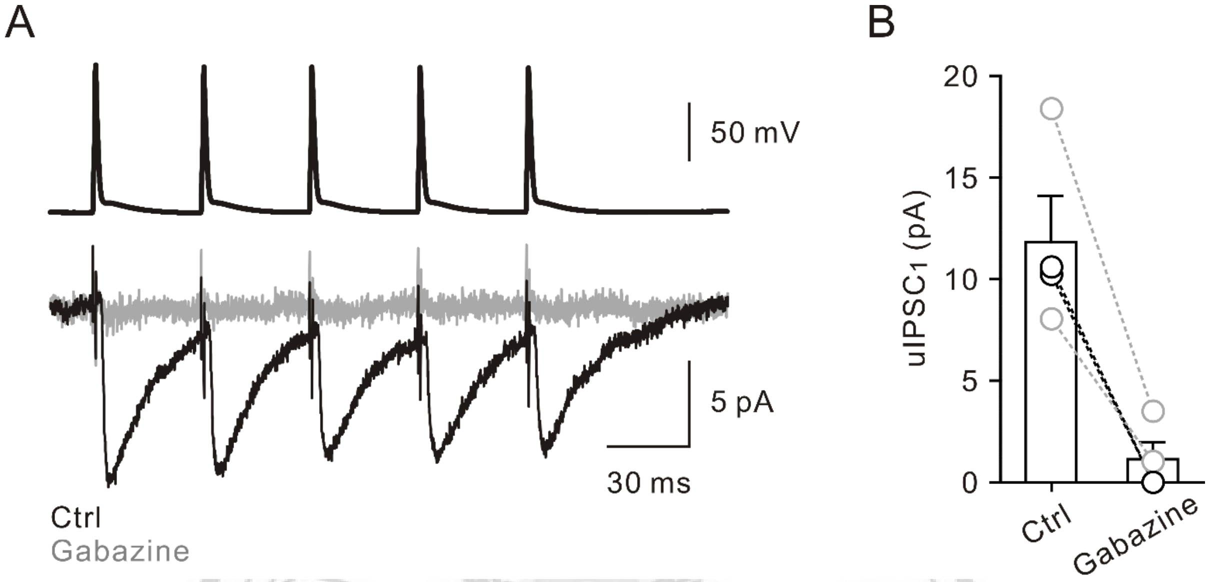

Fig. 2 Unitary GABAergic transmission

(A) Representative traces of non-FS IN-to-GC paired recoding. Top, five action potentials (25 Hz) evoked in a presynaptic IN; bottom, average uIPSCs recorded from a postsynaptic GC in the control (black) and presence (gray) of gabazine (1 µM). Traces were average of 25-65 sweeps.

(B) Summary of effect of gabazine, the mean amplitude of $uIPSC_1$ were reduced to less than 10% of control (black, non-FS IN-to-GC, n=2; gray, FS IN-to-GC, n=2).

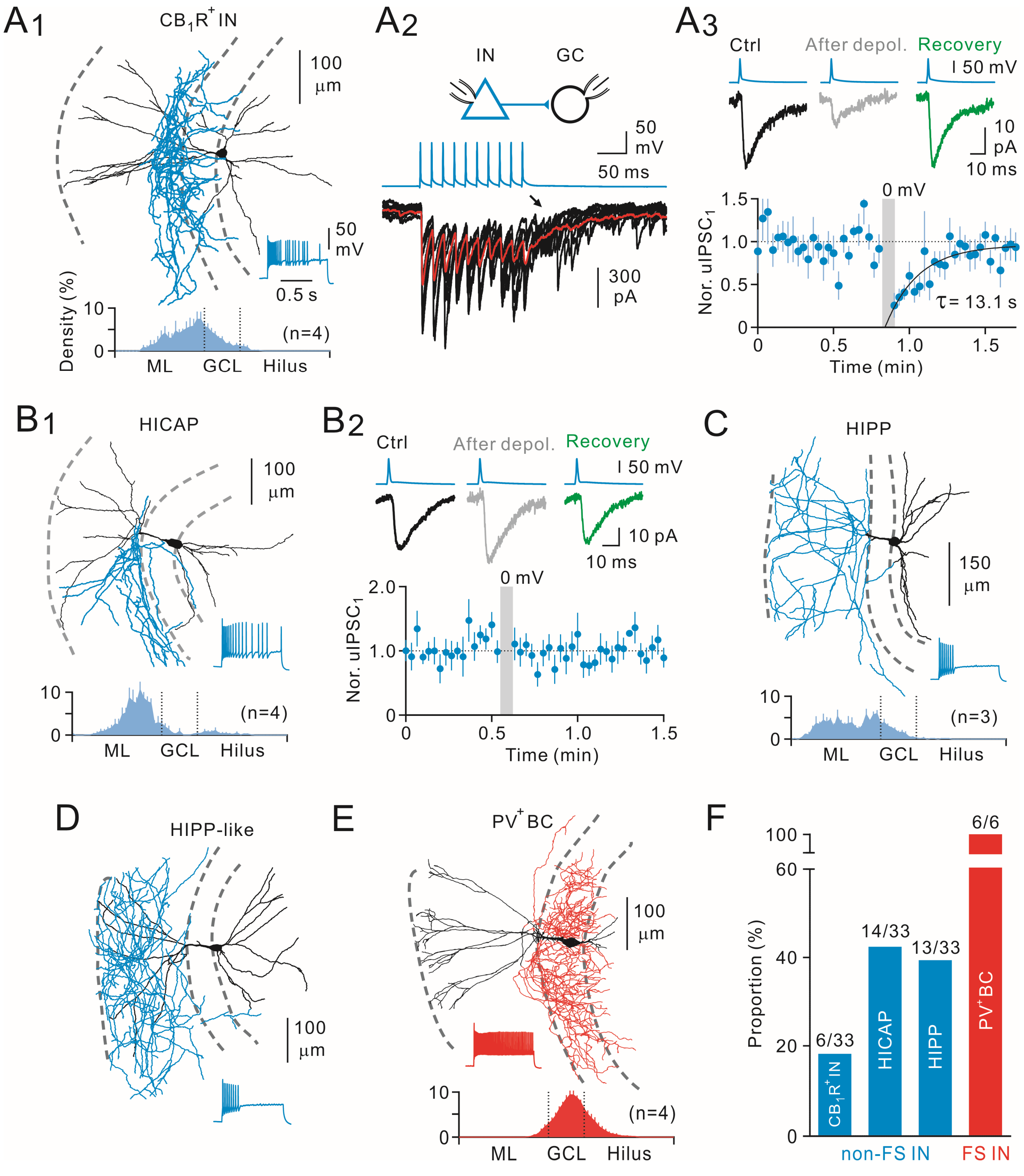

Fig. 3 Heterogeneity of non-FS INs

(A) A non-FS cell (A_1), a putative CB_1R^+IN, with the axonal distribution within the IML (bottom, density plot) exhibited asynchronous release onto GCs (A_2, arrow) and depolarization-induced suppression of inhibition (DSI) (A_3). To induce DSI, GCs were depolarized to 0 mV for 5 s. Eight single uIPSC sweeps are superimposed in A_2; red curve is the average of 35 sweeps; A_3, top, uIPSC traces in control, after depolarization, and recovery from DSI; uIPSC traces are average of 8-25 sweeps. Bottom, summary of the time course of uIPSC suppression from putative CB_1R^+ IN-to-GC pairs (n=5). Recovery is fitted with a single exponential function. CB_1R^+, cannabinoid receptor type 1 (+).

(B) A non-FS cell, a putative hilar C/A pathway-related (HICAP) cell (B_1), had the main axonal innervation in the IML. B_2, HICAP cells had no DSI response (average of 10 pairs). Note that the dendritic processes penetrated the GCL and radially ascended into the ML, whereas the remaining dendrites ramified in the hilus. Bottom, axonal density plot.

(C) A non-FS cell, a typical hilar PP-associated (HIPP) cell, had the axonal distribution in the PP terminal field. Note the dendrites strictly in the hilus. Bottom, axonal density plot.

(D) An exemplar atypical HIPP-like cell, which had the axonal distribution of HIPP cells, but the dendrites ramified in the ML, in addition to the hilus.

(E) A FS cell, a putative PV^+BC with the axonal distribution within the GCL. Note the tangential axon collaterals in the hilus and scattered boutons all along. Bottom, axonal density plot.

(F) Summary of morphological classification of non-FS and FS INs.

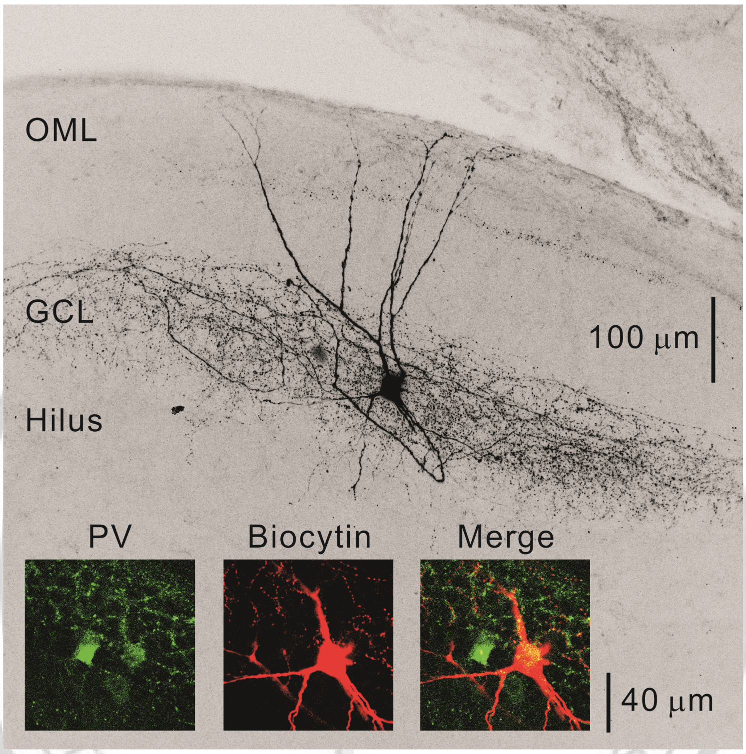

Fig. 4 PV immunoreactivity of a BC in the DG

Morphological reconstruction of a DG BC. Insets, immunoreactivity of PV and biocytin. Note that the PV signals were relatively weaker in the recorded cell than the not recorded one. OML, outer molecular layer.

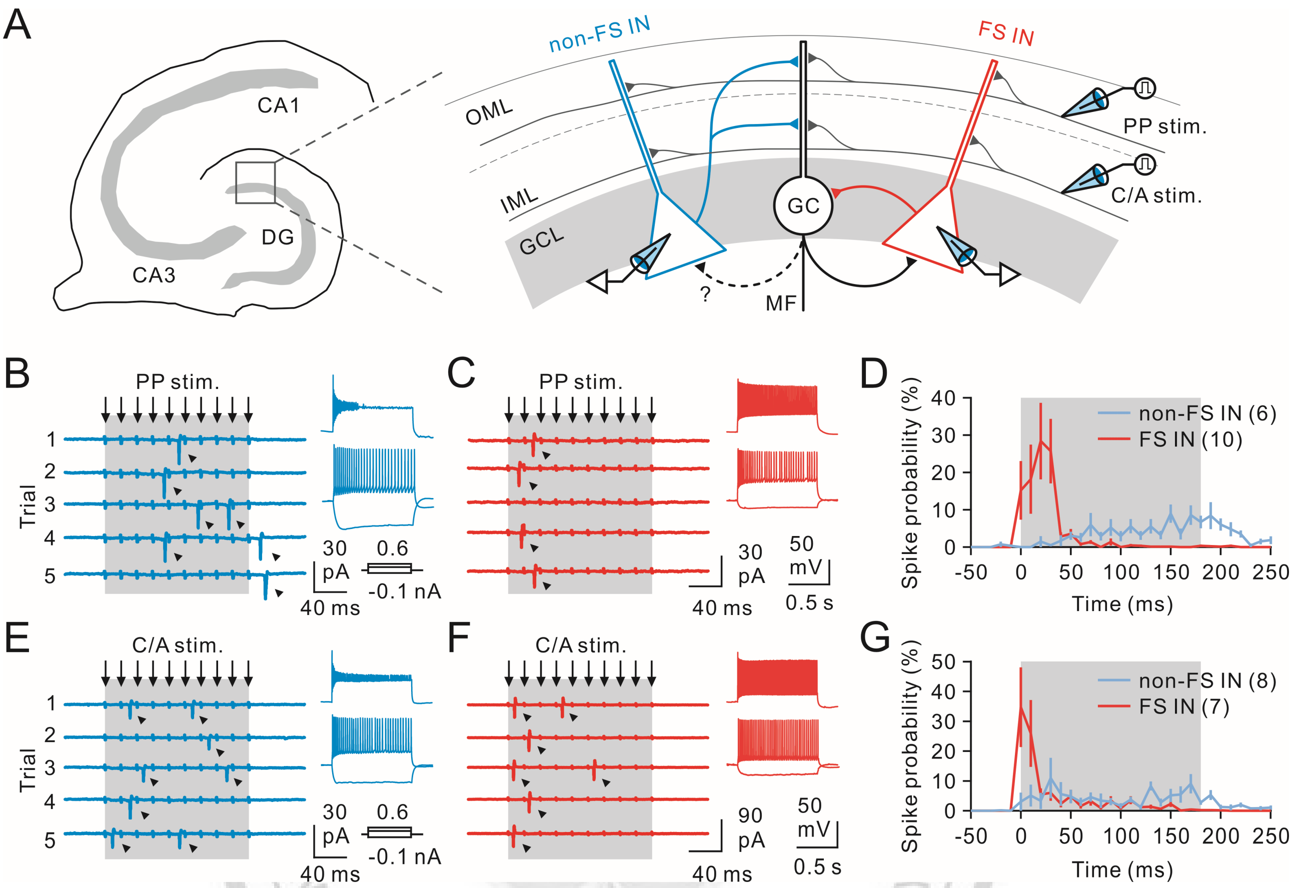

Fig. 5 Differential recruitment of two IN classes by excitatory afferents

(A) Schematic diagram showing extracellular stimulation of afferents (PP stim. and C/A stim.) and FS-IN and non-FS IN recording configuration (not simultaneous). Black circle, GC; blue triangle, dendrite-targeting IN; red triangle, soma-targeting IN; PP, perforant path; C/A, commissural/associational; MF, mossy fiber; OML, outer molecular layer; IML, inner molecular layer. Note the reciprocal connections between soma-targeting INs and GCs.

(B) Exemplar cell-attached recording of responses (arrow heads) to PP stimuli (50 Hz trains (arrows) delivered at near-threshold intensities) in a 'late-onset' IN. The stimulation electrode was positioned within the OML to activate the PP pathway. Inset, whole-cell current-clamp recording of the same cell displayed adapting, non-FS patterns in response to positive square pulse of currents. In the following figures, the spiking pattern allowing identification of the neurons as non-FS or FS cells is shown as an inset

(C) Same stimulation as in (B) triggered responses in an 'early-onset' IN, which responded at the early phase of stimulations. Inset, the same cell displayed non-adapting, FS patterns upon depolarization.

(D) Histogram showing spike probability of non-FS and FS cells in response to ten PP stimulations. Each data point is a 10-ms bin with spike number normalized to the total spike number during stimulation.

(E) Cell-attached recording of spike responses from a 'late-onset' IN to ten stimulations of the C/A pathways. Inset, the same cell displayed adapting, non-FS patterns upon depolarization.

(F) Same stimulation as in (E) triggered spike responses of an 'early-onset' IN. Inset, the same cell displayed non-adapting, FS patterns upon depolarization.

(G) Histogram showing spike probability of non-FS and FS cells in response to C/A afferents stimulation (bin width, 10 ms).

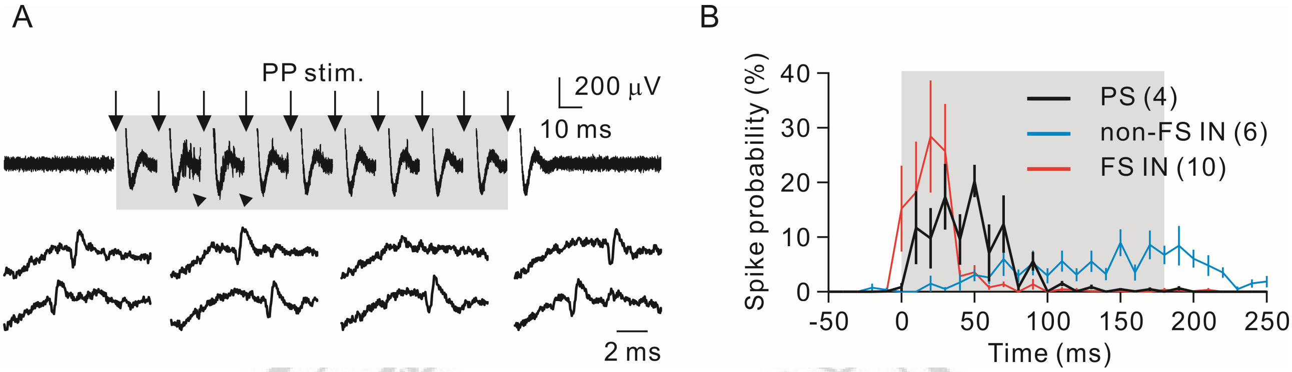

Fig. 6 Intermediate pattern of (GC) population spike in response to PP stimulation

(A) Top, exemplar extracellular recording of responses (arrowheads) to PP stimuli (50 Hz trains; arrows) in the GCL. Ten single sweeps were superimposed. Bottom, temporal enlargement of individual population spikes. Artifacts were blanked for clarity.

(B) Histogram showing spike probability of population spike (PS), non-FS and FS cells in response to ten PP stimulations. Each data point is a 10-ms bin with spike number normalized to the total spike number during stimulation. Note that PS recorded in the GCL displayed an intermediate pattern between non-FS IN and FS IN.

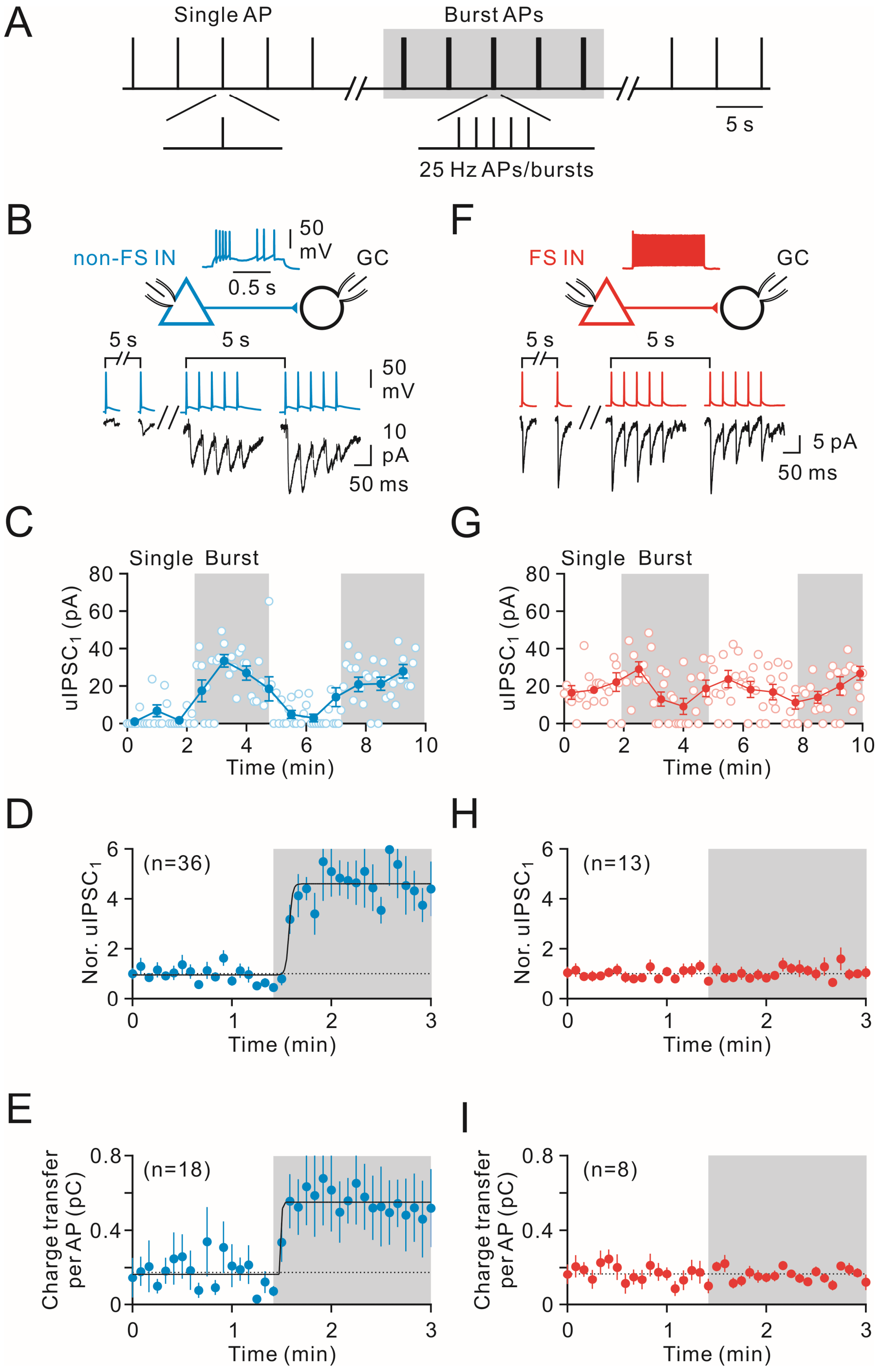

Fig. 7 Cell type-specific dynamics of GABA release

(A) Stimulation protocol used to trigger presynaptic spikes in paired recordings between presynaptic INs and postsynaptic GCs. A single AP ('Single'-mode) or a 25-Hz burst of five presynaptic APs ('Burst'-mode) evoked by brief current pulses were applied at a repetition frequency of 0.2 Hz.

(B) Paired recording between a presynaptic non-FS IN (blue) and a postsynaptic GC (black). Presynaptic IN was evoked by stimulation protocol shown in (A) and the corresponding uIPSCs (bottom traces; single sweeps).

(C) Plot of the peak amplitude of the uIPSC$_1$ evoked by single APs and the uIPSC$_1$ evoked by 25-Hz burst of five APs against time; the same cell as shown in (B). Open circle, individual uIPSC$_1$. Filled circle, average uIPSC$_1$ (average of 9 events).

(D) Summary of uIPSC$_1$ from non-FS IN-to-GC pairs. Curves in (D) and (E) show Boltzmann functions fitted to the data points. Note a brief delay (about 10 s) before the switch of synaptic strength.

(E) Summary of average charge transfer per AP from non-FS IN-to-GC pairs.

(F) Similar to (B), paired recording from a FS IN (red)-to-GC (black) pair. Presynaptic APs (top traces) and corresponding uIPSCs (bottom traces; single sweeps).

(G) Plot of peak amplitude of uIPSC$_1$ against time; the same cell as shown in (F). Open circle, individual uIPSC$_1$. Filled circle, average uIPSC$_1$ (average of 9 events).

(H) Summary of uIPSC$_1$ from FS IN-to-GC pairs.

(I) Summary of average charge transfer per AP from FS IN-to-GC pairs.

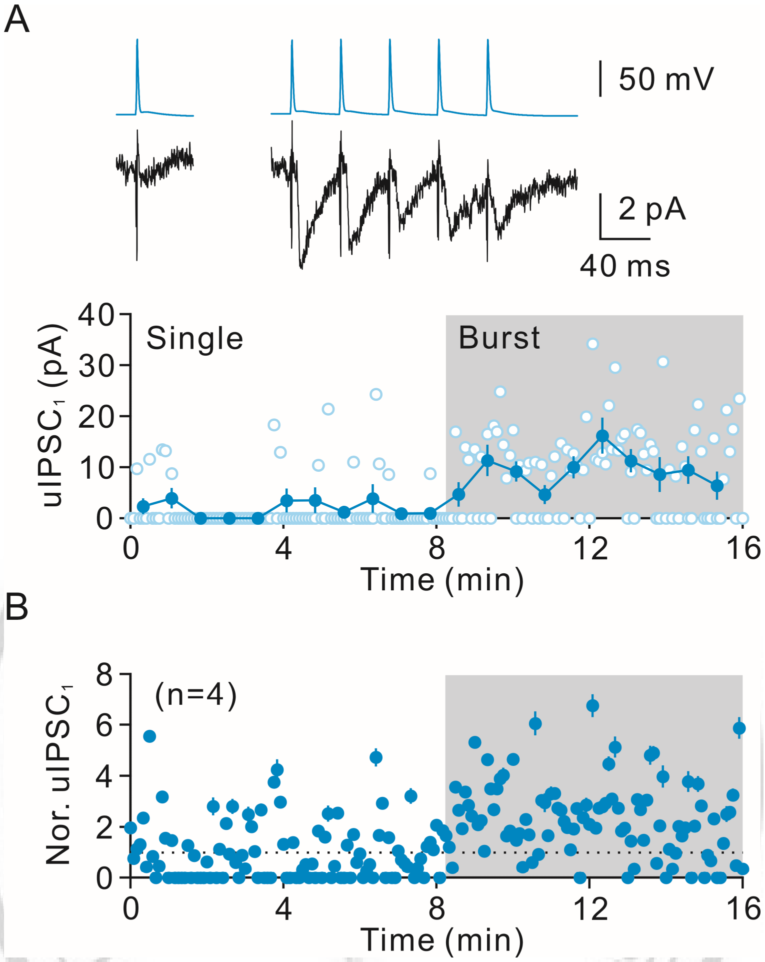

Fig. 8 Stable synaptic transmission during periods of single and burst spiking can be obtained at 0.2 Hz

(A) Top, traces of presynaptic AP and postsynaptic responses; bottom, amplitudes of the uIPSC (single AP) and the uIPSC$_1$ (burst AP) were plotted versus time when a single AP or a 25-Hz burst of five APs was repetitively applied every 5 s. Recording was obtained from a non-FS IN-to-GC pair. Traces were average of 30 sweeps.

(B) Summary plot of four non-FS IN-to-GC pairs.

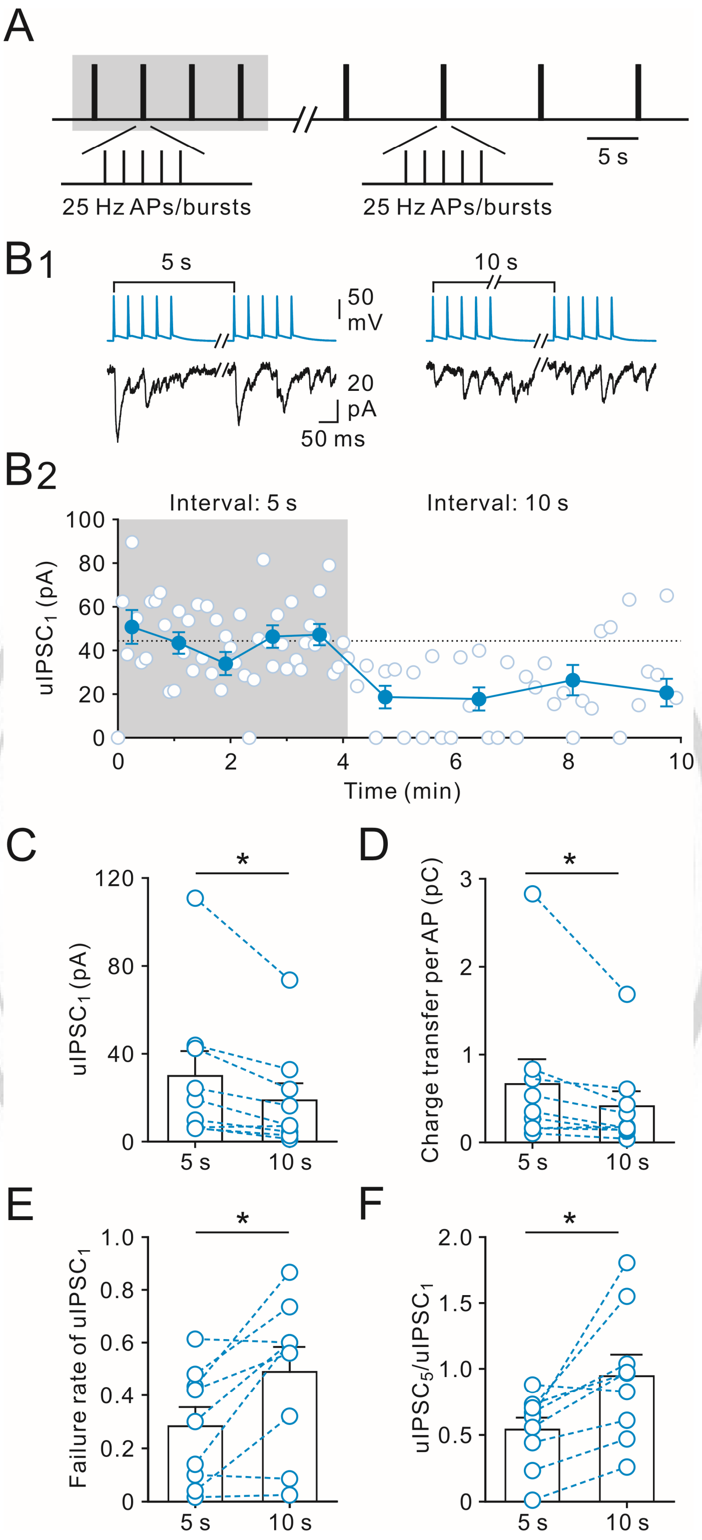

Fig. 9 Presynaptic activity-dependent fast dynamic switches of GABA release

(A) Stimulation protocol: 25-Hz bursts of presynaptic five APs were evoked repetitively at 5- or 10-s intervals.

(B) B_1, presynaptic APs (top) and postsynaptic uIPSCs (bottom, single sweeps). B_2, the peak amplitude of uIPSC$_1$ is plotted against time. Note that the peak amplitude of uIPSC$_1$ was rapidly decreased after the transition.

(C) Summary of uIPSC$_1$ amplitude at 5- and 10-s intervals. *$P < 0.05$.

(D) Summary of mean integral of uIPSC per AP at 5- and 10-s intervals. *$P < 0.05$.

(E) Summary of failure rate at 5- and 10-s intervals. *$P < 0.05$.

(F) Summary of multiple-pulse ratio (uIPSC$_5$/uIPSC$_1$). Bars represent mean values, circles connected by dashed lines indicate data from the same experiment. *$P < 0.05$.

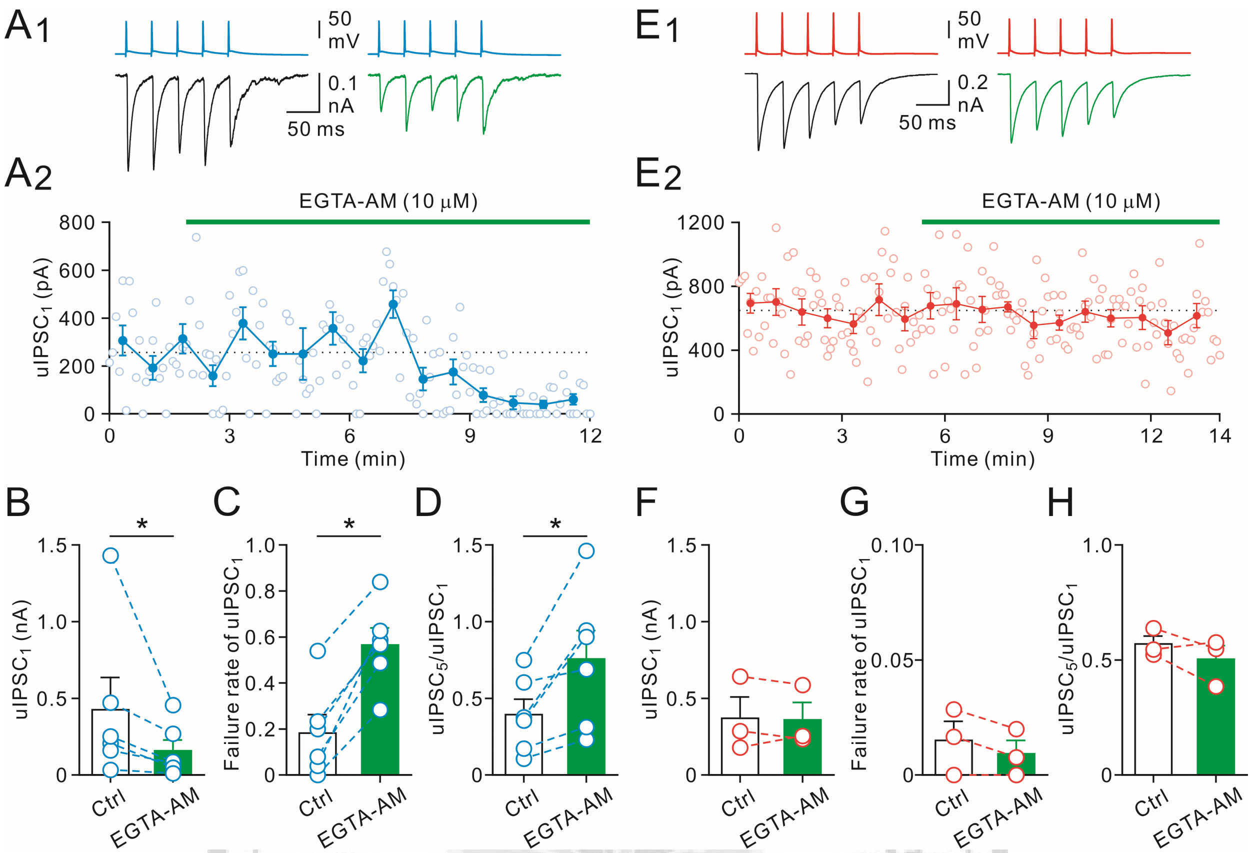

Fig. 10 Membrane-permeable Ca^{2+} chelator EGTA-AM decreased GABA release in non-FS INs

(A) A$_1$, 25-Hz bursts of five presynaptic APs and postsynaptic uIPSC traces (average of 25 sweeps); A$_2$, plot of their corresponding uIPSC$_1$ amplitude in control and after bath perfusion of EGTA-AM (10 μM). Horizontal bar indicates time of EGTA-AM application. Note that EGTA-AM also altered synaptic dynamics.

(B) Summary of mean uIPSC$_1$ amplitude before and after addition of EGTA-AM. *$P < 0.05$.

(C) Failure rate of uIPSC$_1$ before and after addition of EGTA-AM. *$P < 0.05$.

(D) Multiple-pulse ratio before and after addition of EGTA-AM. *$P < 0.05$.

(E) E_1, simultaneous recordings of presynaptic APs evoked in a FS IN (top) and the uIPSCs in a GC (bottom, average of 40 sweeps for each); E_2, plot of their corresponding uIPSC$_1$ amplitude in control and after bath perfusion of EGTA-AM.

(F) Summary of mean uIPSC$_1$ amplitude before and after addition of EGTA-AM.

(G) Failure rate of uIPSC$_1$ before and after addition of EGTA-AM.

(H) Multiple-pulse ratio before and after addition of EGTA-AM.

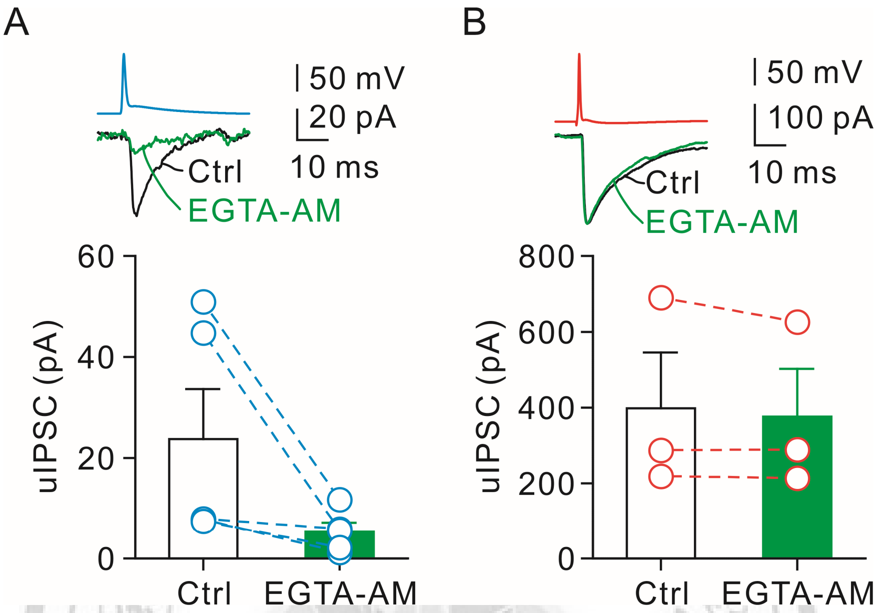

Fig. 11 Membrane-permeable Ca^{2+} chelator EGTA-AM selectively decreased GABA release of non-FS IN output synapses

(A) Top, traces of presynaptic AP and postsynaptic response before and after addition of EGTA-AM; single APs were repetitively applied every 5 s. Recording was obtained from a non-FS IN-to-GC pair. Bottom, summary of uIPSC amplitudes obtained from 5 non-FS IN-to-GC pairs. Traces were average of 26-40 sweeps.

(B) Top, traces of presynaptic AP and postsynaptic responses before and after addition of EGTA-AM; the same protocol as in (A). Recording was obtained from a FS IN-to-GC pair. Bottom, summary of uIPSC amplitudes. Traces were average of 40 sweeps.

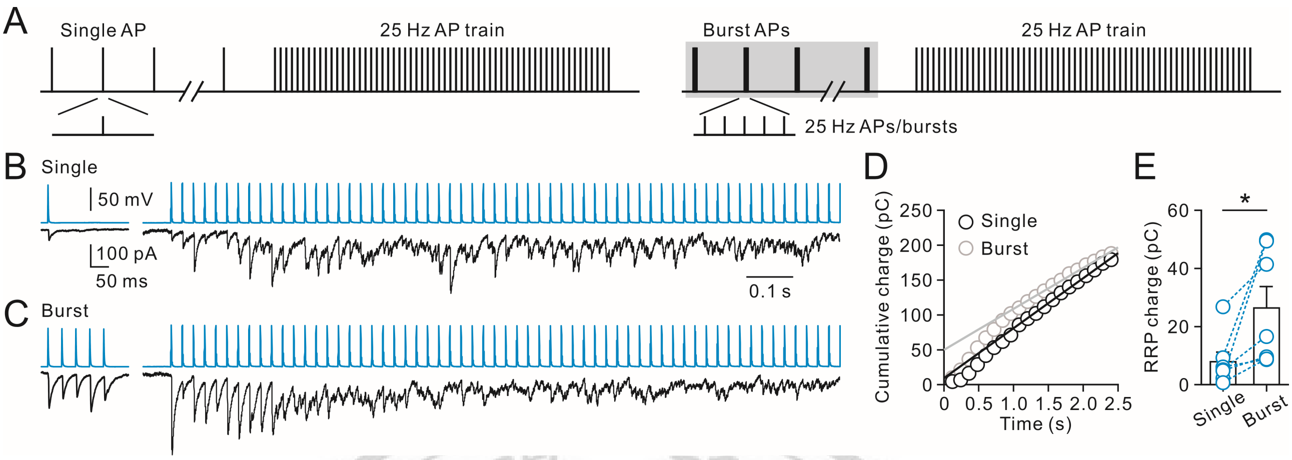

Fig. 12 The RRP size increased during the burst stimulation

(A) Protocols showing that AP trains (60 stimuli; 25 Hz) were delivered after single (left) and burst (right) stimulations to deplete the RRP.

(B) Representative single AP-induced uIPSC (average of 20 traces) and IPSC train (average of 2 trials) recorded from a non-FS IN-to-GC pair. Note synaptic currents during AP trains showing synchronous and asynchronous release.

(C) Representative burst AP-induced uIPSC (average of 30 traces) and IPSC train (average of 3 trials) recorded from the same pair as in (B).

(D) Representative cumulative IPSC area values versus time from the same 60 stimuli, 25 Hz train. Each data point is a 120-ms bin with cumulative charge. Each data point for single and burst firing is an average of 2 and 3 trials, respectively. The solid lines represent linear regression fits to data points after 1 s to estimate the cumulative area at time 0.

(E) Summary of total RRP charge (cumulative area at time 0), as determined with trains. Circles connected by dashed lines indicate data from the same cell. *$P < 0.05$.

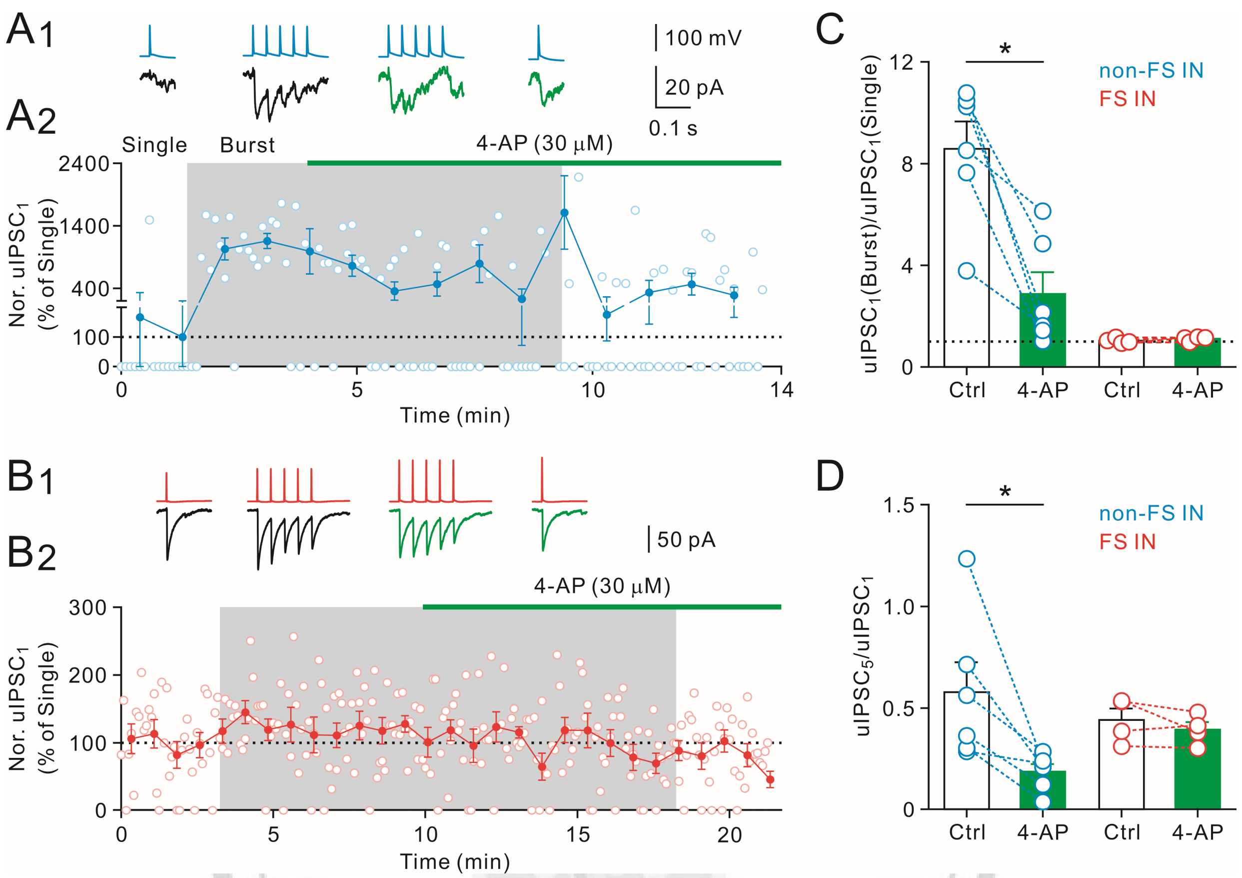

Fig. 13 Blockade of K$^+$ channels decreased the extent of the dynamic switch of dendritic inhibition

(A) A$_1$, bursts of presynaptic APs ('Burst'-mode, 25 Hz) and single presynaptic APs ('Single'-mode) were repetitively evoked at 0.2 Hz in a non-FS cell; postsynaptic uIPSC traces were average of 25-30 sweeps; A$_2$, plot of their mean uIPSC$_1$ amplitude (normalized to the 'Single'-mode in control) in control and in the presence of 4-AP (30 µM). Horizontal bar indicates time of 4-AP application. Note that 4-AP greatly increased uIPSCs during the 'single'-mode.

(B) B$_1$, bursts of presynaptic APs ('Burst'-mode, 25 Hz) and single presynaptic APs ('Single'-mode) were repetitively evoked at 0.2 Hz in a FS cell; postsynaptic uIPSC traces were average of 30 sweeps; B_2, plot of their normalized mean $uIPSC_1$ amplitude in control and in the presence of 4-AP (30 μM). Horizontal bar indicates time of 4-AP application.

(C) Ratio of mean $uIPSC_1$ amplitude in the ‘Burst’-mode over mean $uIPSC_1$ amplitude in the ‘Single’-mode in control and in the presence of 4-AP (30 μM). $*P < 0.05$.

(D) Multiple-pulse ratio in control and in the presence of 4-AP. $*P < 0.05$.

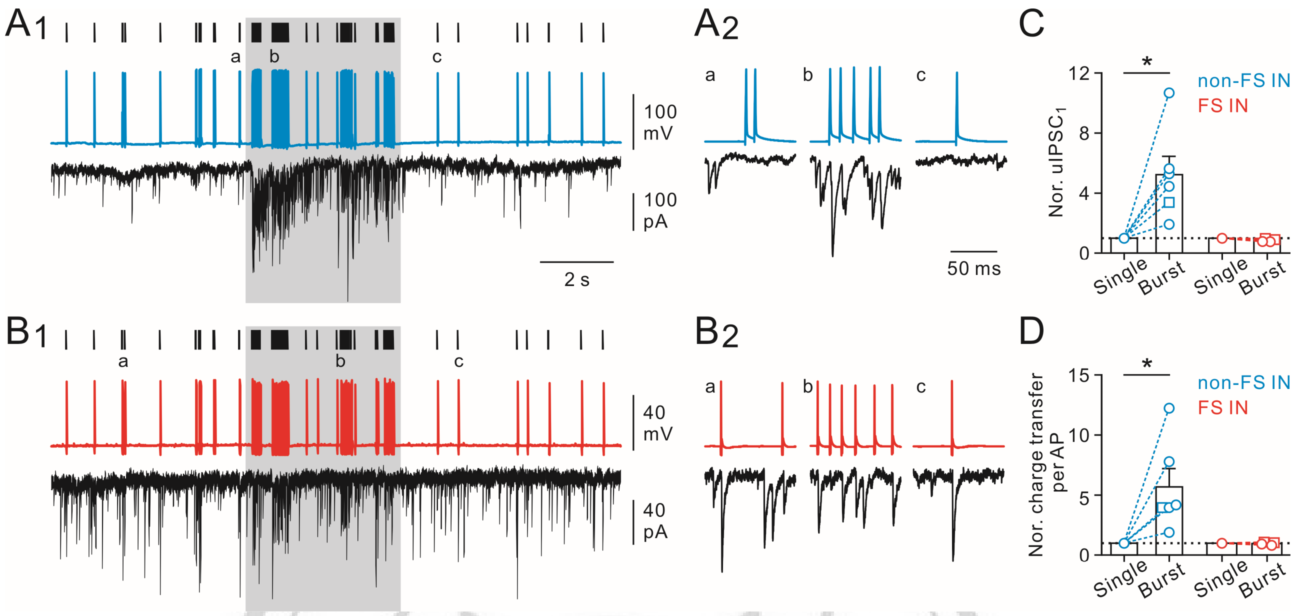

Fig. 14 Rapid dynamic changes of dendritic inhibition preserved at near-physiological temperature

(A) A_1, Top, spike train (shown with hash marks, adapted from Massi et al., 2012) as the stimulation protocol; middle trace, evoked spikes in a dendrite-targeting IN; bottom trace, uIPSCs recorded from a postsynaptic GC (single sweep). A_2, enlargement of spikes and uIPSCs as indicated in A_1.

(B) B_1, Top, the same stimulation protocol as in A_1; middle trace, discharge pattern of a soma-targeting IN; bottom trace, uIPSCs recorded from a postsynaptic GC (single sweep). B_2, enlargement of spikes and uIPSCs as indicated in B_1.

(C) Summary of mean uIPSC$_1$ (normalized to the ‘Single’ mode) from the ‘Single’- and ‘Burst’-modes. *$P < 0.05$.

(D) Summary of normalized mean charge transfer per AP from the ‘Single’- and ‘Burst’-modes. Circle, at 35 ˚C (n=7); square, at 23 ˚C (n=3). *$P < 0.05$.

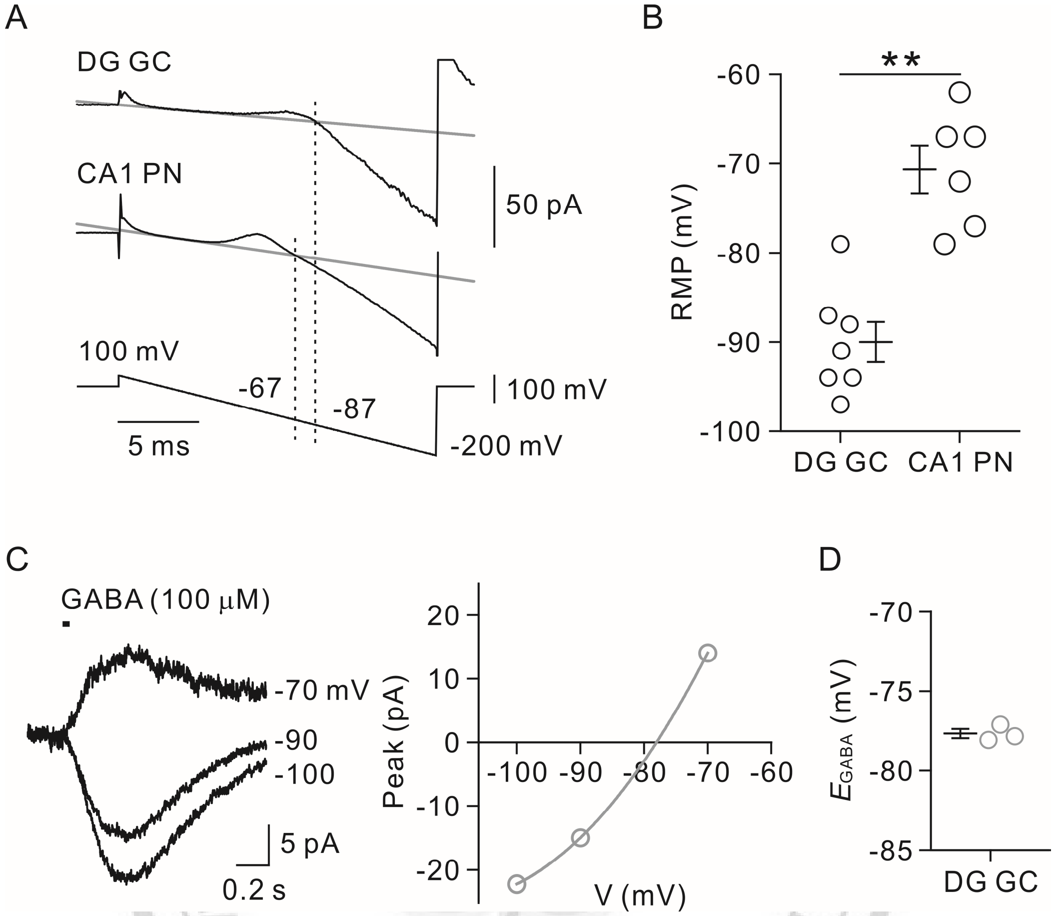

Fig. 15 Determine the action of GABA in the DG by noninvasive approaches

(A) The K$^+$ currents recorded from a DG GC (top) and a CA1 pyramidal neuron (PN, middle) elicited by a voltage ramp protocol (command voltage from 100 to -200 mV, bottom). The leak currents were fitted with a linear line (gray). Note that the K$^+$ currents reversed the polarity on the linear leak at relatively hyperpolarized command potential which represented the RMP and indicated by dashed line. Traces were average of 40-140 sweeps. Artifacts were blanked for clarity.

(B) Summary of estimated RMP in the DG GCs (n=7) and CA1 PNs (n=6). **$P < 0.005$.

(C) Left, GABAergic currents were elicited by local puffs of GABA (100 μM) and recorded from a GC by perforated-patch. Different holding voltages (-70 to -100 mV) revealed the reversed polarity of GABAergic currents. Traces were average of 5-14 sweeps. Black bar indicated the time of puffing. Right, current-voltage relations of the same GC. Data points were fitted with a second order polynomial function (gray line) to determine the E_{GABA} (-78.1 mV).

(D) Summary of estimated E_{GABA} of GCs (n=3).

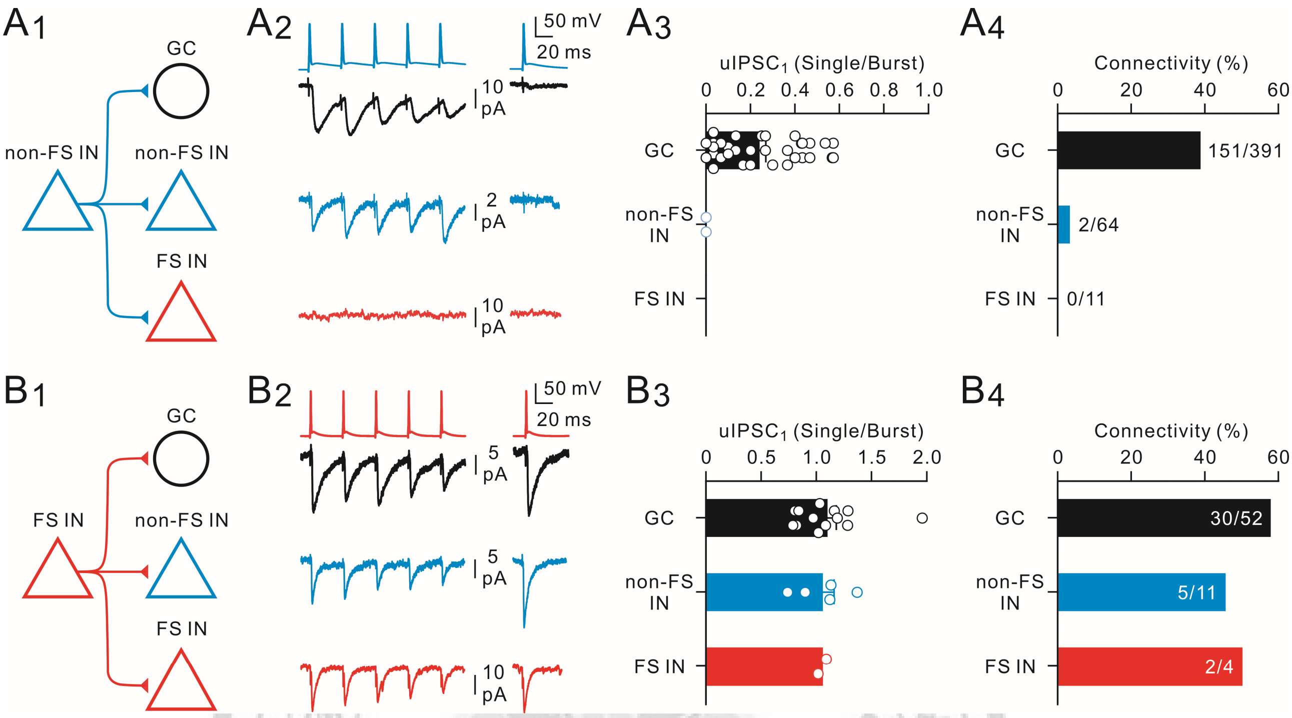

Fig. 16 Connectivity and specificity of the synaptic dynamic switch

(A) A_1, schematic of non-FS IN (blue triangle) to GC (black circle), non-FS IN (blue triangle), and FS IN (red triangle) connections; A_2, representative AP trace (top) from a non-FS IN and average uIPSC traces (bottom) recorded from a GC, a non-FS IN, and a FS IN. Note that no functional connection was detected at non-FS IN-to-FS IN synapses. A_3, Summary of the fraction of uIPSC$_1$(Single)/uIPSC$_1$(Burst) from non-FS IN-to-GC, non-FS IN-to-non-FS IN, and non-FS IN-to-FS IN connections, respectively. A_4, summary plot of the frequency of possible non-FS IN-to-GC, non-FS IN-to-non-FS IN, and non-FS IN-to-FS IN connections. There were 151 of 391 possible non-FS IN-to-GC, 2 of 64 possible non-FS IN-to-non-FS IN, and 0 of 11 possible non-FS IN-to-FS IN connections.

(B) B_1, schematic of FS IN to GC, non-FS IN, and FS IN connections; B_2, AP trace (top) from a FS IN and average uIPSC traces (bottom) recorded from a GC, a non-FS IN and a FS IN.

Current traces are average of 20-80 sweeps. B_3, summary of the fraction of uIPSC_1(Single)/uIPSC_1(Burst) from FS IN-to-GC, FS IN-to-non-FS IN, and FS IN-to-FS IN connections, respectively. B_4, summary plot of the frequency of possible connections. There were 30 of 52 possible FS IN-to-GC, 5 of 11 possible FS IN-to-non-FS IN, and 2 of 4 possible FS IN-to-FS IN connections.

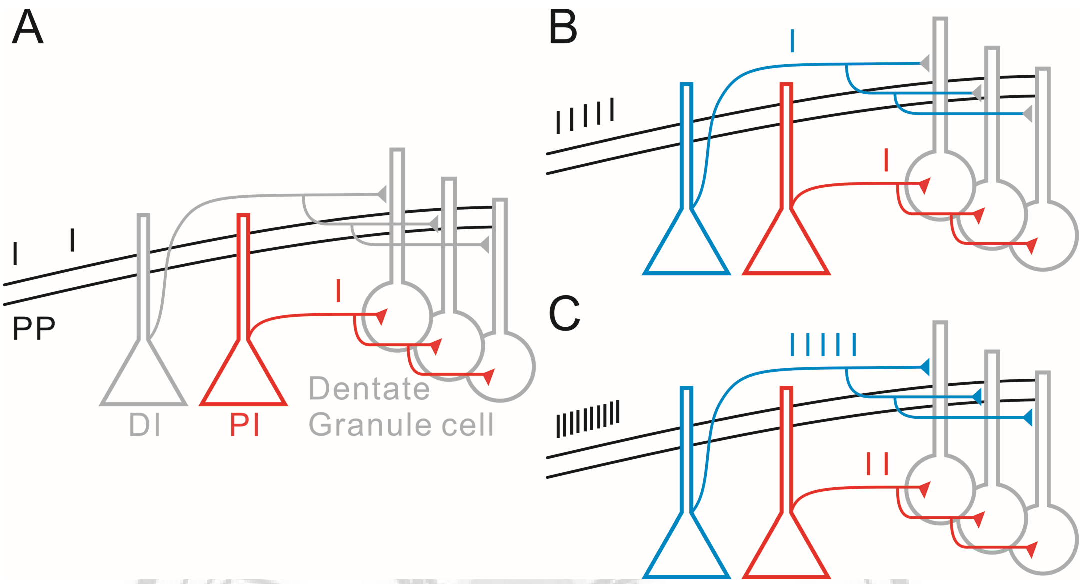

Fig. 17 Schematic summary of activity-dependent switch of dendritic inhibition in the DG.

(A) During resting state, sparse cortical inputs (black harsh marks) can only activate the perisomatic-targeting IN (PI) but not the dendrite-targeting IN (DI). Note that single spike in the PI (red harsh mark) is sufficient to release somatic GABA.

(B) In moderate activity state, elevated inputs can both recruit the DI and PI. Note that single spike in the DI (blue harsh mark) is not sufficient to release dendritic GABA.

(C) Intense inputs can give rise to effectively dendritic GABA release. Dendritic inhibition can be augmented more than four folds, whereas somatic inhibition remains relatively stable.

Table 1. Intrinsic and functional properties of IN-to-GC connections

	CB$_1$R$^+$IN→GC	HICAP→GC	HIPP→GC	PV$^+$BC→GC
AP half-width (ms)	1.7 ± 0.1	1.7 ± 0.1	1.9 ± 0.2	1.2 ± 0.1
CV of ISI	0.75 ± 0.20	0.80 ± 0.26	0.54 ± 0.32	0.09 ± 0.01
R_{in} (MΩ)	303 ± 13	343 ± 18	295 ± 48	109 ± 20
τ_m (ms)	42.2 ± 3.2	45.9 ± 1.6	40.8 ± 5.2	16.5 ± 2.6
Latency (ms)	3.4 ± 0.3	3.8 ± 0.3	3.7 ± 0.4	1.6 ± 0.2
20-80% rise time (ms)	1.6 ± 0.4	1.8 ± 0.3	2.5 ± 0.1	0.7 ± 0.1
uIPSC decay τ (ms)	19.9 ± 5.5	27.2 ± 5.2	40.7 ± 6.8	16.4 ± 4.4
Peak amp. of uIPSC (pA)[a]	12.0 ± 4.5	1.7 ± 0.5	9.2 ± 5.8	32.5 ± 8.9
Peak amp. of uIPSC$_1$ (pA)[b]	118.0 ± 78.3	16.1 ± 3.5	14.5 ± 8.7	24.0 ± 9.0
Charge transfer per AP (pC)[a]	0.18 ± 0.08	0.03 ± 0.01	0.15 ± 0.06	0.51 ± 0.15
Charge transfer per AP (pC)[b]	2.03 ± 1.14	0.31 ± 0.08	0.43 ± 0.23	0.29 ± 0.07
Failure rate of uIPSC[a]	0.68 ± 0.07	0.91 ± 0.02	0.59 ± 0.11	0.07 ± 0.05
Failure rate of uIPSC$_1$[b]	0.20 ± 0.05	0.21 ± 0.07	0.39 ± 0.07	0.17 ± 0.07
Multiple-pulse depression[c]	0.73 ± 0.15	0.68 ± 0.26	0.65 ± 0.05	0.44 ± 0.04

[a] uIPSCs were measured during the single firing mode, including failures.

[b] uIPSCs were measured during the burst firing mode, including failures.

[c] Multiple-pulse depression (25 Hz) was defined as IPSC$_5$/IPSC$_1$.

Data from rigorously confirmed CB$_1$R$^+$IN-to-GC (n=5), HICAP-to-GC (n=7), HIPP-to-GC (n=4) and PV$^+$BC-to-GC (n=4) pairs.

CURRICULUM VITAE

Yu-Chao Liu

Ph.D.

Institute of Neuroscience

National Yang-Ming University

Email: rainnyhunter@gmail.com

Last updated: 2014/2/5

Education

2009-2014 National Yang-Ming University, Ph.D. Neuroscience

2006-2009 National Chung Hsing University, B.S. Life Sciences

Research Interests

Neurophysiology; Synaptic physiology; Functional connectome; Network modeling; Brain-machine interface.

Publications

Liu YC, Cheng JK, Lien CC. Rapid Dynamic Changes of Dendritic Inhibition in the Dentate Gyrus by Presynaptic Activity Patterns. ***J Neurosci*** 2014 Jan; 34 (4): 1344-1357.

Lee YC, Alexandra D, Majczenko K, Huang YH, **Liu YC**, Lien CC, Tsai PC, Ichikawa Y, Goto J, Monin ML, Li JZ, Chung MY, Mundwiller E, Shakkottai V, Liu TT, Tesson C, Lu YC, Brice A, Tsuji S, Burmeister M, Stevanin G, Soong BW. Mutations in KCND3 cause spinocerebellar ataxia type 22. ***Ann Neurol*** 2012 Dec; 72 (6): 859-69.

Chiang PH*, Wu PY*, Kuo TW*, **Liu YC**, Chan CF, Chien TC, Cheng JK, Huang YY, Chiu CD, Lien CC. GABA is Depolarizing in Hippocampal Dentate Granule Cells of the Adolescent and

Adult Rats. ***J Neurosci*** 2012 Jan 4; 32 (1): 62-67. *Co-First author

Lin YC, **Liu YC**, Huang YY, Lien CC. High-Density Expression of Ca2+-Permeable ASIC1a Channels in NG2 Glia of Rat Hippocampus. ***PLoS ONE*** 2010 Sep 10; 5(9): e12665-72.

Honors and Awards

Best Poster Award, Rapid Dynamic Changes of Dendritic Inhibition in the Dentate Gyrus by Presynaptic Activity Patterns, Annual Meeting of Taiwan Neuroscience Society Program, 2013

Poster Presentations

Liu YC, Lien CC. Rapid Dynamic Changes of Dendritic Inhibition in the Dentate Gyrus by Presynaptic Activity Patterns. In: The First Bilateral Israel – Taiwan Life Science Conference, Dec 2013.

Liu YC, Lien CC. Rapid Dynamic Changes of Dendritic Inhibition in the Dentate Gyrus by Presynaptic Activity Patterns. In: Annual Meeting of Taiwan Neuroscience Society Program, Oct 2013.

Liu YC, Lien CC. Differential Dynamic Switch of GABA Release in the Hippocampus. In: The Joint Annual Conference of Biomedical Science, Mar 2013.

Liu YC, Lien CC. Distinct Dynamic Switch of GABA Release in Dendritic- and Perisomatic-Targeting Interneurons. In: Society for Neuroscience Annual Meeting, Oct 2012.

Liu YC, Cheng Irene HJ, Lien CC. Impaired Somatic Inhibition in the Hippocampus in an Animal Model of Alzheimer's Disease. In: Society for Neuroscience Annual Meeting, Nov 2011.

APPENDIX

Publication: **Liu YC**, Cheng JK, Lien CC. Rapid Dynamic Changes of Dendritic Inhibition in the Dentate Gyrus by Presynaptic Activity Patterns. *J Neurosci* 2014 Jan; 34 (4): 1344-1357.

1344 • The Journal of Neuroscience, January 22, 2014 • 34(4):1344–1357

Systems/Circuits

Rapid Dynamic Changes of Dendritic Inhibition in the Dentate Gyrus by Presynaptic Activity Patterns

Yu-Chao Liu,[1] Jen-Kun Cheng,[3] and Cheng-Chang Lien[1,2]

[1]Institute of Neuroscience, National Yang-Ming University, Taipei 112, Taiwan, [2]Brain Research Center, National Yang-Ming University, Taipei 112, Taiwan, and [3]Department of Anesthesiology, Mackay Memorial Hospital, Mackay Junior College of Medicine, Nursing and Management College; and Department of Medicine, Mackay Medical College, Taipei, Taiwan

The dentate gyrus (DG) serves as a primary gate to control information transfer from the cortex to the hippocampus. Activation of incoming cortical inputs results in rapid synaptic excitation followed by slow GABA-mediated (GABAergic) synaptic inhibition onto DG granule cells (GCs). GABAergic inhibitory interneurons (INs) in the DG comprise fast-spiking (FS) and non–fast-spiking (non-FS) cells. Anatomical analyses of DG INs reveal that FS cells are soma-targeting INs, whereas non-FS cells are dendrite-targeting INs. These two IN classes are differentially recruited by excitatory inputs and in turn provide exquisite spatiotemporal control over GC activity. Yet, little is known how FS and non-FS cells transform their presynaptic dynamics into varying postsynaptic response amplitudes. Using paired recordings in rat hippocampal slices, we show that inhibition in the DG is dominated by somatic GABAergic inputs during periods of sparse presynaptic activity, whereas dendritic GABAergic inputs are rapidly shifted to powerful and sustained inhibition during periods of intense presynaptic activity. The variant dynamics of dendritic inhibition is dependent on presynaptic IN subtypes and their activity patterns and is attributed to Ca^{2+}-dependent increases in the probability of release and the size of the readily releasable pool. Furthermore, the degree of dynamic GABA release can be reduced by blocking voltage-gated K^{+} channels, which increases the efficacy of dendrite-targeting IN output synapses during sparse firing. Such rapid dynamic modulation of dendritic inhibition may act as a frequency-dependent filter to prevent overexcitation of GC dendrites and thus set the excitatory–inhibitory synaptic balance in the DG circuits.

Key words: feedforward inhibition; GABA; hippocampus; interneuron; paired recording; readily releasable pool

Introduction

Local-circuit GABA-releasing (GABAergic) inhibitory interneurons (INs) provide inhibition to control neuronal activity (Freund and Buzsáki, 1996; McBain and Fisahn, 2001; Klausberger and Somogyi, 2008). Two distinct classes of inhibitory INs, soma-targeting and dendrite-targeting INs, mediate the inhibitory control. Soma-targeting INs control the spike initiation of principal neurons (PNs) via axonal innervations onto perisomatic areas of PNs (Cobb et al., 1995; Miles et al., 1996), whereas dendrite-targeting INs regulate dendritic electrical and biochemical signaling and synaptic plasticity by innervating dendritic domains of PNs (Miles et al., 1996; Leão et al., 2012; Chiu et al., 2013). On the basis of microcircuit structures, two inhibitory loops are identified. Feedforward inhibition arises when excitatory afferent inputs to cortical areas diverge onto both PNs and local GABAergic INs, which in turn inhibit PNs (Buzsáki, 1984; Pouille and Scanziani, 2001). Feedback inhibition is generated when activated PNs excite local INs, which in turn send inhibitory outputs back to a group of PNs, including those that initially activated the INs (Pouille and Scanziani, 2004).

Feedforward and feedback inhibition serves distinct network functions. Feedforward inhibition enables cortical neurons to accurately report temporal information by shortening the time window of EPSP summation (Pouille and Scanziani, 2001). In contrast, feedback inhibition scales GABAergic inhibition to local excitatory output, thereby contributing to the generation of rhythmic activities (Mann et al., 2005). Sparse firing of dentate gyrus (DG) granule cells (GCs) is thought to be important for rapid pattern separation and spatial information encoding (Leutgeb et al., 2007; McHugh et al., 2007; Moser et al., 2008). The relatively uniform GCs are supported by a rich diversity of GABAergic INs that provide general inhibition and also temporally regulate GC activity. In the DG, parvalbumin-expressing basket cells (PV^{+}BCs), a class of soma-targeting INs, generate reliable and powerful phasic inhibition (Kraushaar and Jonas, 2000), whereas cholecystokinin (CCK)-expressing INs, which innervate the proximal parts of GC dendrites, release GABA in a

Received June 18, 2013; revised Dec. 2, 2013; accepted Dec. 5, 2013.

Author contributions: Y.-C.L., J.-K.C., and C.-C.L. designed research; Y.-C.L. performed research; Y.-C.L. analyzed data; C.-C.L. wrote the paper.

This work was supported by the Ministry of Education (Aim for the Top University Plan), the National Health Research Institutes (NHRI-EX102-10105NI), the National Science Council (NSC101-2321-B-010-024, NSC100-2320-B-010-014-MY3), and the Cheng Hsin General Hospital (Grant 100-53 and 100F117CY19). We thank M. Bartos, P. Geshwill, D. Engel, A.J. Ruiz, and H.W. Tao for critically reading this manuscript and their comments on this manuscript; P. Somogyi (Oxford University) for help with cell identification; T. Klausberger for providing the *in vivo* interneuron spiking trains; and members of the C.-C.L. laboratory for discussions.

Correspondence should be addressed to Dr. Cheng-Chang Lien, Institute of Neuroscience, National Yang-Ming University 155, Section 2, Li-Nong Street, Taipei 112, Taiwan. E-mail: cclien@ym.edu.tw.

DOI:10.1523/JNEUROSCI.2566-13.2014

0270-6474/14/341344-14$15.00/0

highly asynchronous manner, thus generating long-lasting inhibition (Hefft and Jonas, 2005). In contrast, synaptic inhibition provided by other types of GABAergic INs has not been investigated. Hippocampal INs *in vivo* fire in bursts, with variable number and frequency of spikes (Bragin et al., 1995), but presynaptic spikes do not all give rise to identical postsynaptic responses. It is not known how GABAergic INs transform their dynamics into varying postsynaptic response amplitudes.

With rigorous anatomical reconstruction, we here examined properties of GABAergic synapses between INs and target GCs. We found that dendrite-targeting INs generate weak and less reliable inhibition onto GCs during sparse firing compared with soma-targeting INs. However, dendritic inhibition is rapidly switched to the robust and reliable mode during bouts of raised presynaptic activity. Such rapid dynamic changes are presynaptic IN activity- and Ca^{2+}-dependent. Our results reveal a rapid frequency-dependent modulation of dendritic inhibition, a key strategy through which the DG can maintain a balance of excitation and inhibition at different states of cortical activity.

Materials and Methods

Slice preparation and electrophysiology. Male Sprague Dawley rats (16–25 d postnatal) were killed by rapid decapitation without anesthesia, in accordance with national and institutional guidelines. All experimental protocols involving animals were reviewed and approved by the Institutional Animal Care and Use Committee of National Yang-Ming University. Their brains were rapidly removed, and 300-μm-thick transverse hippocampal slices were cut in ice-cold sucrose solution containing the following (in mM): 87 NaCl, 25 $NaHCO_3$, 1.25 NaH_2PO_4, 2.5 KCl, 10 glucose, 75 sucrose, 0.5 $CaCl_2$, and 7 $MgCl_2$ using a vibratome (DTK-1000, Dosaka). Slices were incubated in the sucrose solution (equilibrated with 95% O_2 and 5% CO_2) in a holding chamber at 34°C for 40 min and kept in the same chamber at room temperature (23 ± 2°C) until used. During experiments, slices were placed in a recording chamber and superfused with oxygenated artificial CSF (ACSF) containing the following (in mM): 125 NaCl, 25 $NaHCO_3$, 1.25 NaH_2PO_4, 2.5 KCl, 25 glucose, 2 $CaCl_2$, and 1 $MgCl_2$. The recording temperature was 23 ± 2°C in the majority of experiments and 35 ± 2°C in a subset (see Fig. 9).

Recording electrodes (3–7 MΩ) were pulled from borosilicate glass (outer diameter, 1.5 mm; thickness 0.32 mm; Harvard apparatus). Putative INs were first identified at the border between the granule cell layer (GCL) and the hilus by their relatively large somata (diameter >10 μm) under infrared and differential interference contrast microscope (Olympus BX51WI) coupled with an infrared-sensitive CCD camera (Hamamatsu, C7500–50) and then confirmed by their electrophysiological characteristics. Cell-attached recordings (pipette resistance 3–5 MΩ) were made to detect spike responses of single INs (Lien et al., 2006). Spikes were orthodromically evoked by glass electrodes (tip diameter ~10 μm; filled with ACSF) or bipolar tungsten electrodes (MicroProbes) placed in different DG molecular layers. Trains of 10 pulses (100 μs) at 50 Hz at near-threshold intensities were delivered every 5 s using a stimulus isolator (Isoflex, A.M.P.I.). With near-threshold intensities, each train triggered at least one spike in >50% of trials, and the probability of spike generation triggered by any stimulus did not exceed 0.8 (Pouille and Scanziani, 2004). To induce depolarization-induced suppression of inhibition (DSI), GCs were depolarized to 0 mV for 5 s. Paired recordings from synaptically coupled presynaptic INs and postsynaptic GCs in the DG were made as described previously (Kraushaar and Jonas, 2000). Presynaptic INs were held near −70 mV in current clamp. One or multiple short (1 ms duration) current pulses were delivered to evoke single or clustered APs. Postsynaptic cells were held at −80 mV in voltage clamp. Whole-cell patch-clamp recordings were made using a Multiclamp 700B amplifier (Molecular Devices). Pipette capacitances of both electrodes were carefully compensated (by >95%), and series resistance (R_s) was compensated using the automatic bridge balance (readouts after compensation were 9–28 MΩ). Signals were filtered at 4 kHz using the 4-pole low-pass Bessel filter. A Digidata 1440A (Molecular Devices) connected to a personal computer was used for stimulus generation and data acquisition. The sampling frequency was 10 kHz. Pulse sequences were generated by pClamp 10.2 (Molecular Devices). No correction for liquid junction potentials was made.

Solutions and drugs. The pipette solution for cell-attached recordings contained the following (mM): 141.5 K-gluconate, 13.5 KCl, 0.1 EGTA, 2 $MgCl_2$, 4 Na_2ATP, and 10 HEPES. For whole-cell patch-clamp recordings, the intracellular solution for presynaptic cells contained the following (mM): 135 K-gluconate, 20 KCl, 2 $MgCl_2$, 4 Na_2ATP, 10 HEPES, and 0.4% biocytin. For postsynaptic GC recordings, the intracellular solutions contained the following (mM): 15 K-gluconate, 140 KCl, 0.1 EGTA, 2 $MgCl_2$, 4 Na_2ATP, 10 HEPES, and 0.4% biocytin; or 135 K-gluconate, 20 KCl, 0.1 EGTA, 2 $MgCl_2$ 4 Na_2ATP, 10 HEPES, and 0.4% biocytin; for postsynaptic IN recordings, the intracellular solutions contained the following (mM): 135 K-gluconate, 20 KCl, 2 $MgCl_2$, 4 Na_2ATP, 10 HEPES, and 0.4% biocytin; pH adjusted to 7.3 with KOH. EGTA-AM was purchased from Invitrogen; all other chemicals were purchased from Sigma.

Image acquisition, 3D reconstruction, and axonal density analysis. For 3D reconstruction of biocytin-labeled cells, high-resolution two-photon images of INs were acquired. Labeled INs were examined by a two-photon microscope using a pulsed titanium: sapphire laser (Chameleon-Ultra II tuned to 800 nm; Coherent) attached to a Leica DM6000 CFS (Leica) that was equipped with a 63×/0.9 numerical aperture water-immersion objective (objective type HCX APO L). The morphology of the cells was reconstructed from a stack of 51–179 images per cell (voxel size, 271–758 nm in the *x-y* plane; 1 μm along the *z*-axis). Image stacks belonging to one cell were imported into the Neuromantic 1.6.3 software (Myatt et al., 2012) for 3D reconstruction. To quantify the axonal density along the radial axis, we counted the number of intersections made by the axons with lines running parallel to the border between the GCL and the molecular layer and interspaced by 10 μm (Pouille and Scanziani, 2004).

Data analysis and statistics. Data were analyzed using Clampfit 10.2 (Molecular Devices) and Prism 5.0 (GraphPad). The synaptic latency was measured from the peak amplitude of the action potential (AP) to the 10% rise time of the unitary IPSC (uIPSC) (Glickfeld and Scanziani, 2006); the decay time constant of the uIPSC was fitted with a single exponential; the coefficient of variation (CV) of the interspike intervals (ISIs) was calculated from 1 s spike train elicited in response to current pulse (0.6 nA) injection (Lien and Jonas, 2003). The input resistance (R_{in}) was measured by the ratio of the steady-state (average of the last 100 ms) voltage response versus the injected 1 s hyperpolarizing (100 pA) current pulse. The membrane time constant (τ_m) was calculated using a single-exponential fit to the late portion of the voltage change produced by hyperpolarizing (100 pA) current pulse injection in the current-clamp mode at the resting membrane potential. To estimate the change of the readily releasable pool (RRP) size, AP trains (60 stimuli; 25 Hz) were delivered at 5 s after single and burst stimulations. The RRP size was quantified with a charge integral of the synaptic current (Moulder and Mennerick, 2005; Stevens and Williams, 2007). Linear regression fits to cumulative IPSC area plots after 1 s were back-extrapolated to estimate the cumulative area (RRP charge) at time 0. Data were presented as mean ± SEM, and *n* indicates the number of cells or pairs studied. Error bars indicate SEM and were plotted only when they exceeded the respective symbol size. Statistical significance was tested by the Wilcoxon rank-sum or Wilcoxon signed-rank test at the significance level (*p*) as indicated, using Prism 5.0.

Results

Functional and anatomical dichotomies between non–fast spiking (non-FS) and FS INs in the DG

To study the role of INs in the DG circuitry, experiments were initiated by establishing whole-cell recordings from GABAergic inhibitory INs located between the GCL and the hilus, then correlating their intrinsic properties with morphologies. Based on their firing properties in response to step current injection, GABAergic inhibitory INs were classified as non-FS and FS INs (Fig. 1*A*). Non-FS INs generated relatively slow, accommodating firing patterns during depolarizing current steps (Fig. 1*A*, left).

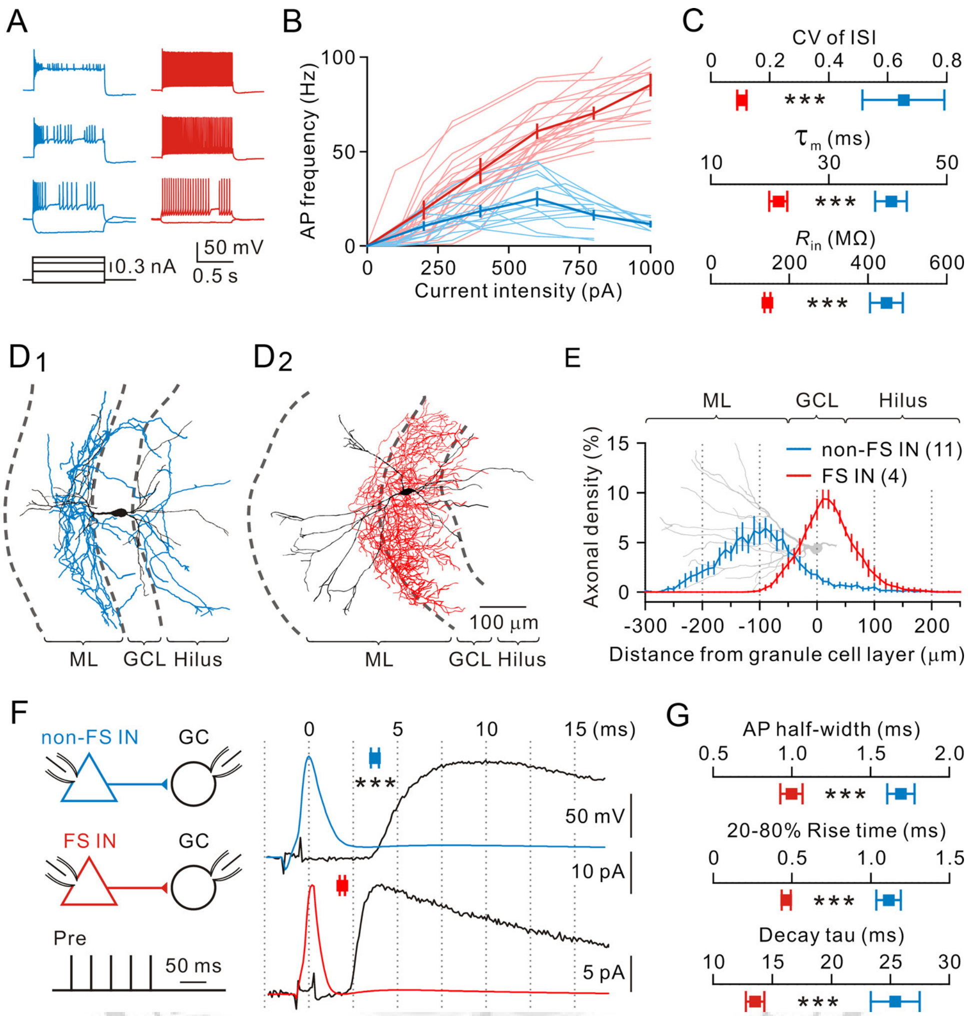

Figure 1. Intrinsic, morphological, and synaptic properties of non-FS and FS cells. ***A***, Exemplar voltage responses evoked by a series of current pulses in a non-FS (blue) and an FS (red) cell. Current during the pulse was −0.1, 0.3, 0.6, and 0.8 nA. Membrane potential before the pulse was −70 mV. ***B***, The relationship between the mean AP frequency and injected current for a subset of representative non-FS ($n = 14$) and FS ($n = 16$) cells. Individual cells were in lighter color, and the average values were darker. ***C***, Summary of CV of ISI, τ_m, and R_{in} of non-FS (blue, $n = 6$–13) and FS (red, $n = 7$–17) cells. ***$p < 0.0005$. ***D***, Exemplar reconstruction of a non-FS IN (***D***$_1$), which had the main axonal distribution (blue) outside the GCL, and an FS IN (***D***$_2$), which had the major axonal distribution (red) within the GCL. Somata and dendrites are indicated in black. ML, Molecular layer. ***E***, Axonal density distribution for non-FS ($n = 11$) and FS ($n = 4$) INs plotted against distance from the GCL. A reconstructed GC (gray) is aligned and scaled to the plot for reference. ***F***, Left, Schematic of paired recordings from a non-FS IN (blue)-to-GC (black) pair and a FS IN (red)-to-GC pair. Bursts of five APs were evoked in the non-FS IN and the FS IN by injection of brief current pulses (1 ms, 25 Hz) every 5 s. Presynaptic INs were current clamped at −70 mV, whereas postsynaptic GCs were voltage clamped at −80 mV. Right, The first AP from non-FS (blue) and FS (red) INs and their corresponding average uIPSCs (average of 70 and 73 sweeps, respectively, currents were inverted for clarity) in the target GCs (black) on an expanded time scale (vertical lines are separated by 2.5 ms). Squares represent average uIPSC latencies for non-FS ($n = 11$) and FS cells ($n = 10$). ***$p < 0.0005$. ***G***, Summary of AP half-width (blue, $n = 8$; red, $n = 10$), 20–80% rise time (blue, $n = 10$; red, $n = 12$), and decay time constant (blue, $n = 9$; red, $n = 12$). ***$p < 0.0005$.

The mean firing frequency did not increase monotonically with the injected current intensity (from 0.1 to 1 nA), but rather showed a maximal value (25 ± 4 Hz, $n = 14$) at an intermediate current intensity (0.6 nA; Fig. 1*B*, blue traces). In contrast, FS INs exhibited fast, nonaccommodating firing patterns (mean firing frequency, 61 ± 4 Hz at 0.6 nA, $n = 16$; Fig. 1*A*, right) with deep, fast afterhyperpolarization, and the mean firing frequency increased monotonically with the current intensity from 0.1 to 1 nA (Fig. 1*B*, red traces). Non-FS and FS INs also differed significantly in their CV of ISI (non-FS INs, 0.65 ± 0.14, $n = 15$; FS INs, 0.11 ± 0.02, $n = 15$; $p < 0.0005$, Wilcoxon rank-sum test), τ_m (non-FS INs, 40.6 ± 2.7 ms, $n = 14$; FS INs, 21.5 ± 1.5 ms, $n = 16$; $p < 0.0005$, Wilcoxon rank-sum test), and R_{in} (non-FS INs, 447 ± 42 MΩ, $n = 15$; FS INs, 144 ± 8 MΩ, $n = 15$; $p < 0.0005$, Wilcoxon rank-sum test) (Fig. 1*C*). To further correlate intrinsic properties with the morphologies of FS and non-FS INs, we filled cells with biocytin in a subset of recordings and recovered their morphologies after experiments. Anatomical analysis revealed that non-FS and FS INs had distinctive axonal distribution patterns (Fig. 1*D*$_1$,*D*$_2$). With the GCL as reference (Fig. 1*E*), reconstructed non-FS INs had the majority of axonal density distributions outside the GCL (in the ML), whereas FS INs had the highest axonal density distribution within the GCL.

We next compared the functional properties of non-FS IN and FS IN output synapses in paired recordings (Fig. 1*F*). Inhibitory synaptic connections were identified by evoking uIPSCs in GCs with five brief depolarizing current pulses (1 ms at 25 Hz; 5 s interval) applied in presynaptic INs. Several differences were detected between non-FS IN-to-GC and FS IN-to-GC synapses. First, presynaptic AP half-width of non-FS INs was significantly longer than that of FS INs (non-FS INs, 1.69 ± 0.09 ms, $n = 10$; FS INs, 1.00 ± 0.07 ms, $n = 8$; $p < 0.0005$, Wilcoxon rank-sum test; Fig. 1*G*). Second, 20–80% rise time (non-FS INs, 1.11 ± 0.08 ms, $n = 12$; FS INs, 0.46 ± 0.03 ms, $n = 10$; $p < 0.0005$,

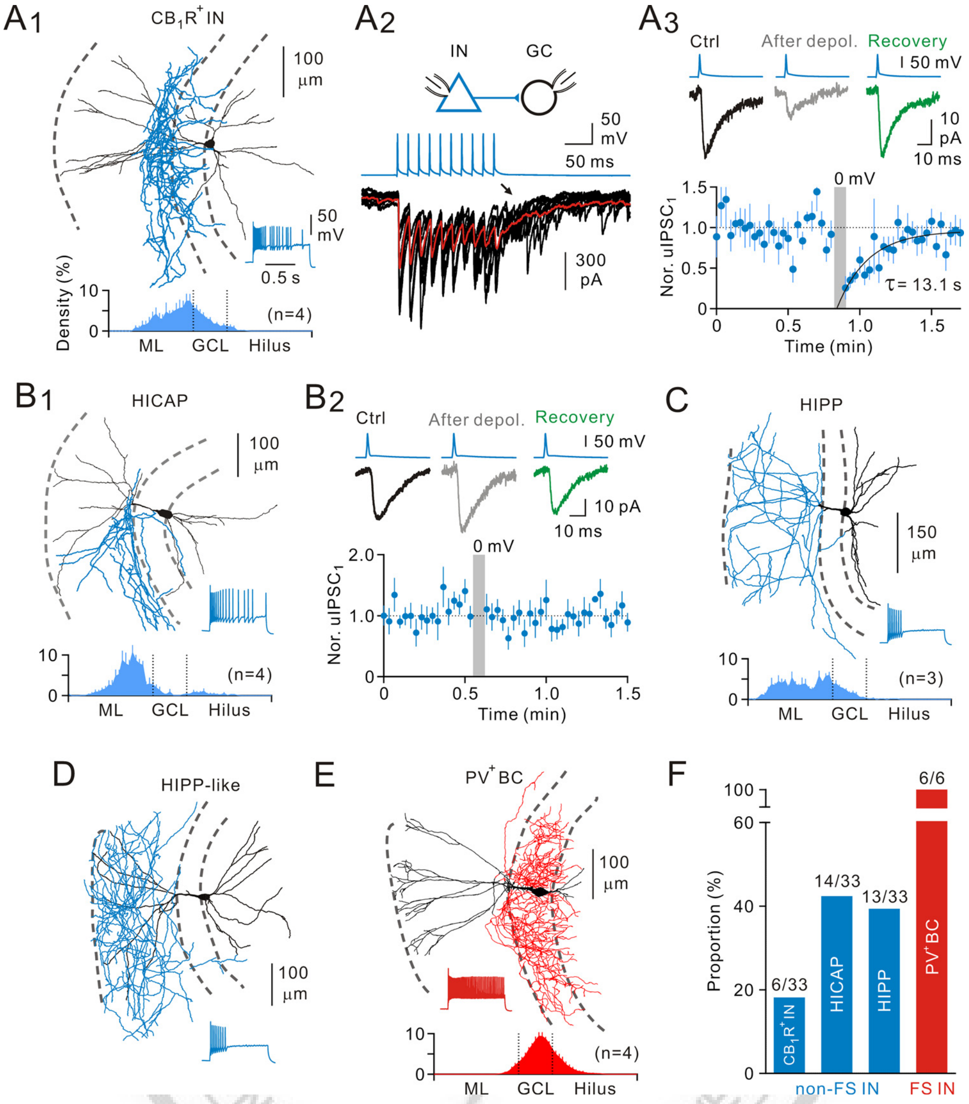

Figure 2. Heterogeneity of non-FS INs. ***A***, A non-FS cell (***A$_1$***), a putative CB$_1$R$^+$ IN, with the axonal distribution within the IML (bottom, density plot) exhibited asynchronous release onto GCs (***A$_2$***, arrow) and DSI (***A$_3$***). To induce DSI, GCs were depolarized to 0 mV for 5 s. Eight single uIPSC sweeps are superimposed in ***A$_2$***; red curve is the average of 35 sweeps. ***A$_3$***, Top, uIPSC traces in control, after depolarization, and recovery from DSI; uIPSC traces are average of 8–25 sweeps. Bottom, Summary of the time course of uIPSC suppression from putative CB$_1$R$^+$ IN-to-GC pairs ($n = 5$). Recovery is fitted with a single exponential function. CB$_1$R$^+$, Cannabinoid receptor type 1 (+). ***B***, A non-FS cell, a putative hilar C/A pathway-related (HICAP) cell (***B$_1$***), had the main axonal innervation in the IML. ***B$_2$***, HICAP cells had no DSI response (average of 10 pairs). The dendritic processes penetrated the GCL and radially ascended into the ML, whereas the remaining dendrites ramified in the hilus. Bottom, Axonal density plot. ***C***, A non-FS cell, a typical hilar PP-associated (HIPP) cell, had the axonal distribution in the PP terminal field. There are dendrites strictly in the hilus. Bottom, Axonal density plot. ***D***, An exemplar atypical HIPP-like cell, which had the axonal distribution of HIPP cells, but the dendrites ramified in the ML, in addition to the hilus. ***E***, An FS cell, a putative PV$^+$BC with the axonal distribution within the GCL. There are tangential axon collaterals in the hilus and scattered boutons all along. Bottom, Axonal density plot. ***F***, Summary of morphological classification of non-FS and FS INs.

Wilcoxon rank-sum test; Fig. 1*G*) and decay time constant (non-FS INs, 25.4 ± 2.1 ms, $n = 12$; FS INs, 13.6 ± 0.8 ms, $n = 9$; $p < 0.0005$, Wilcoxon rank-sum test; Fig. 1*G*) of uIPSCs recorded from pairs of non-FS IN-to-GC synapses were significantly slower than those of FS IN-to-GC synapses. Finally, the synaptic latency was significantly longer for non-FS IN-to-GC synapses than for FS IN-to-GC synapses (non-FS INs, 3.67 ± 0.16 ms, $n = 11$; FS INs, 1.95 ± 0.14 ms, $n = 10$; $p < 0.0005$, Wilcoxon rank-sum test; Fig. 1*F*). These results were similar to previous observations (Hefft and Jonas, 2005) and were consistent with a more distal location of non-FS IN terminals on the dendrites of GCs (Fig. 1*D$_1$*).

Classification of IN subtypes

Non-FS and FS INs can be further classified into several IN subtypes based on their axonal projection patterns (Han et al., 1993; Hefft and Jonas, 2005). Non-FS INs with their somata at the border between the GCL and the hilus comprise at least three distinct subtypes: the cannabinoid receptor type 1-expressing INs (CB$_1$R$^+$INs, also known as CCK$^+$INs), the hilar IN with commissural/associational (C/A) pathway-associated (HICAP) cells and the hilar IN with PP-associated axon terminals (HIPP) cells. Unlike CB$_1$R$^+$INs in the CA1 area (Glickfeld and Scanziani, 2006), CB$_1$R$^+$INs had their axonal distribution in the inner molecular layer (IML) rather than the GCL (Hefft and Jonas, 2005). Thus, CB$_1$R$^+$INs (6 cells; Fig. 2*A$_1$*) in this study were identified by asynchronous release (Fig. 2*A$_2$*), cannabinoid sensitivity (40.6 ± 0.3% of control, $n = 5$ pairs; Fig. 2*A$_3$*), and their axonal distribution in the IML (Glickfeld and Scanziani, 2006). Cannabinoid sensitivity was tested through the DSI protocol (see Materials and Methods). Similar to CB$_1$R$^+$INs, HICAP cells also had the high-

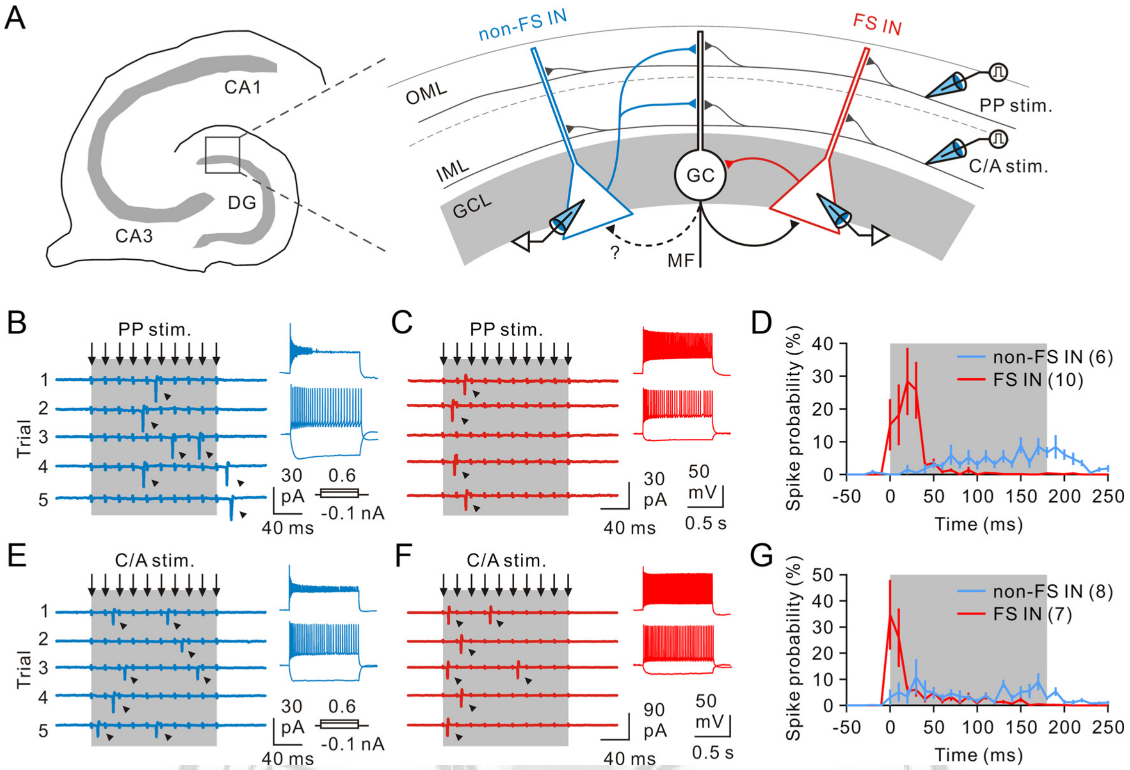

Figure 3. Differential recruitment of two IN classes by excitatory afferents. ***A***, Schematic diagram showing extracellular stimulation of afferents (PP stim. and C/A stim.) and FS-IN and non-FS IN recording configuration (not simultaneous). Black circle represents GC; blue triangle represents dendrite-targeting IN; red triangle represents soma-targeting IN. MF, Mossy fiber. There are reciprocal connections between soma-targeting INs and GCs. ***B***, Exemplar cell-attached recording of responses (arrowheads) to PP stimuli (50 Hz trains (arrows) delivered at near-threshold intensities) in a "late-onset" IN. The stimulation electrode was positioned within the OML to activate the PP pathway. Inset, Whole-cell current-clamp recording of the same cell displayed adapting, non-FS patterns in response to positive square pulse of currents. In the following figures, the spiking pattern allowing identification of the neurons as non-FS or FS cells is shown as an inset. ***C***, Same stimulation as in ***B*** triggered responses in an "early-onset" IN, which responded at the early phase of stimulations. Inset, The same cell displayed non-adapting, FS patterns upon depolarization. ***D***, Histogram showing spike probability of non-FS and FS cells in response to 10 PP stimulations. Each data point is a 10 ms bin with spike number normalized to the total spike number during stimulation. ***E***, Cell-attached recording of spike responses from a "late-onset" IN to 10 stimulations of the C/A pathways. Inset, The same cell displayed adapting, non-FS patterns upon depolarization. ***F***, Same stimulation as in ***E*** triggered spike responses of an "early-onset" IN. Inset, The same cell displayed nonadapting, FS patterns upon depolarization. ***G***, Histogram showing spike probability of non-FS and FS cells in response to C/A afferents stimulation (bin width, 10 ms).

est density of axons within the IML (Fig. 2*B*$_1$). However, in contrast to CB$_1$R$^+$INs, HICAP cells (14 cells) did not display DSI responses (103.4 ± 11.9% of control, n = 10 pairs; Fig. 2*B*$_2$). Unlike CB$_1$R$^+$INs and HICAP cells, HIPP cells (9 cells) had their axonal projection extended to the PP terminal field, whereas its dendrites were restricted to the hilus (Fig. 2*C*). Interestingly, we observed four HIPP-like cells, which projected their axons to the outer molecular layer (OML), but had the dendritic arbor in the ML and the hilus (Fig. 2*D*).

In contrast to non-FS INs, FS INs had remarkable axonal projection almost restricted within the GCL (Fig. 2*E*) and likely comprise two subtypes: axo-axonic cells (AACs) and PV$^+$BCs. AACs have prominent radial axon collaterals with vertical rows of axonal terminals, thus also termed chandelier cells, whereas PV$^+$BCs have tangential axonal collaterals with scattered boutons in the GCL (Howard et al., 2005; Hu et al., 2010). In this study, all recovered FS INs were identified as PV$^+$BCs based on their axonal projection pattern and AACs were not present (Fig. 2*E*). Summary of morphologically identified INs was shown in Figure 2*F*.

Differential recruitment of FS and non-FS INs by excitatory afferents

The DG has a distinct laminated structure and receives incoming excitatory inputs from the entorhinal cortex and the hilar regions (Förster et al., 2006; Bartos et al., 2011). The perforant path (PP) from the entorhinal cortex layer II forms a bundle and innervates the distal part of GC dendrites within the outer two thirds of the molecular layer (OML), whereas the C/A afferents, which originate from the mossy cells in the contralateral and ipsilateral hilar regions, innervate proximal GC dendrites within the IML (Fig. 3*A*). In addition to GCs, both excitatory afferents target local inhibitory INs, which critically control the GC output. To understand how INs exert their inhibition onto postsynaptic GCs in the normal DG circuitry, it is important to understand not only IN outputs, but also the nature of their inputs. To investigate how excitatory afferents recruit INs, we performed cell-attached recordings from individual INs located in or near the GCL. INs were activated by stimulating the PP with glass or bipolar tungsten electrodes placed in the OML (Fig. 3*A*; see Materials and Methods). Spikes, detected as extracellular AP currents, were recorded from the soma of presumed INs in response to trains of 10 electrical stimuli delivered at 50 Hz to the PP. Two populations of INs differed in their responses to the sustained PP afferent stimulation: the first group of INs, termed "late-onset" cells, had the low firing probability in response to the first five stimuli and rapidly increased their firing probability over the course of train stimuli (Fig. 3*B*,*D*); the second group of INs, termed "early-onset" cells, preferred to respond to the first four stimuli and responded less reliably to the latter stimuli (Fig. 3*C*,*D*). After

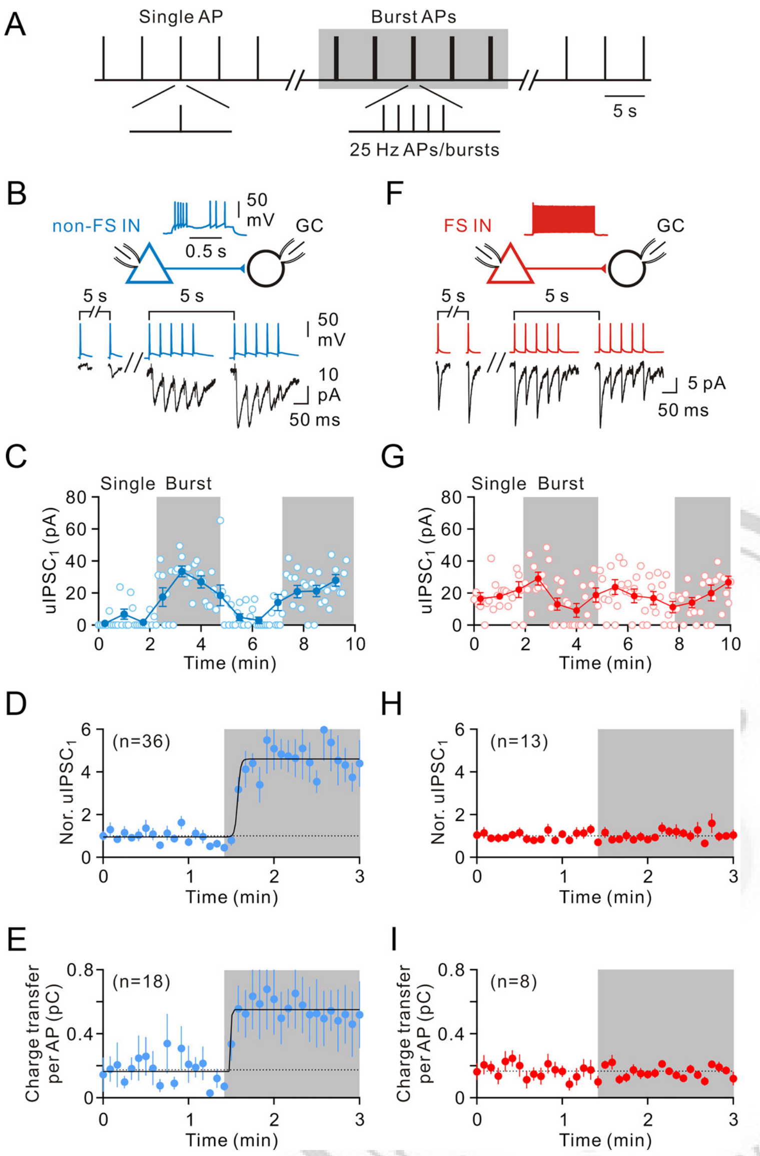

Figure 4. Cell type-specific dynamics of GABA release. ***A***, Stimulation protocol used to trigger presynaptic spikes in paired recordings between presynaptic INs and postsynaptic GCs. A single AP ("Single" mode) or a 25 Hz burst of five presynaptic APs ("Burst" mode) evoked by brief current pulses were applied at a repetition frequency of 0.2 Hz. ***B***, Paired recording between a presynaptic non-FS IN (blue) and a postsynaptic GC (black). Presynaptic IN was evoked by stimulation protocol shown in ***A*** and the corresponding uIPSCs (bottom traces, single sweeps). ***C***, Plot of the peak amplitude of the uIPSC$_1$ evoked by single APs and the uIPSC$_1$ evoked by 25 Hz burst of five APs against time; the same cell as shown in ***B***. Open circle represents individual uIPSC$_1$; filled circle represents average uIPSC$_1$ (average of 9 events). ***D***, Summary of uIPSC$_1$ from non-FS IN-to-GC pairs. ***D***, ***E***, Curves represent Boltzmann functions fitted to the data points. There is a brief delay (~10 s) before the switch of synaptic strength. ***E***, Summary of average charge transfer per AP from non-FS IN-to-GC pairs. ***F***, Similar to ***B***, paired recording from a FS IN (red)-to-GC (black) pair. Presynaptic APs (top traces) and corresponding uIPSCs (bottom traces, single sweeps). ***G***, Plot of peak amplitude of uIPSC$_1$ against time; the same cell as shown in ***F***. Open circle represents individual uIPSC$_1$; filled circle represents average uIPSC$_1$ (average of 9 events). ***H***, Summary of uIPSC$_1$ from FS IN-to-GC pairs. ***I***, Summary of average charge transfer per AP from FS IN-to-GC pairs.

cell-attached recordings, whole-cell recordings of the same cells showed that late-onset cells displayed adapting, irregular spiking at lower frequency (36 ± 2 Hz, $n = 6$; Fig. 3*B*, inset), whereas early-onset cells generated nonadapting, high-frequency spike train (63 ± 5 Hz, $n = 10$; Fig. 3*C*, inset) in response to square pulse current (0.6 nA) injection.

In addition to the PP, INs receive C/A afferents, which terminate in the IML (Fig. 3*A*). Similar to PP activation, sustained stimulation of the C/A afferents sequentially recruited early-onset and late-onset INs. In the early-onset cells, the probability of spiking was highest at the onset of the series and rapidly fell during the sustained afferent stimulation (Fig. 3*E*,*G*). In the late-onset cells, the probability of spike generation was low at the onset of the series and slightly increased over the course of train stimuli (Fig. 3*F*,*G*). Whole-cell recordings of these two types of neurons also revealed that late-onset cells displayed adapting, non-FS patterns (32 ± 3 Hz, $n = 8$; Fig. 3*E*, inset), whereas early-onset cells exhibited non-adapting, FS patterns (65 ± 5 Hz, $n = 7$; Fig. 3*F*, inset).

Rapid dynamic changes of GABA release in non-FS IN-to-GC synapses

In neurons *in vivo*, the membrane potential exhibits substantial rapid variations, during all behavioral states, because of fluctuations in synaptic bombardment (reviewed by Haider and McCormick, 2009). Cortical inhibitory INs *in vivo* fire bursts of APs at γ frequency range (20–50 Hz) during the Up state or γ and spindle oscillations (Haider et al., 2006; Massi et al., 2012). It is unclear how the spike timing of INs is translated into their output synapses in different states. To address this question, we made paired recordings between FS or non-FS INs and GCs. Postsynaptic uIPSCs recorded in GCs were evoked by applying brief current pulses to the presynaptic INs. A single AP or a 25 Hz burst of five APs was repetitively applied every 5 s (Fig. 4*A*). Synaptic transmission at 5 s interval during periods of either single AP or burst AP complex mode was found to be stable for 8 min in the absence of GABA receptor type B antagonists (data not shown). As illustrated in Figure 4*B* (left traces), non-FS IN-to-GC synapses exhibited small uIPSCs (11.7 ± 3.0 pA, $n = 18$ pairs) with a larger number of failures (0.54 ± 0.04, $n = 36$ pairs) during single AP stimulations. Interestingly, when non-FS cells fired at bursting complexes, the efficacy (28.0 ± 7.5 pA, $n = 18$ pairs; $p < 0.0005$, Wilcoxon signed-rank test) and reliability (failure rate of IPSC$_1$, 0.24 ± 0.03, $n = 36$ pairs; $p < 0.0005$, Wilcoxon signed-rank test) of neurotransmission robustly increased (Fig. 4*B*, right traces). When the peak amplitude of the first uIPSC (uIPSC$_1$) was plotted against time, the magnitude was small during single firing modes, whereas the magnitude rapidly increased during burst firing modes (Fig. 4*C*). On average, the uIPSC$_1$ magnitude increased to 412 ± 67% ($n = 36$; $p < 0.0005$, Wilcoxon signed-rank test; Fig. 4*D*). Similar results were also found when the mean charge transfer (the charge integral of the synaptic current) per AP was plotted against time during mode transitions (single, 0.18 ± 0.06 pC; burst, 0.55 ± 0.17 pC, $n = 18$; $p < 0.0005$, Wilcoxon signed-rank test; Fig. 4*E*).

In contrast, FS cells generated relatively reliable and high efficacy of GABA release during single firing modes (Fig. 4*F*,*G*).

Table 1. Functional properties of IN-to-GC connections[a]

	$CB_1R^+IN \rightarrow GC$	$HICAP \rightarrow GC$	$HIPP \rightarrow GC$	$PV^+BC \rightarrow GC$
AP half-width (ms)	1.7 ± 0.1	1.7 ± 0.1	1.9 ± 0.2	1.2 ± 0.1
CV of ISI	0.75 ± 0.20	0.80 ± 0.26	0.54 ± 0.32	0.09 ± 0.01
R_{in} (MΩ)	303 ± 13	343 ± 18	295 ± 48	109 ± 20
τ_m (ms)	42.2 ± 3.2	45.9 ± 1.6	40.8 ± 5.2	16.5 ± 2.6
Latency (ms)	3.4 ± 0.3	3.8 ± 0.3	3.7 ± 0.4	1.6 ± 0.2
20–80% rise time (ms)	1.6 ± 0.4	1.8 ± 0.3	2.5 ± 0.1	0.7 ± 0.1
uIPSC decay τ (ms)	19.9 ± 5.5	27.2 ± 5.2	40.7 ± 6.8	16.4 ± 4.4
Peak amplitude of uIPSC (pA)[b]	12.0 ± 4.5	1.7 ± 0.5	9.2 ± 5.8	32.5 ± 8.9
Peak amplitude of $uIPSC_1$ (pA)[c]	118.0 ± 78.3	16.1 ± 3.5	14.5 ± 8.7	24.0 ± 9.0
Charge transfer per AP (pC)[b]	0.18 ± 0.08	0.03 ± 0.01	0.15 ± 0.06	0.51 ± 0.15
Charge transfer per AP (pC)[c]	2.03 ± 1.14	0.31 ± 0.08	0.43 ± 0.23	0.29 ± 0.07
Failure rate of uIPSC[b]	0.68 ± 0.07	0.91 ± 0.02	0.59 ± 0.11	0.07 ± 0.05
Failure rate of $uIPSC_1$[c]	0.20 ± 0.05	0.21 ± 0.07	0.39 ± 0.07	0.17 ± 0.07
Multiple-pulse depression[d]	0.73 ± 0.15	0.68 ± 0.26	0.65 ± 0.05	0.44 ± 0.04

[a] Data from rigorously confirmed CB_1R^+IN-to-GC ($n = 5$), HICAP-to-GC ($n = 7$), HIPP-to-GC ($n = 4$), and PV^+BC-to-GC ($n = 4$) pairs.

[b] uIPSCs were measured during the single firing mode, including failures.

[c] uIPSCs were measured during the burst firing mode, including failures.

[d] Multiple-pulse depression (25 Hz) was defined as $IPSC_5/IPSC_1$.

While FS cells fired at burst modes, they maintained stable transmission during burst of 5 APs (Fig. 4*F*). Unlike the non-FS IN synapses, the $uIPSC_1$ magnitude (single, 12.8 ± 1.5 pA; burst, 12.0 ± 1.8 pA, $n = 8$; $p = 0.82$, Wilcoxon signed-rank test; Fig. 4*H*), the failure rate of $IPSC_1$ (single, 0.21 ± 0.06; burst, 0.22 ± 0.06, $n = 13$; $p = 0.67$, Wilcoxon signed-rank test; data not shown), and the mean charge transfer (single, 0.17 ± 0.02 pC; burst, 0.16 ± 0.01 pC, $n = 8$; $p = 0.31$, Wilcoxon signed-rank test) per AP were unchanged after transition to burst firing modes (Fig. 4*I*).

Heterogeneity of dendrite-targeting IN output synapses

As illustrated in Figure 2, dendrite-targeting INs are heterogeneous and the properties of most GABAergic synapses between dendrite-targeting INs and GCs are unknown (Hefft and Jonas, 2005). With rigorous anatomical reconstruction, we have identified three subtypes (CB_1R^+, HICAP, and HIPP) of dendrite-targeting INs. In agreement with the distance of their axonal termination to the GC soma (Fig. 2), both uIPSC rise time and decay τ were fast at the CB_1R^+IN-GC synapse, modest at the HICAP-GC synapse, and slow at the HIPP-GC synapse (Table 1). Our present study provides, to our knowledge, the first description of their synaptic strength and properties. The main points are as follows. First, the peak amplitude of uIPSC and the charge transfer per AP at the HICAP-GC synapse (1.7 ± 0.5 pA; 0.03 ± 0.01 pC, $n = 7$) are much smaller than those at the CB_1R^+IN-GC synapse (13.5 ± 5.6 pA; 0.2 ± 0.1 pC, $n = 4$) and the HIPP-GC synapse (10.4 ± 8.0 pA; 0.15 ± 0.09 pC, $n = 3$) during basal transmission. Second, the degree (~10-fold) of dynamic change of both CB_1R^+IN and HICAP cell output synapses is greater than that (~1.5- to 3-fold) of the HIPP output synapse during mode-transitions. Third, the mean charge transfer per AP of the CB_1R^+IN-GC synapse (2.41 ± 1.39 pC, $n = 4$) is substantially larger than those of the HICAP-GC (0.31 ± 0.08 pC, $n = 7$), HIPP-GC (0.48 ± 0.32 pC, $n = 3$), and PV^+BC-GC (0.29 ± 0.07 pC, $n = 4$) synapses during the burst mode, indicating that CB_1R^+IN-mediated asynchronous release provides the main inhibitory control onto GCs.

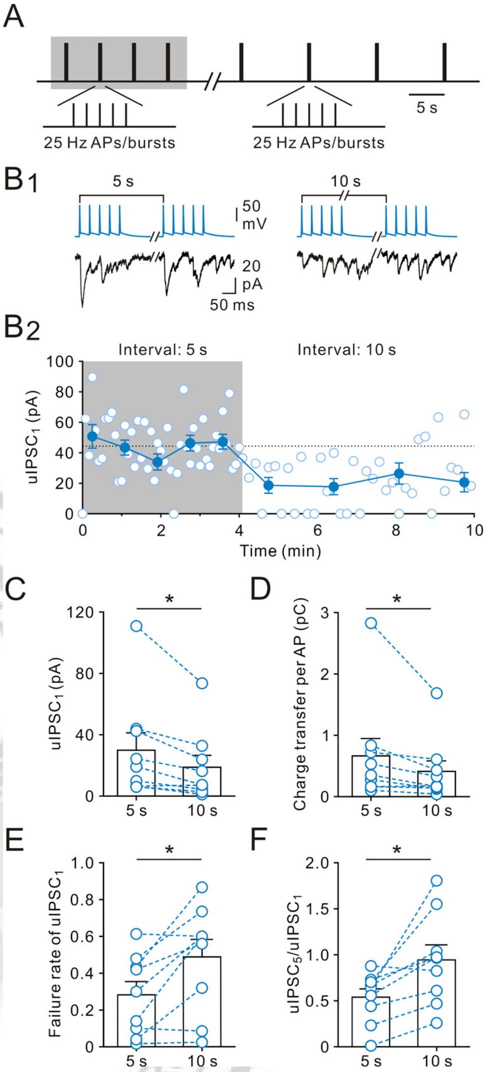

Figure 5. Presynaptic activity-dependent fast dynamic switches of GABA release. ***A***, Stimulation protocol: 25 Hz bursts of presynaptic five APs were evoked repetitively at 5 or 10 s intervals. ***B*₁**, Presynaptic APs (top) and postsynaptic uIPSCs (bottom, single sweeps). ***B*₂**, Peak amplitude of $uIPSC_1$ is plotted against time. The peak amplitude of $uIPSC_1$ was rapidly decreased after the transition. ***C***, Summary of $uIPSC_1$ amplitude at 5 and 10 s intervals. $^*p < 0.05$. ***D***, Summary of mean integral of uIPSC per AP at 5 and 10 s intervals. $^*p < 0.05$. ***E***, Summary of failure rate at 5 and 10 s intervals. $^*p < 0.05$. ***F***, Summary of multiple-pulse ratio ($uIPSC_5/uIPSC_1$). Bars represent mean values; circles connected by dashed lines represent data from the same experiment. $^*p < 0.05$.

Dynamic GABA release is sensitive to presynaptic activity patterns and Ca^{2+} buffers

The synaptic strength at non-FS IN-to-GC synapses was rapidly switched from low to high release during mode transitions, whereas the dynamics of FS IN-to-GC synapses was relatively independent of presynaptic activity. For non-FS INs, the marked increase in GABA release suggests that the probability of release rapidly increased during AP bursts, which persisted until the first AP of the next burst at 5 s later. To further examine the presynaptic activity dependence at non-FS IN-to-GC synapses, we prolonged the interburst interval from 5 to 10 s (Fig. 5*A*). As illustrated in Figure 5*B*, the $uIPSC_1$ magnitude and the mean charge transfer of per AP were greatly reduced. Overall, the $uIPSC_1$ magnitude and the mean charge transfer per AP decreased to 60 ± 8% (from 30.0 ± 11.3 pA to 18.9 ± 7.7 pA, $n = 9$; $p < 0.05$, Wilcoxon signed-rank test; Fig. 5*C*) and 71 ± 7% (from 0.66 ± 0.28 pC to 0.41 ± 0.17 pC, $n = 9$; $p < 0.05$, Wilcoxon signed-rank test; Fig. 5*D*), respectively. In contrast, both the failure rate of $uIPSC_1$ (from 0.28 ± 0.07 to 0.49 ± 0.10, $n = 9$; $p < 0.05$, Wilcoxon signed-rank test; Fig. 5*E*) and the multiple-

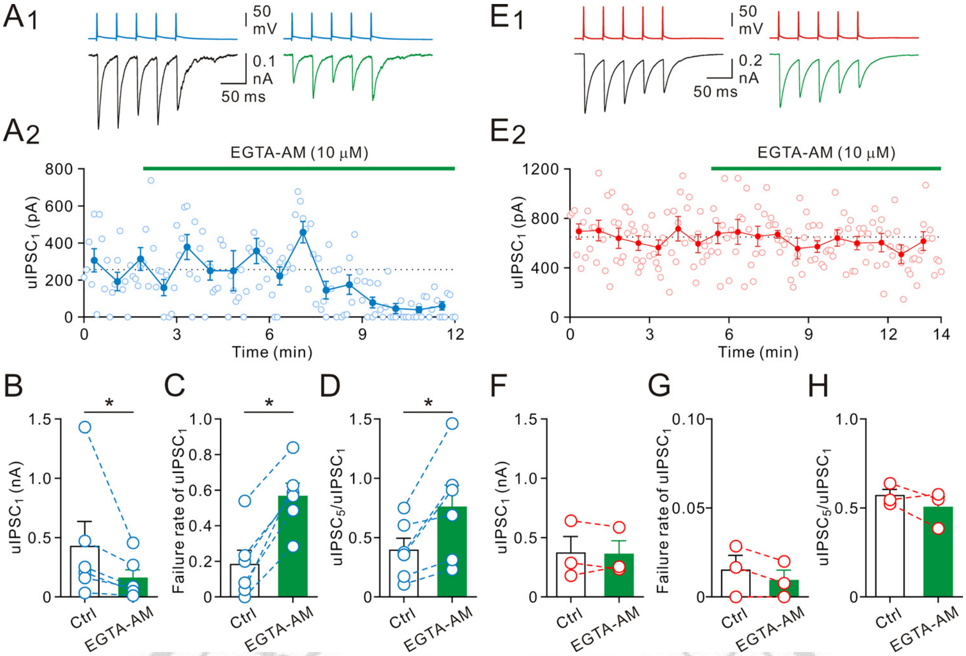

Figure 6. Membrane-permeable Ca^{2+} chelator EGTA-AM decreased GABA release in non-FS INs. ***A$_1$***, The 25 Hz bursts of five presynaptic APs and postsynaptic uIPSC traces (average of 25 sweeps). ***A$_2$***, Plot of their corresponding uIPSC$_1$ amplitude in control and after bath perfusion of EGTA-AM (10 μM). Horizontal bar represents time of EGTA-AM application. EGTA-AM also altered synaptic dynamics. ***B***, Summary of mean uIPSC$_1$ amplitude before and after addition of EGTA-AM. $*p < 0.05$. ***C***, Failure rate of uIPSC$_1$ before and after addition of EGTA-AM. $*p < 0.05$. ***D***, Multiple-pulse ratio before and after addition of EGTA-AM. $*p < 0.05$. ***E$_1$***, Simultaneous recordings of presynaptic APs evoked in a FS IN (top) and the uIPSCs in a GC (bottom, average of 40 sweeps for each). ***E$_2$***, Plot of their corresponding uIPSC$_1$ amplitude in control and after bath perfusion of EGTA-AM. ***F***, Summary of mean uIPSC$_1$ amplitude before and after addition of EGTA-AM. ***G***, Failure rate of uIPSC$_1$ before and after addition of EGTA-AM. ***H***, Multiple-pulse ratio before and after addition of EGTA-AM.

pulse ratio (uIPSC$_5$/uIPSC$_1$ from 0.54 ± 0.09 to 0.94 ± 0.16, $n = 9$; $p < 0.05$, Wilcoxon signed-rank test) were significantly increased (Fig. 5*F*). These results confirm that the use-dependent effects were generated at a presynaptic locus.

Residual elevation of presynaptic [Ca^{2+}]$_i$ as well as loose coupling between Ca^{2+} sources and synaptic vesicles may contribute to activity-dependent facilitation of GABA release during burst activities (Zucker and Regehr, 2002; Bucurenciu et al., 2008; Jonas and Vyleta, 2012). To test this hypothesis, we applied the acetoxymethylester form of EGTA (EGTA-AM, 10 μM), a slowly acting, membrane-permeable Ca^{2+} chelator to interfere with the coupling between endogenous Ca^{2+} and synaptic vesicles (Bucurenciu et al., 2008; Jonas and Vyleta, 2012). The EGTA-AM loaded into the cell can be deesterified by endogenous esterases, and the deesterified EGTA can accumulate to millimolar levels as opposed to the micromolar concentration of the EGTA-AM in the bath (Zucker and Regehr, 2002). A representative recording showed that, after 5 min bath application of EGTA-AM, the uIPSC$_1$ magnitude during burst firing markedly decreased (from 247.0 ± 31.1 pA to 54.7 ± 11.6 pA; Fig. 6*A$_1$*,*A$_2$*). On average, the uIPSC$_1$ magnitude decreased to 43 ± 7% (from 426.0 ± 209.5 pA to 158.1 ± 69.8 pA, $n = 6$; $p < 0.05$, Wilcoxon signed-rank test; Fig. 6*B*) in the presence of EGTA-AM. A similar effect on uIPSC was found during the period of single spiking (control, 23.8 ± 9.9 pA; EGTA-AM, 5.3 ± 1.8 pA; $n = 5$; data not shown). Consistent with the chelator effects on the presynaptic release machinery, the failure rate of the uIPSC$_1$ during bursting spiking increased from 0.18 ± 0.08 to 0.57 ± 0.07 ($n = 6$; $p < 0.05$, Wilcoxon signed-rank test; Fig. 6*C*) and the multiple-pulse ratio (uIPSC$_5$/uIPSC$_1$) increased from 0.39 ± 0.10 to 0.76 ± 0.19 ($n = 6$; $p < 0.05$, Wilcoxon signed-rank test; Fig. 6*D*), whereas the CV^{-2} of uIPSC$_1$ amplitude was reduced from 6.25 ± 4.12 to 2.01 ± 0.99 ($p < 0.05$, Wilcoxon signed-rank test; 6 pairs, respectively; data not shown).

Previous studies showed that GABA release at FS IN-GC synapses is insensitive to the slow Ca^{2+} chelator EGTA, suggesting that Ca^{2+} source and Ca^{2+} sensor are tightly coupled at this synapse (Hefft and Jonas, 2005; Bucurenciu et al., 2008). In agreement with those of Hefft and Jonas (2005) and Bucurenciu et al. (2008), bath application of EGTA-AM had little effect on FS IN synapses during single spiking (control, 398.2 ± 147.2 pA; EGTA-AM, 375.8 ± 126.7 pA; $n = 3$; data not shown). Similarly, the uIPSC$_1$ was not changed in the presence of EGTA-AM during burst spiking (control, 642.7 ± 27.2 pA; EGTA-AM, 587.6 ± 24.0 pA; Fig. 6*E$_1$*,*E$_2$*). On average, the uIPSC$_1$ magnitude before and after EGTA-AM application was unchanged (control, 369.5 ± 140.0 pA; EGTA-AM, 359.3 ± 114.3 pA; $n = 3$; Fig. 6*F*). Consistently, there were no changes of failure rate (control, 0.015 ± 0.008; EGTA-AM, 0.009 ± 0.006; $n = 3$; Fig. 6*G*) and the multiple-pulse ratio (control, 0.57 ± 0.04; EGTA-AM, 0.50 ± 0.06; $n = 3$; Fig. 6*H*). As non-FS IN output synapses are markedly more sensitive to Ca^{2+} chelators than FS IN output synapses, our results suggest residual presynaptic [Ca^{2+}]$_i$ and/or loose coupling between Ca^{2+} sources and synaptic vesicles in non-FS IN terminals.

The RRP size increased during periods of burst firing

In addition to increasing the probability of release, a recent study (Thanawala and Regehr, 2013) shows that presynaptic Ca^{2+} accumulation may increase neurotransmitter release in part by increasing the size of the RRP. To test the contribution of this mechanism, we depleted the RRPs in non-FS IN-GC pairs at 5 s after periods of single and burst AP firing using AP trains (Fig. 7*A*) and then compared the change of the RRP charge using cumulative methods (Moulder and Mennerick, 2005; Rizzoli and

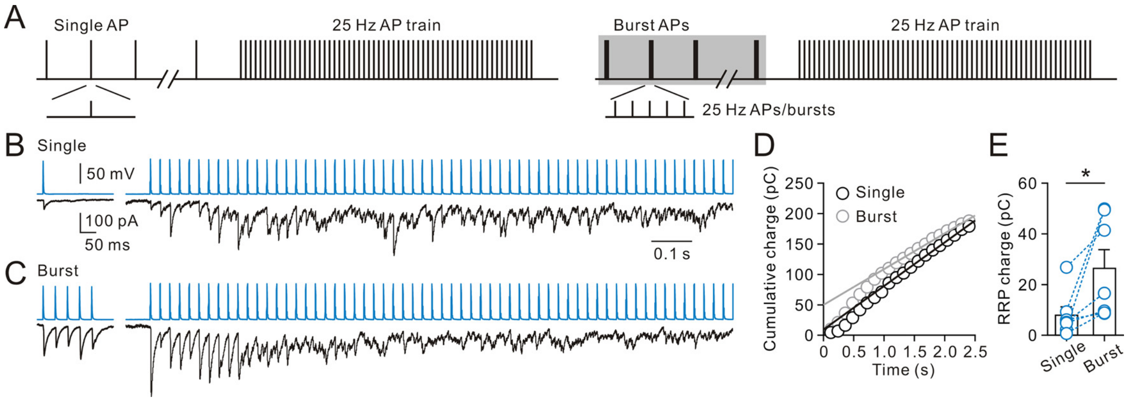

Figure 7. The RRP size increased during the burst stimulation. ***A***, Protocols showing that AP trains (60 stimuli; 25 Hz) were delivered after single (left) and burst (right) stimulations to deplete the RRP. ***B***, Representative single AP-induced uIPSC (average of 20 traces) and IPSC train (average of 2 trials) recorded from a non-FS IN-to-GC pair. Synaptic currents during AP trains show synchronous and asynchronous release. ***C***, Representative burst AP-induced uIPSC (average of 30 traces) and IPSC train (average of 3 trials) recorded from the same pair as in ***B***. ***D***, Representative cumulative IPSC area values versus time from the same 60 stimuli, 25 Hz train. Each data point is a 120 ms bin with cumulative charge. Each data point for single and burst firing is an average of 2 and 3 trials, respectively. The solid lines represent linear regression fits to data points after 1 s to estimate the cumulative area at time 0. ***E***, Summary of total RRP charge (cumulative area at time 0), as determined with trains. Circles connected by dashed lines represent data from the same cell. $^{*}p < 0.05$.

Betz, 2005; Stevens and Williams, 2007; Thanawala and Regehr, 2013).

As illustrated in Figure 7*B*, the uIPSCs during periods of single AP firing were small. After obtaining stable release during periods of single AP firing, AP trains of 60 stimuli at 25 Hz were delivered. The synaptic responses to the first 5 APs were small and then transiently increased during the train, but soon depressed and reached an apparent steady state. Notably, synaptic currents displayed synchronous and asynchronous release. After the recovery from train-induced depletion, INs were then stimulated in the burst mode. In agreement with non-FS IN output synapses, the uIPSC rapidly increased after transition to burst firing and then reached a steady state. To deplete the RRP, the same AP trains were delivered to INs. As illustrated in Figure 7*C*, synaptic responses were initially large, but rapidly depressed and reached an apparent steady state over the course of 60 stimuli, indicating the rapid depletion of the RRP. Furthermore, synaptic responses showed similar buildup of asynchronous release during AP trains (Fig. 7*C*). To account for asynchronous release during AP trains, we made cumulative area plots from the 25 Hz trains (Moulder and Mennerick, 2005; Stevens and Williams, 2007). They consisted of charge integrals of total synaptic charge transfer, and a line of best fit was calculated by linear regression (Fig. 7*D*). The average RRP charge estimated from the cumulative area at time 0 was 7.9 ± 3.3 pC ($n = 7$) during single firing and markedly increased to 26.4 ± 7.4 pC ($n = 7$), a more than threefold increase during the burst stimulation ($p < 0.05$, Wilcoxon signed-rank test; Fig. 7*E*).

Attenuation of rapid dynamic change of GABA release by 4-aminopyridine (4-AP)

Unlike the release-independent short-term plasticity found at FS IN-to-GC synapses (Kraushaar and Jonas, 2000), rapid dynamic changes of non-FS IN-to-GC synapses are presynaptic activity- and release-dependent. We next asked whether increasing presynaptic spike duration, and therefore driving more Ca^{2+} into terminals, could further increase the probability of release and in turn decrease the extent of the dynamic switch. We inhibited voltage-gated K^+ channels with 30 μM 4-AP. Bath application of 4-AP slightly increased the somatic AP half-duration (control, 1.60 ± 0.07 ms; 4-AP, 1.91 ± 0.14 ms, $n = 6$; $p = 0.06$, Wilcoxon signed-rank test) and preferentially increased the $uIPSC_1$ magnitude during single AP modes (control, 125.0 ± 113.7 pA; 4-AP, 269.0 ± 227.2 pA, $n = 6$; $p < 0.05$, Wilcoxon signed-rank test; Fig. 8*A1*,*A2*). On average, the degree of the dynamic switch of the $uIPSC_1$ magnitude was reduced in the presence of 4-AP (control, 8.58 ± 1.08-fold; 4-AP, 2.87 ± 0.86-fold; $n = 6$; $p < 0.05$, Wilcoxon signed-rank test; Fig. 8*C*). Notably, although the multiple-pulse ratio ($uIPSC_5/uIPSC_1$) decreased (control, 0.58 ± 0.15; 4-AP, 0.19 ± 0.04; 6 pairs, respectively; $p < 0.05$, Wilcoxon signed-rank test; Fig. 8*D*) in the presence of 4-AP, the $uIPSC_1$ magnitude during burst AP modes was unchanged (see Discussion).

We also tested for 4-AP effect on FS IN-to-GC synapses. In contrast to non-FS IN-to-GC synapses, bath application of 4-AP at low concentrations had little effect on the $uIPSC_1$ magnitude during both single and burst AP modes (Fig. 8B_1,B_2). On average, the degrees of the dynamic switch of the $uIPSC_1$ magnitude in control and in the presence of 4-AP were 1.04 ± 0.05-fold and 1.12 ± 0.05-fold (4 pairs, Fig. 8*C*), respectively. Consistently, the multiple-pulse ratio ($uIPSC_5/uIPSC_1$) was unchanged (control, 0.44 ± 0.06; 4-AP, 0.39 ± 0.04; 4 pairs, respectively; Fig. 8*D*). As non-FS IN output synapses are markedly more sensitive to 4-AP at low concentrations than FS IN output synapses, our results suggest differential expression of K^+ channels between FS and non-FS IN terminals.

Rapid dynamic changes of dendritic inhibition is preserved at near-physiological temperature

Cortical inhibitory INs *in vivo* discharge bursts of APs at γ frequency range during the Up state (Massi et al., 2012). Although the natural firing pattern of INs in the DG remains to be determined, we tested whether dendrite-targeting INs fired in *in vivo* recorded discharge patterns exhibited rapid dynamic release during bursting complexes. To mimic the physiological activity, INs were stimulated for 20 s at near-physiological temperature using an IN spike train (Fig. 9A_1,B_1, hash marks) recorded from anesthetized rats as the stimulation protocol. The stimulation protocol comprised variable stimuli at 30–90 Hz frequency (cell code LK10c from Massi et al., 2012). At 35 ± 2°C, rapid dynamic release from dendrite-targeting IN output synapses during mode transitions was preserved. As illustrated in Figure 9A_1, the efficacy of neurotransmission was low during low-frequency AP stimulation but was greatly enhanced during clustered AP stimulation. Figure 9A_2 illustrates that single APs did not reliably generate

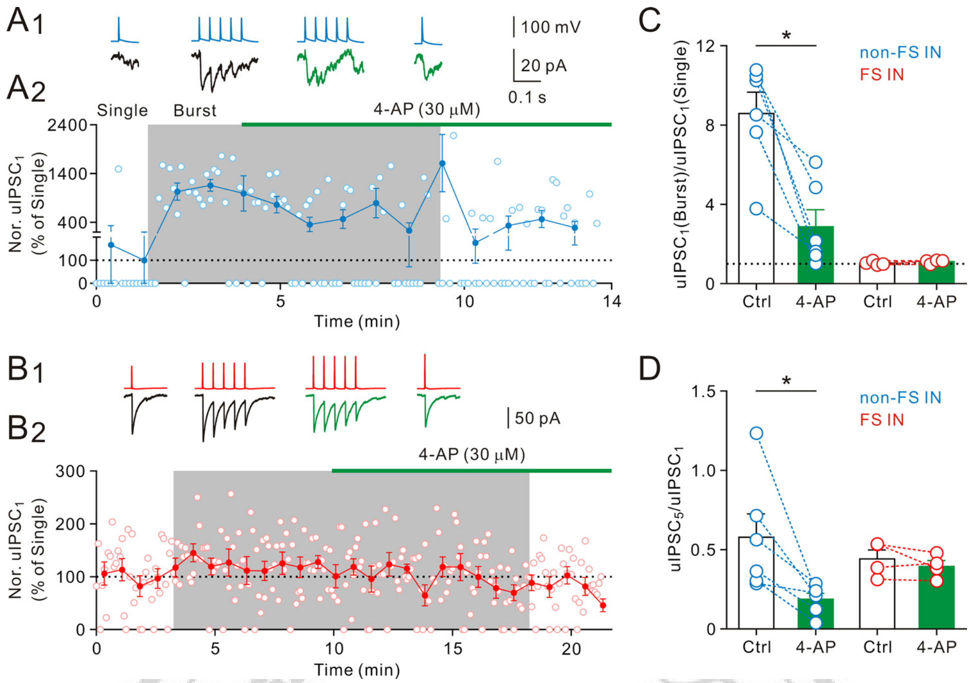

Figure 8. Blockade of K$^+$ channels decreased the extent of the dynamic switch of dendritic inhibition. **A_1**, Bursts of presynaptic APs (“Burst” mode, 25 Hz) and single presynaptic APs (“Single” mode) were repetitively evoked at 0.2 Hz in a non-FS cell; postsynaptic uIPSC traces were average of 15–30 sweeps. **A_2**, Plot of their mean uIPSC$_1$ amplitude (normalized to the “Single” mode in control) in control and in the presence of 4-AP (30 μM). Horizontal bar represents time of 4-AP application. 4-AP greatly increased uIPSCs and decreased the failures during the “single” mode. **B_1**, Bursts of presynaptic APs (“Burst” mode, 25 Hz) and single presynaptic APs (“Single” mode) were repetitively evoked at 0.2 Hz in a FS cell; postsynaptic uIPSC traces were average of 30 sweeps. **B_2**, Plot of their normalized mean uIPSC$_1$ amplitude in control and in the presence of 4-AP (30 μM). Horizontal bar represents time of 4-AP application. ***C***, Ratio of mean uIPSC$_1$ amplitude in the “Burst” mode over mean uIPSC$_1$ amplitude in the “Single” mode in control and in the presence of 4-AP (30 μM). $*p < 0.05$. ***D***, Multiple-pulse ratio in control and in the presence of 4-AP. $*p < 0.05$.

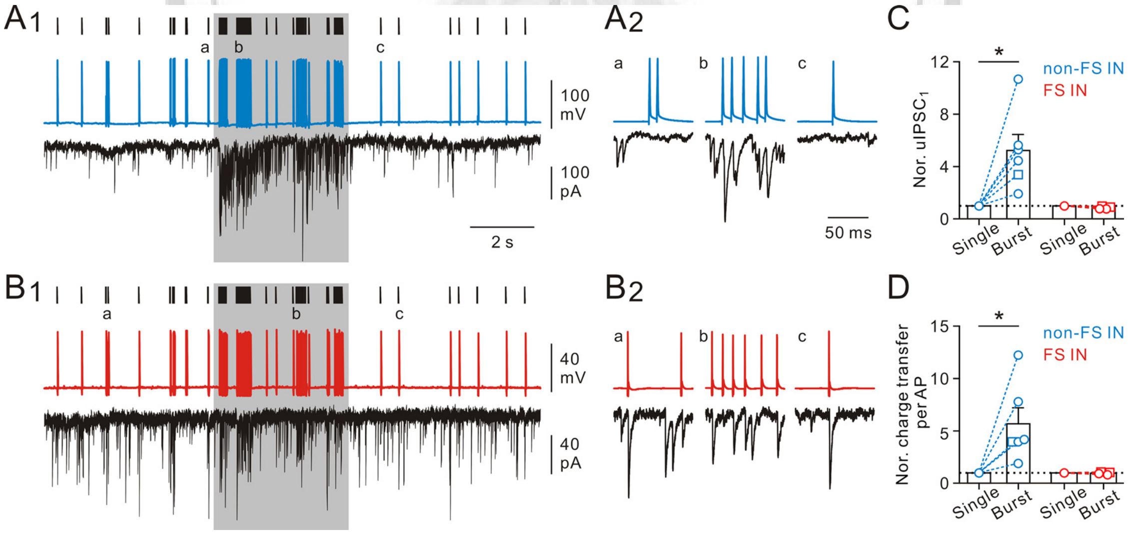

Figure 9. Rapid dynamic changes of dendritic inhibition preserved at near-physiological temperature. **A_1**, Top, Spike train (shown with hash marks; adapted from Massi et al., 2012) as the stimulation protocol. Middle, Evoked spikes in a dendrite-targeting IN. Bottom, uIPSCs recorded from a postsynaptic GC (single sweep). **A_2**, Enlargement of spikes and uIPSCs as indicated in **A_1**. **B_1**, Top, Same stimulation protocol as in **A_1**. Middle, Discharge pattern of a soma-targeting IN. Bottom, uIPSCs recorded from a postsynaptic GC (single sweep). **B_2**, Enlargement of spikes and uIPSCs as indicated in **B_1**. ***C***, Summary of mean uIPSC$_1$ (normalized to the “Single” mode) from the “Single” and “Burst” modes. $*p < 0.05$. ***D***, Summary of normalized mean charge transfer per AP from the “Single” and “Burst” modes. Circle represents 35°C ($n = 7$); square represents 23°C ($n = 3$). $*p < 0.05$.

postsynaptic responses in contrast to AP bursts. On average, the uIPSC$_1$ magnitude and charge transfer per AP increased to 523 ± 122% ($n = 6$ pairs; $p < 0.05$, Wilcoxon signed-rank test; Fig. 9*C*) and 568 ± 153% ($n = 6$ pairs; $p < 0.05$, Wilcoxon signed-rank test; Fig. 9*D*), respectively. In contrast, soma-targeting INs maintained stable and reliable release during single to burst AP transitions (Fig. 9B_1,B_2). On average, the uIPSC$_1$ and charge transfer per AP were unchanged (uIPSC$_1$, 86 ± 4%; charge transfer per AP, 96 ± 5%; $n = 4$ pairs; Fig. 9*C*,*D*). Under the same conditions tested, the substantial difference between dendrite- and soma-targeting IN output synapses was preserved at 35 ± 2°C (Fig. 9*C*,*D*). Thus, rapid dynamic changes of GABA release from

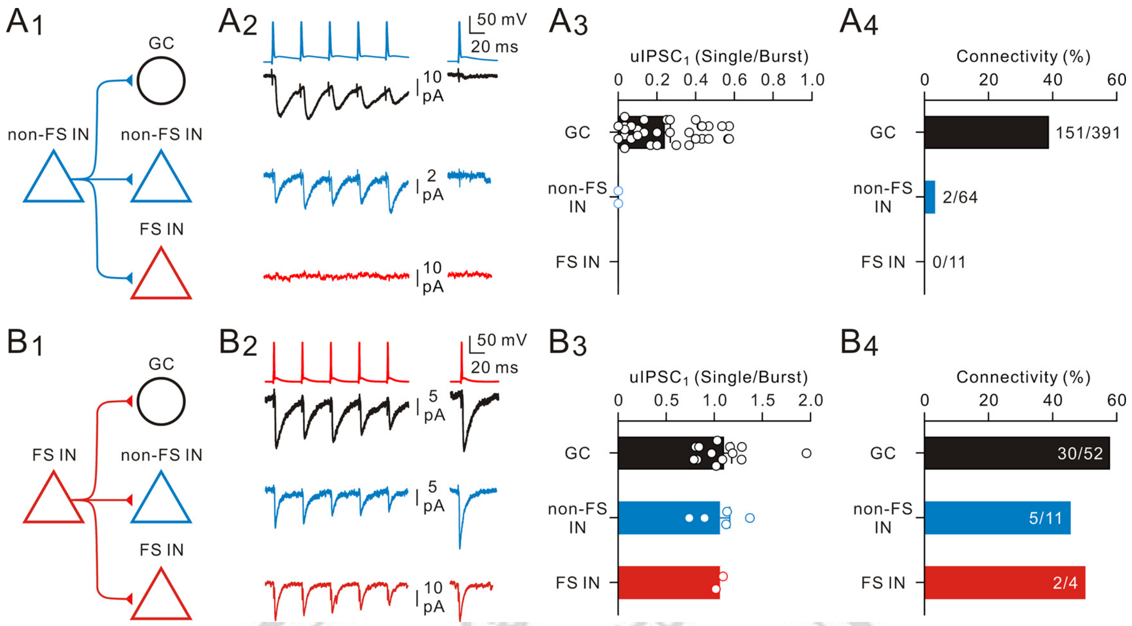

Figure 10. Connectivity and specificity of the synaptic dynamic switch. **A_1**, Schematic of non-FS IN (blue triangle) to GC (black circle), non-FS IN (blue triangle), and FS IN (red triangle) connections. **A_2**, Representative AP trace (top) from a non-FS IN and average uIPSC traces (bottom) recorded from a GC, a non-FS IN, and a FS IN. No functional connection was detected at non-FS IN-to-FS IN synapses. **A_3**, Summary of the fraction of uIPSC_1 (Single)/uIPSC_1 (Burst) from non-FS IN-to-GC, non-FS IN-to-non-FS IN, and non-FS IN-to-FS IN connections, respectively. **A_4**, Summary plot of the frequency of possible non-FS IN-to-GC, non-FS IN-to-non-FS IN, and non-FS IN-to-FS IN connections. There were 151 of 391 possible non-FS IN-to-GC, 2 of 64 possible non-FS IN-to-non-FS IN, and 0 of 11 possible non-FS IN-to-FS IN connections. **B_1**, Schematic of FS IN to GC, non-FS IN, and FS IN connections. **B_2**, AP trace (top) from a FS IN and average uIPSC traces (bottom) recorded from a GC, a non-FS IN, and a FS IN. Current traces are average of 20–80 sweeps. **B_3**, Summary of the fraction of uIPSC_1 (Single)/uIPSC_1 (Burst) from FS IN-to-GC, FS IN-to-non-FS IN, and FS IN-to-FS IN connections, respectively. **B_4**, Summary plot of the frequency of possible connections. There were 30 of 52 possible FS IN-to-GC, 5 of 11 possible FS IN-to-non-FS IN, and 2 of 4 possible FS IN-to-FS IN connections.

dendrite-targeting IN terminals occur at physiological temperature and with behaviorally relevant stimulation patterns. As dendrite-targeting INs provide a rapid fluctuating output, they could efficiently change the gain of input–output relations of GCs *in vivo* (Hefft and Jonas, 2005).

Functional connectivity and specificity of the synaptic dynamic switch

To further determine whether the rapid dynamic switch of GABA release is dependent on postsynaptic cell type, we recorded from non-FS IN-to-non-FS IN, non-FS IN-to-FS IN, FS IN-to-FS IN, and FS IN-to-non-FS IN pairs (Fig. 10A_1,B_1). Regardless of the cell type of postsynaptic targets, the rapid dynamic switch of GABA release was exclusively detected at pairs with non-FS cells as presynaptic neurons, suggesting presynaptic cell type specificity (Fig. 10A_2,B_2). The uIPSC_1 (single/burst) ratios at non-FS IN-to-GC and non-FS IN-to-non-FS IN synapses were 0.24 ± 0.03 ($n = 36$) and 0 ($n = 2$), respectively (Fig. 10A_3). By contrast, the uIPSC_1 (single/burst) ratios at FS IN output synapses (FS IN-to-GC, 1.10 ± 0.09, $n = 13$; FS IN-to-non-FS IN, 1.05 ± 0.11, $n = 5$; FS IN-to-FS IN, 1.05, $n = 2$) were close to 1 (Fig. 10B_3). Further analyses of synaptic dynamics revealed that FS IN output synapses exhibited short-term depression when tested at 25 Hz ($\text{uIPSC}_5/\text{uIPSC}_1$: 0.51 ± 0.04 at FS IN-to-GC pairs, $n = 12$; 0.54 ± 0.10 at FS IN-to-non FS IN pairs, $n = 5$; 0.50 at FS IN-to-FS IN pairs, $n = 2$). In contrast, non-FS IN output synapses appeared to display a functional divergence: the non-FS IN-to-GC synapses showed short-term depression ($\text{uIPSC}_5/\text{uIPSC}_1$: 0.63 ± 0.06, $n = 29$), whereas non-FS IN-to-non FS IN synapses exhibited little short-term plasticity ($\text{uIPSC}_5/\text{uIPSC}_1$: 1.10, $n = 2$) under the same stimulation condition. Notably, no functional connectivity was detected at non-FS IN-to-FS IN pairs in the present study (11 pairs; Fig. 10A_4).

Our study also revealed cell-type specificity of the functional connectivity (Fig. 10A_4,B_4). Non-FS INs preferentially formed functional connections with GCs (38.6%; 151 of 391 pairs) but rarely formed connections with non-FS INs (3.1%; 2 of 64 pairs) and FS INs (0%; 0 of 11 pairs). In contrast, FS INs frequently and almost equally formed connections with GCs (57.7%; 30 of 52 pairs), non-FS INs (45.4%; 5 of 11 pairs), and FS INs (50%; 2 of 4 pairs).

Discussion

Here, we report a novel synaptic dichotomy between two IN classes (soma targeting vs dendrite targeting) in the DG. Notably, despite considerable heterogeneity in dendrite-targeting IN properties and projection patterns, they all exhibit a rapid switch in GABA release between periods of sparse spiking activity and periods of enhanced activity at both 23°C and 35°C in contrast to soma-targeting INs (Table 1).

IN dichotomy in distinct microcircuits

Similar to our present study, a number of functional and anatomical dichotomies have been shown to exist between two IN classes, PV^+BCs and CCK^+BCs, in the hippocampus proper (see review by Armstrong and Soltesz, 2012). However, these two circuits, CA areas and DG, differ in some respects. First, INs in the DG exert shunting inhibition and depolarize GCs at rest, whereas INs in the CA1 and CA3 areas generate hyperpolarizing inhibition onto pyramidal cells (Glickfeld et al., 2009; Chiang et al., 2012). Second, unlike the remarkable axonal distribution of CB_1R^+ INs within the IML, CCK^+ (also termed CB_1R-containing) BCs in the CA1 area primarily synapse onto the somata of their principal cell targets with a slight shifted distribution toward the proximal dendrites (Glickfeld and Scanziani, 2006). Third, PV$^+$BC input, but not CCK$^+$BC input, in the CA1 area is selectively modulated by the hyperpolarization-activated chloride channel, ClC-2 (Földy et al., 2010). Such synapse-specific expression of ClC-2 is not present in the DG. Overall, these differences point to circuit-specific network function of INs.

Classification of dendrite-targeting INs

Compared with soma-targeting INs, dendrite-targeting INs are more complex and heterogeneous. In this study, we focus exclusively on dendrite-targeting INs with their somata at the border between the GCL and the hilus. According to previous studies (Han et al., 1993; Freund and Buzsáki, 1996), there are three major subtypes (i.e., CB$_1$$^+$INs, HICAP and HIPP cells). However, we observed a small population of INs not compatible with these classifications. In this study, INs with their axon projection to the OML were classified as HIPP cells. Among them, the majority (9 of 13 cells) of HIPP cells did display their dendrites strictly in the hilus, in agreement with that of Han et al. (1993). In other words, we observed four atypical HIPP-like cells, which project their axons to the OML, but have the dendritic arbor in the ML. Furthermore, we found that 7 of 13 of HIPP cells exhibit axon collaterals in the IML in addition to the OML. The possible explanation is that our slices were cut from the hippocampus at some septotemporal level where the IML may be very narrow or the angle of sectioning relative to layer boundaries may influence the appearance of the axon. It is also likely that those atypical HIPP cells represent a novel subtype of INs. The features of Petilla nomenclature (Ascoli et al., 2008) may provide a stepping stone toward a future classification of these atypical INs.

Synapse selectivity in the DG

The connectivity of non-FS IN onto different types of target cells in the DG suggests target-cell selectivity. The probability of finding a synaptic connection between non-FS INs and GCs is considerably higher than those in non-FS IN-to-non-FS IN and non-FS IN-to-FS IN pairs (Fig. 10*A*$_4$). In contrast, the connectivity of FS IN onto target cells is relatively independent of target cell type (Fig. 10*B*$_4$). Interestingly, nonrandom local circuits have been reported previously in the DG (Larimer and Strowbridge, 2008). Mossy cells in the hilus show profound synapse selectivity: 87.5% of their intralamellar excitatory connections are exclusively onto hilar INs (mossy cell-to-IN connectivity is 6%; 7 of 114 cells) and 12.5% of their intralamerllar excitatory connections (mossy cell-to-mossy cell connectivity is 0.5%; 1 of 206 cells) are onto mossy cell. Similarly, hilar INs also show high synapse selectivity and primarily synapse onto mossy cells (81% of inhibitory connections; hilar IN-to-mossy cell connectivity is 15%) with relatively few connections (19% of inhibitory connections; hilar IN-to-hilar IN connectivity is 6%) onto other hilar INs.

Possible mechanisms by which presynaptic activity regulates the short-term presynaptic facilitation

Cortical INs display a specific mode of firing composed of sparse and clustered APs (Goldberg et al., 2008). In our experimental conditions, whereas firing of dendrite-targeting INs is switched from the single to the burst spiking mode, the probability of release is rapidly enhanced, suggesting that AP bursts induced a long-lasting increase in [Ca^{2+}]$_i$ in the terminals and the residual [Ca^{2+}]$_i$ enables the enhancement of subsequent GABA release. Accumulation of residual [Ca^{2+}]$_i$ may be attributed to the loose coupling between Ca^{2+} sources and release sensors (Eggermann et al., 2012) and/or saturation of endogenous Ca^{2+} buffers (Fioravante and Regehr, 2011). This hypothesis can be tested by introducing the slowly acting, but high-affinity, Ca^{2+} buffer EGTA into presynaptic terminals (Eggermann et al., 2012). Indeed, the effect of EGTA-AM strongly depress GABA release in dendrite-targeting INs. This is in great contrast to the lack of effect of the EGTA-AM on soma-targeting IN output synapses, where Ca^{2+} channels and Ca^{2+} sensors are tightly coupled (Hefft and Jonas, 2005; Bucurenciu et al., 2008). Here, a potential caveat should be noted. We cannot exclude a contribution of other variables that can affect neurotransmission by EGTA-AM; for instance, the treatment could affect the release of another substance that is selectively modulating synaptic transmission at non-FS IN output synapses but not FS IN output synapses.

Changes of AP shape can regulate release probability. By prolonging AP duration in the terminals, the probability of release may increase via the enhancement of presynaptic Ca^{2+} influx. In agreement with this view, inhibition of voltage-gated K$^+$ channels with 4-AP increases AP duration and greatly enhances single AP-evoked uIPSCs. A significant decrease in multiple-pulse ratio (Fig. 8*D*) confirmed that 4-AP enhances presynaptic release, thus reducing the extent of dynamic change during mode transitions. A lack of 4-AP effect on the enhancement of uIPSC$_1$ amplitude during the burst mode suggests that other activity-dependent gating mechanisms may be involved in regulating neurotransmission (Brody and Yue, 2000; Kraushaar and Jonas, 2000).

As indicated by an increase in multiple-pulse ratio (Figs. 5 and 6), the reduction of burst-induced IPSC amplitude by the prolonged interburst interval or EGTA-AM appears to be a result of a decrease in the probability of the release. However, a recent study (Thanawala and Regehr, 2013) shows that alterations in presynaptic calcium influx can also change the effective RRP size. Indeed, we found that the RRP is markedly increased during periods of burst firing. Thus, the calcium dependence of rapid enhancement of GABA release is likely determined by the combined calcium dependencies of the release probability and the effective size of the RRP. Finally, in addition to those discussed above, we still cannot exclude other mechanisms here, such as use-dependent increases in presynaptic Ca^{2+} currents (Ishikawa et al., 2005) or activation of presynaptic receptors (Ruiz et al., 2010).

Significance of dynamic switches of dendritic inhibition in network function

Sparse dentate activity is thought to be important for pattern separation and spatial information encoding (Leutgeb et al., 2007; McHugh et al., 2007; Moser et al., 2008). Multiple cellular mechanisms are coordinated for sparse activation of GCs. First, GC dendrites act as strong voltage attenuators. Synaptic inputs from the cortex strongly attenuate along GC dendrites (Schmidt-Hieber et al., 2007; Krueppel et al., 2011). Second, GC dendritic properties are linear integrators. GC dendrites summate synaptic inputs linearly and are not designed for highly efficient synchrony detection (Krueppel et al., 2011). Third, GC dendrites lack dendritic spikes that would allow them to be more efficiently to bring EPSPs to AP threshold (Krueppel et al., 2011). Finally, GCs have relatively hyperpolarized resting membrane potentials compared with other types of neurons (Schmidt-Hieber et al., 2007; Chiang et al., 2012). Beyond the cellular level, what is the circuit mechanism that contributes to the quiescent nature of GCs? Here, we show that GCs are controlled by the powerful dendritic inhibition during periods of intense activity. This novel finding not only provides an important bridge between the fields of synaptic short-term plasticity and hippocampal network states but also lends a considerable support for a critical role of dendritic inhibitory circuits in gating the information transfer from the cortex to the hippocampus.

GABAergic INs exert shunting inhibition onto GCs in the adult brain (Chiang et al., 2012). Therefore, burst spiking of dendrite-targeting INs during Up states may promote dendritic excitability but also exert powerful shunting inhibition to limit the degree of dendritic depolarization. Such a rapid switch on/off of dendritic inhibition during state transitions can prevent overexcitation of GCs and effectively control the total amount of signal transfer from the cortex to the hippocampus under normal conditions. Dendrite-targeting IN-GC synapses have a long synaptic latency. What is the computational significance of such a long delay? Analysis of IN network models suggests that the network oscillation frequency is reduced by longer delays and increased by shorter delays (see review by Bartos et al., 2007). Moreover, network coherence is substantially increased by shorter delays and reduced by longer delays. Together, specialization of dendrite-targeting IN connections may expand the dynamic range of network oscillation frequency and coherence.

References

Armstrong C, Soltesz I (2012) Basket cell dichotomy in microcircuit function. J Physiol 590:683–694. CrossRef Medline

Ascoli GA, Alonso-Nanclares L, Anderson SA, Barrionuevo G, Benavides-Piccione R, Burkhalter A, Buzsáki G, Cauli B, Defelipe J, Fairén A, Feldmeyer D, Fishell G, Fregnac Y, Freund TF, Gardner D, Gardner EP, Goldberg JH, Helmstaedter M, Hestrin S, Karube F, et al. (2008) Petilla terminology: nomenclature of features of GABAergic interneurons of the cerebral cortex. Nat Rev Neurosci 9:557–568. CrossRef Medline

Bartos M, Vida I, Jonas P (2007) Synaptic mechanisms of synchronized gamma oscillations in inhibitory interneuron networks. Nat Rev Neurosci 8:45–56. CrossRef Medline

Bartos M, Alle H, Vida I (2011) Role of microcircuit structure and input integration in hippocampal interneuron recruitment and plasticity. Neuropharmacology 60:730–739. CrossRef Medline

Bragin A, Jandó G, Nádasdy Z, Hetke J, Wise K, Buzsáki G (1995) Gamma (40–100 Hz) oscillation in the hippocampus of the behaving rat. J Neurosci 15:47–60. Medline

Brody DL, Yue DT (2000) Release-independent short-term synaptic depression in cultured hippocampal neurons. J Neurosci 20:2480–2494. Medline

Bucurenciu I, Kulik A, Schwaller B, Frotscher M, Jonas P (2008) Nanodomain coupling between Ca^{2+} channels and Ca^{2+} sensors promotes fast and efficient transmitter release at a cortical GABAergic synapse. Neuron 57:536–545. CrossRef Medline

Buzsáki G (1984) Feed-forward inhibition in the hippocampal formation. Prog Neurobiol 22:131–153. CrossRef Medline

Chiang PH, Wu PY, Kuo TW, Liu YC, Chan CF, Chien TC, Cheng JK, Huang YY, Chiu CD, Lien CC (2012) GABA is depolarizing in hippocampal dentate granule cells of the adolescent and adult rats. J Neurosci 32:62–67. CrossRef Medline

Chiu CQ, Lur G, Morse TM, Carnevale NT, Ellis-Davies GC, Higley MJ (2013) Compartmentalization of GABAergic inhibition by dendritic spines. Science 340:759–762. CrossRef Medline

Cobb SR, Buhl EH, Halasy K, Paulsen O, Somogyi P (1995) Synchronization of neuronal activity in hippocampus by individual GABAergic interneurons. Nature 378:75–78. CrossRef Medline

Eggermann E, Bucurenciu I, Goswami SP, Jonas P (2012) Nanodomain coupling between Ca^{2+} channels and sensors of exocytosis at fast mammalian synapses. Nat Rev Neurosci 13:7–21. CrossRef Medline

Fioravante D, Regehr WG (2011) Short-term forms of presynaptic plasticity. Curr Opin Neurobiol 21:269–274. CrossRef Medline

Földy C, Lee SH, Morgan RJ, Soltesz I (2010) Regulation of fast-spiking basket cell synapses by the chloride channel ClC-2. Nat Neurosci 13:1047–1049. CrossRef Medline

Förster E, Zhao S, Frotscher M (2006) Laminating the hippocampus. Nat Rev Neurosci 7:259–267. CrossRef Medline

Freund TF, Buzsáki G (1996) Interneurons of the hippocampus. Hippocampus 6:347–470. Medline

Glickfeld LL, Scanziani M (2006) Distinct timing in the activity of cannabinoid-sensitive and cannabinoid-insensitive basket cells. Nat Neurosci 9:807–815. CrossRef Medline

Glickfeld LL, Roberts JD, Somogyi P, Scanziani M (2009) Interneurons hyperpolarize pyramidal cells along their entire somatodendritic axis. Nat Neurosci 12:21–23. CrossRef Medline

Goldberg EM, Clark BD, Zagha E, Nahmani M, Erisir A, Rudy B (2008) K^+ channels at the axon initial segment dampen near-threshold excitability of neocortical fast-spiking GABAergic interneurons. Neuron 58:387–400. CrossRef Medline

Haider B, McCormick DA (2009) Rapid neocortical dynamics: cellular and network mechanism. Neuron 62:171–189. CrossRef Medline

Haider B, Duque A, Hasenstaub AR, McCormick DA (2006) Neocortical network activity in vivo is generated through a dynamic balance of excitation and inhibition. J Neurosci 26:4535–4545. CrossRef Medline

Han ZS, Buhl EH, Lörinczi Z, Somogyi P (1993) A high degree of spatial selectivity in the axonal and dendritic domains of physiologically identified local-circuit neurons in the dentate gyrus of the rat hippocampus. Eur J Neurosci 5:395–410. CrossRef Medline

Hefft S, Jonas P (2005) Asynchronous GABA releases generates long-lasting inhibition at a hippocampal interneuron-principal neuron synapse. Nat Neurosci 8:1319–1328. CrossRef Medline

Howard A, Tamas G, Soltesz I (2005) Lighting the chandelier: new vistas for axo-axonic cells. Trends Neurosci 28:310–316. CrossRef Medline

Hu H, Martina M, Jonas P (2010) Dendritic mechanisms underlying rapid synaptic activation of fast-spiking hippocampal interneurons. Science 327:52–58. CrossRef Medline

Ishikawa T, Kaneko M, Shin HS, Takahashi T (2005) Presynaptic N-type and P/Q-type Ca^{2+} channels mediating synaptic transmission at the calyx of Held of mice. J Physiol 568:199–209. CrossRef Medline

Jonas P, Vyleta NO (2012) Loose coupling between Ca^{2+} channels and release sensors generated "conditional detonator" properties of hippocampal mossy fiber terminals (Program 334.19). 2012 Neuroscience Meeting Planner. Washington, DC: Society for Neuroscience.

Klausberger T, Somogyi P (2008) Neuronal diversity and temporal dynamics: the unity of hippocampal circuit operations. Science 321:53–57. CrossRef Medline

Kraushaar U, Jonas P (2000) Efficacy and stability of quantal GABA release at a hippocampal interneuron-principal neuron synapse. J Neurosci 20:5594–5607. Medline

Krueppel R, Remy S, Beck H (2011) Dendritic integration in hippocampal dentate granule cells. Neuron 71:512–528. CrossRef Medline

Larimer P, Strowbridge BW (2008) Nonrandom local circuits in the dentate gyrus. J Neurosci 28:12212–12223. CrossRef Medline

Leão RN, Mikulovic S, Leão KE, Munguba H, Gezelius H, Enjin A, Patra K, Eriksson A, Loew LM, Tort AB, Kullander K (2012) OLM interneurons differentially modulate CA3 and entorhinal inputs to hippocampal CA1 neurons. Nat Neurosci 15:1524–1530. CrossRef Medline

Leutgeb JK, Leutgeb S, Moser MB, Moser EI (2007) Pattern separation in the dentate gyrus and CA3 of the hippocampus. Science 315:961–966. CrossRef Medline

Lien CC, Jonas P (2003) Kv3 potassium conductance is necessary and kinetically optimized for high-frequency action potential generation in hippocampal interneurons. J Neurosci 23:2058–2068. Medline

Lien CC, Mu Y, Vargas-Caballero M, Poo MM (2006) Visual stimuli-induced LTD of GABAergic synapses mediated by presynaptic NMDA receptors. Nat Neurosci 9:372–380. CrossRef Medline

Mann EO, Suckling JM, Hajos N, Greenfield SA, Paulsen O (2005) Perisomatic feedback inhibition underlies cholinergically induced fast network oscillations in the rat hippocampus in vitro. Neuron 45:105–117. CrossRef Medline

Massi L, Lagler M, Hartwich K, Borhegyi Z, Somogyi P, Klausberger T (2012) Temporal dynamics of parvalbumin-expressing axo-axonic and basket cells in the rat medial prefrontal cortex in vivo. J Neurosci 32:16496–16502. CrossRef Medline

McBain CJ, Fisahn A (2001) Interneurons unbound. Nat Rev Neurosci 2:11–23. CrossRef Medline

McHugh TJ, Jones MW, Quinn JJ, Balthasar N, Coppari R, Elmquist JK, Lowell BB, Fanselow MS, Wilson MA, Tonegawa S (2007) Dentate gyrus NMDA receptors mediate rapid pattern separation in the hippocampal network. Science 317:94–99. CrossRef Medline

Miles R, Tóth K, Gulyás AI, Hájos N, Freund TF (1996) Differences between somatic and dendritic inhibition in the hippocampus. Neuron 16:815–823. CrossRef Medline

Moser EI, Kropff E, Moser MB (2008) Place cells, grid cells, and the brain's spatial representation system. Annu Rev Neurosci 31:69–89. CrossRef Medline

Moulder KL, Mennerick S (2005) Reluctant vesicles contribute to the total readily releasable pool in glutamatergic hippocampal neurons. J Neurosci 25:3842–3850. CrossRef Medline

Myatt DR, Hadlington T, Ascoli GA, Nasuto SJ (2012) Neuromantic- from semi-manual to semi-automatic reconstruction of neuron morphology. Front Neuroinform 6:4. CrossRef Medline

Pouille F, Scanziani M (2001) Enforcement of temporal fidelity in pyramidal cells by somatic feed-forward inhibition. Science 293:1159–1163. CrossRef Medline

Pouille F, Scanziani M (2004) Routing of spike series by dynamic circuits in the hippocampus. Nature 429:717–723. CrossRef Medline

Rizzoli SO, Betz WJ (2005) Synaptic vesicle pools. Nat Rev Neurosci 6:57–69. CrossRef Medline

Ruiz A, Campanac E, Scott RS, Rusakov DA, Kullmann DM (2010) Presynaptic $GABA_A$ receptors enhance transmission and LTP induction at hippocampal mossy fiber synapses. Nat Neurosci 13:431–438. CrossRef Medline

Schmidt-Hieber C, Jonas P, Bischofberger J (2007) Subthreshold dendritic signal processing and coincidence detection in dentate gyrus granule cells. J Neurosci 27:8430–8441. CrossRef Medline

Stevens CF, Williams JH (2007) Discharge of the readily releasable pool with action potentials at hippocampal synapses. J Neurophysiol 98:3221–3229. CrossRef Medline

Thanawala MS, Regehr WG (2013) Presynaptic calcium influx controls neurotransmitter release in part by regulating the effective size of the readily releasable pool. J Neurosci 33:4625–4633. CrossRef Medline

Zucker RS, Regehr WG (2002) Short-term synaptic plasticity. Annu Rev Physiol 64:355–405. CrossRef Medline